AN ANALYTICAL STUDY OF CONFINED VORTEX FLOW

Ngo Dinh Thinh

A THESIS

in the

Faculty of Engineering

Presented in Partial Fulfillment of the Requirements for
the Degree of Doctor of Engineering at
Concordia University
Montreal, Canada

March 1975

Ngo Dinh Thinh

AN ANALYTICAL STUDY OF CONFINED VORTEX FLOW

ABSTRACT

The swirling, incompressible flow within a short vortex chamber has been studied analytically. A set of non-dimensional differential equations are developed for the whole vortex flow field which is divided into two regions, namely an annular and an inner region. Wormley's analytical technique is further extended to include an apparent viscosity for the annular region. The technique of separation of variables is applied to formulate the equations of motion in the inner region. Differential equations are solved numerically using the Runge-Kutta method. All the fluid parameters including the apparent viscosity match at the boundary between the annular region and the inner flow region of the vortex chamber.

The analytical results show the variation of the apparent viscosity across the whole vortex chamber and show that the values of apparent viscosity seriously affect the velocity profile within the vortex chamber. In comparison with the existing experimental data, the magnitude of the apparent viscosity is obtained and further substantiates the earlier prediction by Kwok.

Flow characteristics and velocity profiles for the whole chamber were analytically obtained for two-cell as well as for multi-cell vortex flows.

ACKNOWLEDGEMENT

The author wishes to express his appreciation to his research directors, Professor Clyde C.K. Kwok and Professor Sui Lin, for their encouragement and guidance throughout all stages of this investigation.

The author also wishes to express his gratitude to Professor Morne P. duPlessis, Chairman of the Mechanical Engineering Department and Professor Clyde C.K. Kwok for arranging financial support during his full time period of this investigation.

Special thanks are extended to his employer, United Aircraft of Canada Limited, for the company's Educational Assistance Programme.

The author is deeply grateful to his parents and his wife, Thanh Van, for their patience and encouragement which made his entire graduate study possible.

Thanks are due to Nancy Elliott for typing the manuscript.

This work was partially supported by the National Research Council of Canada under Grant No. A 7435.

TABLE OF CONTENTS

LIST OF FIGURES

NOMENCLATURE

A, A_1, A_2	function $\phi(Z)$ and its derivatives, ϕ, $\frac{d\phi}{dZ}$, $\frac{d^2\phi}{dZ^2}$
B, B_1, B_2	function $\psi(Z)$ and its derivatives, ψ, $\frac{d\psi}{dZ}$, $\frac{d^2\psi}{dZ^2}$
C	constant
C_1, C_2, C_3	chamber geometry factor
C_f	friction factor
$\frac{dX_1}{dR}, \ldots, \frac{dX_8}{dR}$	ordinary differential equations representing flow parameters
f	end wall friction coefficient
$f(n)$	velocity profile function
$F(R)$	axial velocity function
$g(n)$	velocity profile function
$G(R)$	radial velocity function
h	chamber height, m.
H	non-dimensional chamber height = $\frac{h}{r_e}$
K_1	constant
K_2	constant
m, n	power index
p	pressure, Pa
p_a	ambient pressure, Pa
p_o	pressure at radius r_o, Pa
P	a non-dimensional pressure = $(p-p_a)/\rho v_o^2$
Qc, Qs	control and supply flow rate, m^3/s
$+r$	direction from center to periphery

$-r$	direction from periphery to center
r_e	exit radius, m.
r_o	chamber radius, m.
r, ϕ, z	cylindrical coordinates
R	non-dimensional radius $= \frac{r}{r_e}$
R_e	non-dimensional orifice radius $= \frac{r_e}{r_e} = 1$
R_o	non-dimensional chamber radius $= \frac{r_o}{r_e}$
R^*	non-dimensional radius in the annular region where U becomes zero
RE	Reynolds number $= \frac{\rho v_o r_e}{\mu}$
u, v, w	components of velocity in Cartesian coordinates, m/s.
u', v', w'	velocity fluctuations in Cartesian coordinates, m/s.
u_o	radial velocity in the core region at r_o defined positive in $-r$ direction, m/s.
u_s	radial velocity coefficient in the boundary layer region defined positive in $+r$ direction, m/s.
u_δ	radial velocity coefficient in the inviscid region defined positive in $+r$ direction, m/s.
U, V, W	non-dimensional velocity components in cylindrical coordinates
U_o	non-dimensional velocity at chamber periphery
U_δ	non-dimensional radial velocity coef. in the inviscid region defined positive in $-r$ direction $= -u_\delta/u_o$
U_s	non-dimensional radial velocity coefficient in the boundary layer region defined positive in $-r$ direction $= -u_s/u_o$

v_o	tangential velocity at r_o, m/s.
v_δ	tangential velocity in the inviscid region, m/s.
V_r	radial velocity defined positive in +r direction, m/s.
V_z	axial velocity, m/s.
V_ϕ	tangential velocity, m/s.
x, y, z	Cartesian coordinates
X	dimensionless radial coordinate in -r direction $= 1 - r/r_o$
Z	dimensionless axial coordinate $= z/r_e$
α	power index
α^*	dimensionless parameter $= Q/2\pi\nu_a h$
$\alpha_{1...5}$	velocity profile coefficients
β	constant
Γ	non-dimensional circulation $= v_\delta r/v_o r_o$
δ	boundary layer thickness, m.
$\bar{\delta}$	non-dimensionless boundary layer thickness $= 2\delta/h = \frac{2\delta/r_e}{H}$
δ_e	non-dimensionless boundary layer thickness at interface $= \frac{\delta(r_e)}{r_e}$
ε	eddy viscosity, $N.s/m^2$
η	ratio of axial displacement to boundary layer thickness $= z/\delta$
λ	ratio of outer periphery tangential to radial velocity $= v_o/u_o$

μ	operating fluid viscosity, $N.s/m^2$
μ_a	apparent viscosity, $N.s/m^2$
μ_A	non-dimensional apparent viscosity = $\frac{\mu_a}{\mu}$
ν	operating kinematic viscosity, m^2/s
ν_a	apparent kinematic viscosity, m^2/s
$\phi(Z)$	radial velocity function
$\psi(Z)$	tangential velocity function
ρ	operating fluid density, kg/m^3
σ	normal stress, Pa
τ	shear stress, Pa

CHAPTER 1

INTRODUCTION

1.1 General

In recent years, there has been much interest in the study of incompressible vortex flow because numerous applications utilizing this phenomenon have been evolved in such specialized fields as heat transfer, gas turbine, swirl atomizers, nuclear reactors and meteorology. With the emergence of fluid controls technology especially in the field of "Fluidics", many ingenious ideas and fascinating concepts have stimulated further interest in the many possible applications of confined vortex motion. Fluidic vortex devices which offer the most potential applications are the vortex rate sensor (Fig. 1) and the vortex amplifier (Figs. 2 and 3).

A vortex rate sensor consists of a thin cylindrical chamber with a porous peripheral wall and a plenum chamber external to the porous wall. A central orifice serves as a sink. In the absence of any rotation, the flow in the chamber is radial from the porous wall towards the central orifice. When the sensor is subjected to rotation, fluid coming into the vortex chamber through the porous wall acquires the same tangential velocity as that of the periphery. Due to the presence of the sink hole and the effect of conservation of angular momentum of fluid flow, substantial amplification of the tangential velocity is obtained as the flow

spirals in towards the center. The general flow pattern resembles that of the free vortex. However, due to the presence of inherent viscosity in real fluid flow, the resulting flow is rather complex in nature, consisting of both a free and a forced vortex in structure.

The performance of a vortex rate sensor depends on the sensitivity of the pick-off device. In this particular case, the maximum fluid tangential velocity at the sink must be sensed in some way and the output is in turn used to drive compatible fluid amplifiers. Therefore, if the maximum tangential velocity in the vortex chamber of known geometric configurations can be mathematically predicted, the performance characteristic together with various design parameters of the rate sensor can be established.

The vortex amplifier consists of a thin cylindrical chamber with a wide slot cut radially into the periphery of the chamber for main supply flow and a relatively smaller slot cut tangentially to the periphery for control flow. When there is no control flow, the fluid from the supply flow inlet leaves the chamber through a central outlet orifice with low resistance. When control flow is introduced, the interaction of the power and control jet stream results in significant changes. The tangential control flow enters the chamber and deflects the power stream away from its

radial path to establish a spiral pattern. The deflection of power stream and the subsequent formation of vortex produce two important properties of the flow field. First, as the inlet tangential velocity from the slot increases, the flow path of the main stream lengthens. More resistance is therefore encountered by the flow as it spirals in. Second, due to the conservation of angular momentum, the fluid accelerates as the curvature of the flow path increases. The increase in tangential velocity leads to a centrifugal pressure buildup across the vortex chamber in a radial direction; in other words, the increase in pressure drop across the vortex chamber will result in a reduction of the main supply flow. This constitutes the basis of a vortex amplifier operation.

The fundamental fluid flow equations describing the flow phenomena in the vortex chamber are so complex that most of the engineers engaged in the design and development of vortex fluid amplifiers have resorted to the experimental approach. Better understanding of the vortex flow phenomena is necessary in order to develop a suitable mathematical model for design purposes.

A vast amount of information on swirling flow phenomena has been accumulated over the years. Many reviews and reports exist dealing with various aspects of this problem, among them the work of Gartshore [1, 2], Donaldson and Sullivan [3], and Küchemann [4]. Lewellen [5] has made an extensive review of the state of knowledge

of confined vortex flow and their applications including a bibliography of over 400 references. In his extensive work, he reviewed various possible exact and approximate solutions of the axisymmetric Navier-Stokes equations related to confined vortex flows. The derivations were discussed and critically compared with available experimental data. In this report, a brief review of the methods and solutions in the literature that are most relevant to the present investigation of steady, incompressible, swirling flow will be presented.

In general, theoretical analysis of vortex flow involves solving the Navier-Stokes equations to obtain either approximate or exact solutions. A great deal of work has been done to obtain approximate solutions to the Navier-Stokes equations for incompressible swirling flow. The method of obtaining these solutions involves the introduction of perturbation and subsequent linearization of the resulting equations. This technique was used by Görtler [6], Talbot [7] and Newman [8] to investigate steady, swirling flow motions. Lewellen [9] linearized the incompressible Navier-Stokes equations and used the perturbation technique to obtain the results for both the cases of non-rotating and strongly rotating confined vortex flows. An analytical solution for the axial decay of a given swirl was presented.

With advances in computer technology, numerical methods are

becoming more powerful in seeking approximate solutions. An approximate solution can generally be attempted either by solving the equations of motion numerically or by introducing valid assumptions to simplify the complex flow equations to a solvable form.

In 1940, Burgers and Rott [10, 11] discussed the dissipation of a vortex of infinite extent using the cylindrical coordinates r, ϕ and z with the corresponding velocity components V_r, V_ϕ and V_z. They assumed axial and radial velocities of the form $V_r=-ar$ and $V_z=2az$ which led to an explicit solution for V_ϕ. Later, Donaldson and Sullivan [3,12] introduced a more general case of a solution for V_z, namely, $V_z=zf(r)$. Solutions applicable only to laminar vortex motion were obtained numerically using the boundary conditions applied specifically to their problems. Farris [13] studied both theoretically and experimentally the interaction of a vortex with a stationary surface. Examination of the numerical results over a wide range of parameters led to interesting conclusions about the sensitiveness of the entire flow field to the amount of radial flow.

An alternative approach that has been used to achieve exact solutions is to make use of the method often connected with the boundary layer theory by performing order of magnitude analysis to simplify the equations of motion.

Recently, Mack [14], King [15], Weber [16], Rott [17] and

Ostrach and Loper [18] have considered the development of the boundary layer on a finite disc or on a vortex chamber end wall for a swirling flow. Long [19, 20] also presented the numerical results of an integration by simplifying the equations of motion within the core of a vortex. Mention should be made of the work of Wormley [21] in which a momentum integral analysis is presented for incompressible, steady, axisymmetric flow in a short vortex chamber. Only the annular region was studied in his work with consideration being given to the interaction occurring between the inviscid vortex flow and the viscous end wall boundary layer.

Many investigators have attempted to interpret the experimental results obtained from actual viscous vortex motion. Einstein and Li [22] used the parameter of apparent viscosity to represent complex turbulence and viscous effects in actual vortex flow. Rott [11] also discussed the inclusion of the variable eddy viscosity to explain phenomena associated with natural meteorological disturbances, while Squire [23] assumed the turbulent eddy viscosity to be proportional to the vortex strength ($\varepsilon \propto r_p^n v^{1-n}$, where n is some exponent) in his study of the decay of the trailing vortex system behind an airplane. Ross [24] studied especially the turbulence level in vortex chambers and determined an effective turbulent-to-laminar shear ratio ranging from 10 to 10^3. Lately, Kwok [25] achieved a closed form solution of the Navier-Stokes equations applicable to the problems of a swirling, incompressible

flow within a thin cylindrical chamber of aspect ratio 50. He also discussed that the apparent viscosity varies throughout the vortex flow. Thinh [26] developed an analysis of the confined vortex motion using the concept of apparent viscosity. Only the annular region of the vortex chamber was studied. By comparing the existing experimental data with theoretical results, Thinh was able to establish the relationship between apparent viscosity with the velocity profiles within the annular region of the vortex chamber.

The present investigation is a continuation of Thinh's work [26] extended into the inner core region of a confined vortex flow. This was initiated following an interesting finding from Kwok's work [25]. In his work, Kwok obtained a closed form solution of the Navier-Stokes equations for confined vortex flow. Two cases were treated: first, the general case where the axial velocity in the exit core of the vortex is considered dependent on radius, and second, the special case where axial velocity is assumed uniform. He introduced a non-dimensional parameter α^* which is defined as the ratio of flow rate Q to the product of $2\pi\nu_a h$ where ν_a is the apparent kinematic viscosity and h is the chamber height. It was interesting to learn from Kwok's experimental measurements that flow in a vortex chamber of aspect ratio 50 corresponds fairly closely to that predicted by a theoretical curve calculated from $\alpha^* = 1.8$. In other words, this represents a value of apparent kinematic viscosity of approximately 6000 ν, where ν is the kinematic viscosity of the

operating fluid. Such a magnitude of apparent viscosity has been surmised for some time, as evident from Schlichting [27] who mentions that "... the effects caused by it (turbulent mixing motion) are as if the viscosity were increased by factors of one hundred, ten thousand or even more". Thinh [26] substantiated Kwok's finding by developing an analytical study of the vortex motion in the annular region with the apparent viscosity factor. The numerical solutions were compared with those of existing experimental measurements by Savino [28]. The analytical results proved that the values of apparent viscosity seriously affect the velocity profiles within the vortex chamber. The results also show that the apparent viscosity varies from 7000 μ at the vortex chamber periphery to 4500 μ at the orifice exit plane, where μ is the operating fluid viscosity. The main intention of the present investigation is to continue studying the behaviour of the apparent viscosity in the inner core region of the vortex chamber.

1.2 Outline of the Investigation

The aim of the present study is to investigate analytically the swirling flow of a short cylindrical chamber of large aspect ratio (ratio of chamber diameter to chamber height).

The main objective of this investigation is to develop explicit mathematical relationships between various flow parameters

of confined vortex flow in short cylindrical chambers. The analysis will be carried out by dividing the whole vortex flow field into two separate regions, namely the outer and inner regions. The boundary conditions at the interface are matched by assuming that the tangential velocity, the tangential shear and the static pressure remain continuous. Theoretical analysis will be matched with published experimental data to establish the magnitude and behaviour of the apparent viscosity throughout the flow field. It is believed that the results will be of engineering interest when predicting flow patterns for many vortex flow phenomena.

The results of the investigation will be presented as follows:

The derivation of a mathematical model for incompressible, swirling flow of a short cylindrical chamber which has a small central exhaust orifice will be presented in Chapter 2. Wormley's theoretical technique [21] for turbulent flow will be adapted and extended to include the apparent viscosity factor for the annular region. Appropriate boundary conditions and velocity profiles will be discussed. For the inner core region, the technique of separation of variables will be used to transform the equations of motion into a set of ordinary differential equations which can be solved by numerical methods.

Chapter 3 presents a detailed description of the experimental investigation conducted by Savino and Keshock [28] and Luh [29]. Both theoretical and experimental results will be compared to obtain the best fit for the annular region. Also, a quantitative comparison will be made with results obtained for the flow field in the inner core region to fully establish the magnitude and behaviour of apparent viscosity of confined vortex flow in short cylindrical chambers with large aspect ratio.

Multi-cell vortex will be discussed in Chapter 4.

CHAPTER 2

THEORETICAL ANALYSIS

2.1 Initial Assumptions of the Flow Model

In order to gain insight into the very complex phenomena of confined vortex flow in a short cylindrical chamber, it is essential that the Navier-Stokes equation be solved directly. However, the Navier-Stokes equations are distinguished by the scarcity of their solution due to the highly non-linear characteristic of the mathematical expression. As a result, certain realistic assumptions must be made to reduce these equations to a solvable form.

In this investigation of vortex flow in the annular and core regions, the flow is assumed to be steady and incompressible. It is also assumed that the vortex flow axis coincides with the geometric axis of the cylindrical chamber.

2.2 Equation of Motion

Neglecting body force, the Navier-Stokes equation for the mean motion of incompressible turbulent flow in Cartesian coordinates is given in Schlichting [27] as:

$$\rho\left(u\frac{\partial u}{\partial x} + v\frac{\partial u}{\partial y} + w\frac{\partial u}{\partial z}\right) = -\frac{\partial p}{\partial x} + \nabla(\mu\nabla u) - \rho\left(\frac{\partial u'^2}{\partial x} + \frac{\partial u'v'}{\partial y} + \frac{\partial u'w'}{\partial z}\right) \quad (1a)$$

$$\rho\left(u\frac{\partial v}{\partial x} + v\frac{\partial v}{\partial y} + w\frac{\partial v}{\partial z}\right) = -\frac{\partial p}{\partial y} + \nabla(\mu\nabla v) - \rho\left(\frac{\partial u'v'}{\partial x} + \frac{\partial v'^2}{\partial y} + \frac{\partial v'w'}{\partial z}\right) \quad (1b)$$

$$\rho\left(u\frac{\partial w}{\partial x} + v\frac{\partial w}{\partial y} + w\frac{\partial w}{\partial z}\right) = -\frac{\partial p}{\partial z} + \nabla(\mu\nabla w) - \rho\left(\frac{\partial u'w'}{\partial x} + \frac{\partial v'w'}{\partial y} + \frac{\partial w'^2}{\partial z}\right) \quad (1c)$$

where $$\nabla^2 = \frac{\partial^2}{\partial x^2} + \frac{\partial^2}{\partial y^2} + \frac{\partial^2}{\partial z^2} \quad (2)$$

Eqn. (1) is identical with the steady-state Navier-Stokes equations for the laminar case, except that there are additional terms depending on the turbulence of the stream. The flow fluctuations may be interpreted as additional surface stresses and Eqn. (1) can be expressed as:

$$\rho\left(u\frac{\partial u}{\partial x} + v\frac{\partial u}{\partial y} + w\frac{\partial u}{\partial z}\right) = -\frac{\partial p}{\partial x} + \nabla(\mu\nabla u) + \left(\frac{\partial \sigma x}{\partial x} + \frac{\partial \tau xy}{\partial y} + \frac{\partial \tau xz}{\partial z}\right) \quad (3a)$$

$$\rho\left(u\frac{\partial v}{\partial x} + v\frac{\partial v}{\partial y} + w\frac{\partial v}{\partial z}\right) = -\frac{\partial p}{\partial y} + \nabla(\mu\nabla v) + \left(\frac{\partial \tau xy}{\partial x} + \frac{\partial \sigma y}{\partial y} + \frac{\partial \tau yz}{\partial z}\right) \quad (3b)$$

$$\rho\left(u\frac{\partial w}{\partial x} + v\frac{\partial w}{\partial y} + w\frac{\partial w}{\partial z}\right) = -\frac{\partial p}{\partial z} + \nabla(\mu\nabla w) + \left(\frac{\partial \tau xy}{\partial x} + \frac{\partial \tau yz}{\partial y} + \frac{\partial \sigma z}{\partial z}\right) \quad (3c)$$

It is noted that the components of the mean velocity of turbulent flow satisfy the same laminar flow equations, except that the laminar stresses must be increased by the addition of "apparent", or Reynolds stresses, in the turbulent flow. Assuming that the

apparent stresses, which are caused by the eddy viscosity "ε", have the same influence on flow as ordinary viscous stresses have on laminar flow, and also assuming that the apparent viscosity varies throughout the whole field of interest, Eqn. (2) may be written as:

$$u\frac{\partial u}{\partial x} + v\frac{\partial u}{\partial y} + w\frac{\partial u}{\partial z} = -\frac{1}{\rho}\frac{\partial p}{\partial x} + \nabla(\nu_a \nabla u) \qquad (4a)$$

$$u\frac{\partial v}{\partial x} + v\frac{\partial v}{\partial y} + w\frac{\partial v}{\partial z} = -\frac{1}{\rho}\frac{\partial p}{\partial y} + \nabla(\nu_a \nabla v) \qquad (4b)$$

$$u\frac{\partial w}{\partial x} + v\frac{\partial w}{\partial y} + w\frac{\partial w}{\partial z} = -\frac{1}{\rho}\frac{\partial p}{\partial z} + \nabla(\nu_a \nabla w) \qquad (4c)$$

where the apparent kinematic viscosity is

$$\nu_a = \frac{\mu_a}{\rho} = \frac{\mu + \varepsilon}{\rho} \qquad \text{(See Appendix A)} \qquad (5)$$

In the cylindrical coordinate system, r, ϕ and z denote the radial, tangential and axial coordinates, and V_r, V_ϕ and V_z represent the velocity components in the respective directions. For axisymmetric flow, all the derivatives with respect to ϕ will vanish. Eqns. (4), representing the motion for the incompressible fluid with apparent viscosity as a function of radius can be expressed as:

$$V_r\frac{\partial V_r}{\partial r} - \frac{V_\phi^2}{r} + V_z\frac{\partial V_r}{\partial z} = -\frac{1}{\rho}\frac{\partial p}{\partial r} - \frac{2V_r}{\rho r}\frac{\partial \mu_a}{\partial r}$$

$$+ \frac{2}{\rho r}\frac{\partial \mu_a}{\partial r}\frac{\partial}{\partial r}(rV_r) + \frac{\mu_a}{\rho}\frac{\partial}{\partial r}\left[\frac{1}{r}\frac{\partial}{\partial r}(rV_r)\right] + \frac{\mu_a}{\rho}\frac{\partial^2 V_r}{\partial z^2} \qquad (6a)$$

$$V_r \frac{\partial V_\phi}{\partial r} + \frac{V_r V_\phi}{r} + V_z \frac{\partial V_\phi}{\partial z} = \frac{1}{\rho} \frac{\partial}{\partial r} \left[\frac{\mu_a}{r} \frac{\partial}{\partial r} (rV_\phi)\right]$$

$$- \frac{2V_\phi}{\rho r} \frac{\partial \mu_a}{\partial r} + \frac{\mu_a}{\rho} \frac{\partial^2 V_\phi}{\partial z^2} \qquad (6b)$$

$$V_r \frac{\partial V_z}{\partial r} + V_z \frac{\partial V_z}{\partial z} = -\frac{1}{\rho} \frac{\partial p}{\partial z} + \frac{1}{\rho r} \frac{\partial}{\partial r} \left[\mu_a r \left(\frac{\partial V_r}{\partial z} + \frac{\partial V_z}{\partial r}\right)\right]$$

$$+ \frac{2\mu_a}{\rho} \frac{\partial^2 V_z}{\partial z^2} \qquad (6c)$$

and the continuity equation becomes:

$$\frac{1}{r} \frac{\partial}{\partial r} (rV_r) + \frac{\partial V_z}{\partial z} = 0 \qquad (6d)$$

2.3 Introduction to Dimensionless Variables

To further generalize the problem, all the variables of Eqn. (6) are made dimensionless. A reference length, r_e, which is the radius of the exit orifice of the vortex chamber, is used to reduce all the radial dimensions, the axial length z, and the boundary layer thickness δ to dimensionless coordinates.

The radial, tangential, and the axial components are made dimensionless by comparing them to the peripheral tangential velocity v_o. In the annular region, the tangential velocity component v_δ is introduced in another non-dimensional term, called

circulation, by referring it to the circulation at the periphery $v_o r_o$.

The static pressure is also made dimensionless by comparing it to twice the value of the dynamic head and the ambient pressure. Similarly, reference dimension μ, which is the operating fluid viscosity, is used to normalize the apparent viscosity μa.

These non-dimensional variables are defined as:

$$U = -\frac{V_r}{v_o} \qquad Z = \frac{z}{r_e}$$

$$V = \frac{V_\phi}{v_o} \qquad H = \frac{h}{r_e}$$

$$W = \frac{V_z}{v_o} \qquad R = \frac{r}{r_e}$$

$$U_\delta = -\frac{u_\delta}{v_o} \qquad R_o = \frac{r_o}{r_e} \tag{7}$$

$$U_s = -\frac{u_s}{v_o} \qquad \delta^* = \frac{\delta}{r_e}$$

$$P = \frac{P-P_a}{\rho v_o^2} \qquad \bar{\delta} = \frac{2\delta}{h} = \frac{2\delta^*}{H}$$

$$\Gamma = \frac{v_\delta r}{v_o r_o}$$

A Reynolds number is defined as:

$$RE = \frac{\rho v_o r_e}{\mu} \qquad \mu_A = \frac{\mu_a}{\mu}$$

The equation of motion (6) will be normalized separately for each flow region in the next Sections.

2.4 Boundary Conditions

In order to produce continuous swirling flow, fluid must be injected tangentially at the periphery of the vortex chamber. If a sufficient number of evenly-spaced injection nozzles are used to maintain the axisymmetric flow pattern, the tangential velocity at the periphery should be exactly equal to the exit velocity of the injection nozzle. This therefore defines the first boundary condition at the periphery of the vortex chamber. In non-dimensional form, this condition can be expressed as:

$$R = R_o \qquad U = U_o \qquad V = 1 \qquad P = P_o \tag{8}$$

where R_o, U_o and P_o are non-dimensional radius, radial velocity and pressure at the periphery.

In the case of swirling inviscid fluid, the tangential velocity increases to infinite at the center of a vortex. However, in real fluid flow where viscosity is involved, the tangential velocity will reach its maximum at some distance from the chamber

axis and decreases rapidly until it vanishes at the center. In other words, both the radial and tangential velocity components in actual flow must vanish at the center. This condition is defined by the following equation:

$$R = 0 \qquad U = 0 \qquad V = 0 \qquad (9)$$

2.5 Classification of Two Flow Regions

To simplify the problem, the vortex flow within the chamber is divided into two distinct regions namely the outer annular region where $r_o \geq r \geq r_e$ is bounded by the periphery of the vortex chamber and the interface of the central orifice. The inner region where $0 \leq r \leq r_e$ is bounded by the central orifice (Fig. 4).

Numerical solutions are sought first for the annular region and then for the inner core region with matching boundary conditions at the interface where $r = r_e$. It is assumed that the wall static pressure, the tangential velocity and tangential shear remain continuous across the matching surface. Due to the particular configuration for the vortex chamber used in this case, the axial velocity component in the outer annular region is assumed to be negligible as compared with the radial and tangential velocity components.

In the inner core region, since there exists a central orifice, the axial velocity therefore cannot be neglected. The problem therefore becomes much more complicated.

2.6 Outer Annular Region

2.6.1 The Flow Model

The flow within the outer annular region can be divided into two main regions: region 1, called the developing flow region and region 2 called the developed flow region (Fig. 4), similar to the system described by Kwok, et al [31]. Flow region 1 extends from the chamber's outer periphery to the point in the chamber at which all flow has entered the chamber end wall boundary layers ($R = R^*$). Flow region 2 extends from R^* to the chamber exit. Within these two regions, the flow is subdivided into a boundary layer flow on the chamber end wall, and an inviscid flow at the chamber mid-plane. In the inviscid flow region, flow is uniform and the tangential and radial velocity components are assumed to be functions of r only. In the boundary layer flow region, the flow is dependent on both r and z and the apparent viscosity is assumed to be a function of tangential velocity in the inviscid region. Strictly speaking, the apparent viscosity should be a function of the velocity vector rather than the tangential velocity component alone. However, in this particular case, the tangential velocity component is much greater than either the radial or the axial velocity components. In order to simplify

the analysis, the above assumption is made.

Since the analysis of the flow in this region is restricted to short vortex chambers, v_z is very small and the static pressure is essentially constant in the annular region and Eqn. (6c) is eliminated. Making use of the boundary layer theory by performing order of magnitude analysis, as discussed by Schlicting [27] and Brodkey [30], Eqns. (6a), (6b) and (6d) can be expressed as:

$$V_r \frac{\partial V_r}{\partial r} - \frac{V_\phi^2}{r} + V_z \frac{\partial V_r}{\partial z} = -\frac{1}{\rho}\frac{\partial p}{\partial r} + \frac{1}{\rho}\frac{\partial}{\partial z}\left[\mu_a \frac{\partial V_r}{\partial z}\right] \qquad (10)$$

$$V_r \frac{\partial V_\phi}{\partial r} + \frac{V_r V_\phi}{r} + V_z \frac{\partial V_\phi}{\partial z} = \frac{1}{\rho}\frac{\partial}{\partial z}\left[\mu_a \frac{\partial V_\phi}{\partial z}\right] \qquad (11)$$

and the continuity equation becomes:

$$\frac{\partial V_r}{\partial r} + \frac{V_r}{r} + \frac{\partial V_z}{\partial z} = 0 \qquad (12)$$

The momentum equations for the flow in the inviscid region are in the forms:

$$u_\delta \frac{\partial u_\delta}{\partial r} - \frac{v_\delta^2}{r} = -\frac{1}{\rho}\frac{\partial p}{\partial r} \qquad (13)$$

$$u_\delta \frac{\partial v_\delta}{\partial r} + \frac{u_\delta v_\delta}{r} = 0 \qquad (14)$$

2.6.2 Velocity Profiles

In order to obtain a solution to the set of equations (8-12), it is necessary to know the velocity profiles. In this case, the tangential and radial velocity profiles take the same form as presented in Wormley's work [21]:

$0 \leq z \leq \delta$

$$V_\phi = v_\delta f(\eta) \tag{15}$$

$$V_r = u_\delta f(\eta) + u_s g(\eta) \tag{16}$$

$\delta \leq z \leq h/2$

$$V_\phi = v_\delta \tag{17}$$

$$V_r = u_\delta \tag{18}$$

Where $\eta = z/\delta$ and $f(\eta)$, $g(\eta)$ are the velocity profile functions that satisfy the following conditions:

$$f(0) = 0 \qquad g(0) = 0$$

$$f(1) = 1 \qquad g(1) = 0 \tag{19}$$

It is noted that the tangential velocity profile is a single profile while the radial profile consists of two separate profiles. The $u_\delta f(\eta)$ part represents the contribution of the radial flow profile due to radial flow in the inviscid region and $u_s g(\eta)$ part

represents the contribution of secondary flow induced into the boundary layer by the strong inward pressure gradient which exists in the chamber for $v_b/u_o >> 1$. Since the tangential Reynolds numbers ($\rho v_b r_o/\mu$) for this type of flow are generally in the range of 10^4 to 10^6, then the familiar 1/7 power law distribution [27] can be applied in the numerical calculation of f (η). The choice of g (η) is dictated by the fact that g (η) = 0 for η = 1. Moreover, the first derivative of g (η) is also zero for η = 1. Consequently, the expression for f (η) and g (η) are shown as

$$f(\eta) = \eta^{1/7} \tag{20}$$

and

$$g(\eta) = 1.69\ \eta^{1/7}\ (1 - \eta)^2 \tag{21}$$

It is convenient to introduce here the definition of the constants of integration which will be useful later in making the set of equations (10-14) non-dimensionalized.

The constants of integration are defined as:

$$\alpha_1 = \int_o^1 f^2(\eta)\,d\eta \qquad \alpha_3 = \int_o^1 g^2(\eta)\,d\eta$$

$$\alpha_2 = \int_o^1 f(\eta)\ g(\eta)\,d\eta \qquad \alpha_4 = \int_o^1 g(\eta)\,d\eta \tag{22}$$

$$\alpha_5 = \int_o^1 f(\eta)\,d\eta$$

Substituting Eqns. (18) and (19) into Eqn. (20), the numerical values of α_1, α_2, α_3, α_4 and α_5 are obtained as

$$\alpha_1 = .77778 \qquad \alpha_3 = .31337$$

$$\alpha_2 = .39004 \qquad \alpha_4 = .43914$$

$$\alpha_5 = .87500$$

2.6.3 Formulation of Flow in the Annular Region

In this region, the apparent viscosity is selected as a function of tangential velocity as follows:

$$\mu_a = K_1 v_\delta^{\,n} + K_2 \qquad (24)$$

where K_1, K_2 and n are constants to be determined later by comparing analytical results with experimental data.

When the flow is assumed to be symmetric about the chamber mid-plane, the following boundary conditions are adapted:

$$\text{at } z = 0 \qquad V_r = V_z = V_\phi = 0 \qquad (25)$$

$$\text{at } z = \frac{h}{2} \qquad V_z = \frac{\partial V_r}{\partial z} = \frac{\partial V_\phi}{\partial z} = 0 \qquad (26)$$

$$\text{at } r = r_o \qquad V_r = -u_o,\ V_\phi = v_o,\ V_z = 0,\ p = P_o \qquad (27)$$

The set of equations (8-12) is solved by using the approximate momentum integral method of Schlichting [27], subjected to the boundary conditions in Eqns. (25), (26) and (27).

The continuity equation (12) is integrated from z = 0 to z = h/2 to have the following form:

$$\int_o^{h/2} \frac{\partial V_r}{\partial r}\, dz + \int_o^{h/2} \frac{V_r}{r}\, dz = 0 \qquad (28)$$

The boundary layer momentum equations are obtained by integrating Eqns. (10) and (11) across the boundary layer:

$$\int_o^{\delta} \frac{\partial V_r^2}{\partial r}\, dz - \frac{1}{r}\int_o^{\delta} (V_\phi^2 - V_r^2)\, dz - u_\delta \int_o^{\delta} \left(\frac{\partial V_r}{\partial r} + \frac{V_r}{r}\right) dz$$

$$= -\frac{\delta}{\rho}\frac{\partial p}{\partial r} + \frac{1}{\rho}\int_o^{\delta} \frac{\partial}{\partial z}\left(u \frac{\partial V_r}{\partial z}\right) dz \qquad (29)$$

$$\int_o^{\delta} \frac{\partial (V_r V_\phi)}{\partial r}\, dz + 2\int_o^{\delta} \frac{V_r V_\phi}{r}\, dz - v_\delta \int_o^{\delta} \left(\frac{\partial V_r}{\partial r} + \frac{V_r}{r}\right) dz$$

$$= \frac{1}{\rho}\int_o^{\delta} \frac{\partial}{\partial z}\left(u_a \frac{\partial V_\phi}{\partial z}\right) dz \qquad (30)$$

where u_δ and v_δ are the velocity components in the inviscid region.

The momentum integral equations for the inviscid region remain the same as Eqns. (13) and (14) since all quantities are functions

of r.

$$u_\delta \frac{\partial u_\delta}{\partial r} - \frac{v_\delta^2}{r} = -\frac{1}{\rho}\frac{\partial p}{\partial r} \tag{31}$$

$$u_\delta \frac{\partial v_\delta}{\partial r} + \frac{u_\delta v_\delta}{r} = 0 \tag{32}$$

When V_r and V_ϕ, given by Eqns. (15) and (16), are substituted into the momentum integral equations and the constants of the integration α's are defined as in Eqn. (22), five non-dimensional equations for flow region 1 are obtained, as follows:

i) Continuity equation:

$$[\alpha_5 U_\delta + \alpha_4 U_s - U_\delta]\frac{d\bar{\delta}}{dx} + [\alpha_5\bar{\delta} + (1-\bar{\delta})]\frac{dU_\delta}{dR} + \alpha_4\bar{\delta}\frac{dU_s}{dR}$$

$$= -\frac{1}{R}[\alpha_5\bar{\delta}U_\delta + \alpha_4\bar{\delta}U_s + (1-\bar{\delta})U_\delta] \tag{33}$$

ii) Boundary layer radial momentum equation:

$$+\left[\alpha_1 U_\delta^2 + 2\alpha_2 U_\delta U_s - \alpha_5 U_\delta^2 - \alpha_4 U_\delta U_s + \alpha_3 U_s^2\right]\frac{d\bar{\delta}}{dR}$$

$$+ [2\alpha_1\bar{\delta}U_\delta + 2\alpha_2\bar{\delta}U_s - \alpha_5\bar{\delta}U_\delta]\frac{dU_\delta}{dX} - \bar{\delta}\frac{dP}{dR}$$

$$+ [2\alpha_2\bar{\delta}U_\delta - \alpha_4\bar{\delta}U_\delta + 2\alpha_3\bar{\delta}U_s]\frac{dU_s}{dR}$$

$$= \frac{1}{R}\left[\frac{\alpha_1\bar{\delta}R_o^2\Gamma^2}{R} - \alpha_1\bar{\delta}U_\delta^2 - 2\alpha_2\bar{\delta}U_\delta U_s - \alpha_3\bar{\delta}U_s^2\right.$$

$$+ \alpha_5 \bar{\delta} U_\delta^2 + \alpha_4 \bar{\delta} U_\delta U_s \Big] + \frac{4K_1 r_e U_\delta}{7\rho h^2 v_o \bar{\delta}} \left[\frac{\Gamma v_o R_o}{R}\right]^n + \frac{4K_2 U_\delta r_e}{7\rho v_o h^2 \bar{\delta}} \quad (34)$$

iii) Boundary layer tangential momentum equation:

$$- [\alpha_1 U_\delta + \alpha_2 U_s - \alpha_5 U_\delta - \alpha_4 U_s] \frac{d\bar{\delta}}{dR} - [\alpha_1 \bar{\delta} - \alpha_5 \bar{\delta}] \frac{dU_\delta}{dX}$$

$$- [\alpha_2 \bar{\delta} - \alpha_4 \bar{\delta}] \frac{dU_s}{dR}$$

$$= + \frac{[\alpha_1 \bar{\delta} U_\delta + \alpha_2 \bar{\delta} U_s]}{\Gamma} \frac{d\Gamma}{dR} - \frac{[\alpha_1 \bar{\delta} U_\delta - \alpha_2 \bar{\delta} U_s + \alpha_5 \bar{\delta} U_\delta + \alpha_4 \bar{\delta} U_s]}{R}$$

$$- \frac{4 r_e K_1}{7 h^2 \rho \bar{\delta} v_o} \left[\frac{\Gamma v_o R_o}{R}\right]^n - \frac{4 r_e K_2}{7 \rho h^2 v_o \bar{\delta}} \quad (35)$$

iv) Inviscid radial momentum equation:

$$+ U \frac{dU_\delta}{dR} - \frac{\Gamma^2 R_o^2}{R^3} = - \frac{dP}{dR} \quad (36)$$

v) Inviscid tangential momentum equation:

$$U_\delta \frac{d\Gamma}{dR} = 0 \quad (37)$$

The values of these unknowns at $R = R_o$ are:

$$U_\delta(R_o) = 1.0, \quad U_s(R_o) = 0.0, \quad \Gamma(R_o) = 1.0, \quad \bar{\delta}(R_o) = 0.0$$

$$P(R_o) = \frac{p_o - p_a}{\rho v_o^2} \qquad (38)$$

The mathematical expressions of Eqns. (33) to (38) are identical to those presented by Wormley [21] except for the expressions related to shear stress which, in this case, include the eddy viscosity as a result of the turbulence. It should be noted that flow region 2 starts at a point where the radial velocity in the inviscid region reaches zero, i.e. U = 0.

A problem exists at X = 0 in starting the solution numerically because of the factor $\bar{\delta}$ in the denominator of the shear stress terms in the equations for flow regions 1 and 2. The values of the unknowns for the initial step were obtained from the work of Rott [17] who derived expressions valid for small X for the secondary flow in the boundary layer and the boundary layer thickness, as follows:

$$\bar{\delta} = \left[18.1 \frac{2r_o}{h} \frac{C_f \sqrt{X}}{\lambda^{1/4}} \right]^{4/5} \qquad (39)$$

$$U_s = 0.686 \lambda \sqrt{X}$$

where

$$C_f = f \left[\frac{\rho h u_o}{2\mu} \right]^{-1/4}$$

$$X = 1 - \frac{r}{r_o}$$

$$f = .0225$$

$$\lambda = \frac{v_o}{u_o}$$

2.7 Inner Core Region

2.7.1 The Flow Model

In the inner core region the velocity component v_z is by no means negligible due to the axial pressure differences across the central orifice. The fundamental equations describing the three dimensional flow phenomena in non-dimensional form of equations (6a-6d) are:

Radial Momentum Equation:

$$U\frac{\partial U}{\partial R} - \frac{V^2}{R} - W\frac{\partial U}{\partial Z} = -\frac{\partial P}{\partial R} + \frac{2}{RE}\frac{U}{R}\frac{\partial \mu_A}{\partial R} - \left[\frac{2}{RE.R}\cdot\frac{\partial \mu_A}{\partial R}\frac{\partial}{\partial R}(RU)\right]$$

$$-\frac{\mu_A}{RE}\frac{\partial}{\partial R}\left[\frac{1}{R}\frac{\partial}{\partial R}(RU)\right] - \frac{\mu_A}{RE}\frac{\partial^2 U}{\partial Z^2} \qquad (40)$$

Tangential Momentum Equation:

$$-U\frac{\partial V}{\partial R} - \frac{UV}{R} + W\frac{\partial V}{\partial Z} = \frac{1}{RE}\frac{\partial}{\partial R}\left[\frac{\mu_A}{R}\frac{\partial}{\partial R}(RV)\right] - \frac{2}{RE}\frac{V}{R}\frac{\partial \mu_A}{\partial R}$$

$$+\frac{\mu_A}{RE}\frac{\partial^2 V}{\partial Z^2} \qquad (41)$$

Axial Momentum Equation:

$$-U\frac{\partial W}{\partial R}+W\frac{\partial W}{\partial Z}=-\frac{\partial P}{\partial Z}+\frac{1}{RE.R}\frac{\partial}{\partial R}\left[\mu_A R\left(\frac{\partial W}{\partial R}-\frac{\partial U}{\partial Z}\right)\right]+\frac{2\mu_A}{RE}\frac{\partial^2 W}{\partial Z^2} \qquad (42)$$

and Continuity Equation:

$$\frac{1}{R}\frac{\partial}{\partial R}(RU)-\frac{\partial W}{\partial Z}=0 \qquad (43)$$

2.7.2 Velocity Profile

Due to the highly non-linear characteristics of equations (40) to (43), certain realistic assumptions must be made in order to seek the solutions to the problem.

Applying the technique of separation of variables, the velocity and pressure functions are assumed to take the following forms:

$$U=\phi(Z)\cdot G(R) \qquad (44)$$

$$V=\psi(Z)/\mu_A^m(R) \qquad (45)$$

$$W=Z^{\alpha}\cdot F(R) \qquad (46)$$

$$P=P(R)+P(Z) \qquad (47)$$

where the functions $\phi_{(Z)}$ and $\psi(Z)$ will be determined by matching the boundary conditions along the Z direction at the interface between the annular and core flow regions (see Appendix A). The function

$G(R)$, $\mu_A(R)$ and $F(R)$ therefore will represent the velocity components within the inner core region of the vortex flow field.

The assumption made in the tangential velocity function (45) was based on the work of Kwok et al [31] where a relationship between the tangential velocity at mid-plane of a vortex chamber and the apparent viscosity was successfully established. The axial velocity function (46) has been used previously by Donaldson and Sullivan [3] to describe the vortex flow field. It was found that by using different constant α values, a series of solutions for the axial velocity profile could be obtained. These were described as "multi-cell" type vortex flow. More description as well as physical interpretation of this phenomenon will be presented in the following Chapter. Eqns. (45) and (47) were taken after many selections. It was found that only under these forms the boundary conditions at the interface can be matched.

Substitution of Eqns. (44) - (47) into Eqns. (40) - (43) gives:

Radial Momentum Equation:

$$\frac{\phi\mu_A}{RE}\frac{d^2G}{dR^2} + \frac{\phi}{RE}\left[2\frac{d\mu_A}{dR} + \frac{\mu_A}{R} + \phi\cdot G\cdot RE\right]\frac{dG}{dR} + \frac{\mu_A}{RE}\left[\frac{d^2\phi}{dZ^2} - \frac{Z^\alpha F\cdot RE}{\mu_A}\frac{d\phi}{dZ} - \frac{\phi}{R^2}\right]G$$

$$- \frac{\psi^2}{R\mu_A^{2m}} + \frac{dP(R)}{dR} = 0 \qquad (48)$$

Tangential Momentum Equation:

$$- \frac{\phi\cdot\psi\cdot G}{\mu_A^m}\left[\frac{1}{R} - \frac{m}{\mu_A}\frac{d\mu_A}{dR}\right] + \frac{Z^\alpha F}{\mu_A^m}\frac{d\psi}{dZ} - \frac{1}{RE\cdot\mu_A^{m-1}}\frac{d^2\psi}{dZ^2}$$

$$- \frac{\psi}{RE}\left[\frac{m^2}{\mu_A^{m+1}}\left(\frac{d\mu_A}{dR}\right)^2 - \frac{m}{\mu_A^m}\frac{d^2\mu_A}{dR^2} + \frac{1}{R^2\mu_A^{m-1}} + \frac{1-m}{R\,\mu_A^m}\frac{d\mu_A}{dR}\right]$$

$$+ \frac{2}{RE}\frac{\psi}{R\mu_A^m}\frac{d\mu_A}{dR} = 0 \qquad (49)$$

Axial Momentum Equation:

$$- Z^\alpha \phi\, G\frac{dF}{dR} + \alpha Z^{2\alpha-1} F^2 + \frac{dP(Z)}{dZ} - \frac{2\alpha(\alpha-1)}{RE} Z^{\alpha-2}\,\mu_A F$$

$$- \frac{1}{R_e R}\left[Z^\alpha\left(\mu_A R\frac{d^2F}{dR^2} + \mu_A\frac{dF}{dR} + R\frac{dF}{dR}\cdot\frac{d\mu_A}{dR}\right)\right.$$

$$\left. - \frac{d\phi}{dZ}\left(RG\frac{d\mu_A}{dR} + \mu_A G + \mu_A R\frac{dG}{dR}\right)\right] = 0 \qquad (50)$$

and Continuity Equation:

$$\phi\left[\frac{G}{R} + \frac{dG}{dR}\right] - \alpha Z^{\alpha-1} F = 0 \qquad (51)$$

2.7.3 Boundary Conditions

The boundary condition at the center of the vortex is defined by Eqn. (9):

$$R = 0 \qquad U = 0 \qquad V = 0 \qquad (9)$$

Using expressions for the radial and tangential velocities as shown in Eqns. (44), (45), Eqn. (9) can be written as:

$$R = 0 \qquad G_{(o)} = 0 \qquad \mu_{A(o)} = \infty \qquad (52)$$

Matching the static pressure, the tangential velocity and its first derivative between the interface of the annular and the core flow regions, the results can be expressed in the following equations:

$$R = 1 \qquad U = U_{(1)} \qquad V = V_{(1)} \qquad P = P_{(1)} \qquad (53)$$

$$R = 1 \qquad G_{(1)} = \beta \qquad \mu_A = \mu_{A(1)} \qquad P = P_{(1)} \qquad (54)$$

where β is a constant.

2.7.4 Formulation of Flow in the Core Region

From Appendix A it can be seen that the function $\phi_{(z)}$ and $\psi_{(z)}$ their first and second derivatives are calculated directly with respect to the interface conditions at any location of Z. Eqns. (48) to (51) then become a set of ordinary differential equations with only one dependent parameter R.

Let

$$A = \phi_{(Z)}$$

$$A_1 = \frac{d\phi}{dZ} \qquad (55)$$

$$A_2 = \frac{d^2\phi}{dZ^2}$$

and $B = \psi_{(Z)}$

$$B_1 = \frac{d\psi}{dZ} \qquad (56)$$

$$B_2 = \frac{d^2\psi}{dZ^2}$$

Eqns. (48) to (51) become:

Radial Momentum Equation:

$$\frac{A\mu_A}{RE} \cdot \frac{d^2G}{dR^2} + \frac{A}{RE}\left[2\frac{d\mu_A}{dR} + \frac{\mu_A}{R} + AG \cdot RE\right]\frac{dG}{dR}$$

$$+ \frac{\mu_A}{RE}\left[A_2 - \frac{Z^\alpha F \cdot RE}{\mu_A} A_1 - \frac{A}{R^2}\right] G$$

$$- \frac{B^2}{R \cdot \mu_A^{2m}} + \frac{dP_{(R)}}{dR} = 0 \qquad (57)$$

Tangential Momentum Equation:

$$- \frac{ABG}{\mu_A^m}\left[\frac{1}{R} - \frac{m}{\mu_A}\frac{d\mu_A}{dR}\right] + \frac{Z^\alpha F}{\mu_A^m} B_1 - \frac{B_2}{\mu_A^{m-1} RE}$$

$$- \frac{B}{RE}\left[\frac{m^2}{\mu_A^{m+1}}\left(\frac{d\mu_A}{dR}\right)^2 - \frac{m}{\mu_A^m}\frac{d^2\mu_A}{dR^2} - \frac{1}{R^2\mu_A^{m-1}} + \frac{1-m}{R\mu_A^m}\frac{d\mu_A}{dR}\right]$$

$$+ \frac{2}{RE}\frac{B}{R\mu_A^m} \cdot \frac{d\mu_A}{dR} = 0 \qquad (58)$$

Axial Momentum Equation:

$$- AZ^{\alpha} G \frac{dF}{dR} + \alpha Z^{2\alpha-1} F + \frac{dP(Z)}{dZ} - \frac{2\alpha(\alpha-1)}{RE} Z^{\alpha-2} \mu_A F$$

$$- \frac{1}{R\,RE} \left[Z^{\alpha} \left(\mu_A R \frac{d^2F}{dR^2} + \mu_A \frac{dF}{dR} + R \frac{dF}{dR} \frac{d\mu_A}{dR} \right) \right.$$

$$\left. - A_1 \left(RG \frac{d\mu_A}{dR} + \mu_A G + \mu_A R \frac{dG}{dR} \right) \right] = 0 \qquad (59)$$

and Continuity Equation:

$$\frac{dG}{dR} + \frac{G}{R} - \frac{\alpha Z^{\alpha-1}}{A} F(R) = 0 \qquad (60)$$

In order to solve Eqns. (57) to (60) numerically, it is necessary to transform them into the following forms.

Let

$$X_1 = R \quad (a) \qquad X_5 = \frac{d\mu_A}{dR} \quad (e)$$

$$X_2 = G(R) \quad (b) \qquad X_6 = F(R) \quad (f) \qquad (61)$$

$$X_3 = \frac{dG}{dR} \quad (c) \qquad X_7 = \frac{dF}{dR} \quad (g)$$

$$X_4 = \mu_A(R) \quad (d) \qquad X_8 = P(R) \quad (h)$$

and differentiation of Eqn. (61a) gives:

$$\frac{dX_1}{dR} = 1 \qquad (62)$$

From continuity Eqn. (60), X_3' can be found as:

$$\frac{dG}{dR} + \frac{G}{R} - \frac{\alpha Z^{\alpha-1}}{A} F(R) = 0 \tag{63}$$

or

$$\frac{dX_2}{dR} = X_3 = -\frac{X_2}{X_1} + \frac{\alpha Z^{\alpha-1}}{A} X_6 \tag{64}$$

Differentiation of X_3 gives:

$$\frac{dX_3}{dR} = \frac{X_2}{X_1^2} - \frac{X_3}{X_1} + \frac{\alpha Z^{\alpha-1}}{A} X_7 = G_2 \tag{65}$$

Combining Eqns. (61d) and (61e) yields:

$$\frac{dX_4}{dR} = X_5 \tag{66}$$

Substituting Eqns. (61) into tangent[illegible]mentum Eqn.(58) gives:

$$\frac{dX_5}{dR} = \frac{A\,RE}{m}\left(\frac{1}{X_1} - m\frac{X_5}{X_4}\right) X_2 + \left(\frac{B_2}{B} - \frac{1}{X_1^2}\right)\frac{X_4}{m}$$

$$- \frac{Z^{\alpha} B_1 RE}{mB} X_6 + \left(\frac{mX_5}{X_4} + \frac{1-m}{mX_1} - \frac{2}{mX_1}\right) X_5 \tag{67}$$

Also combining Eqns. (61f) and (61g) yields:

$$\frac{dX_6}{dR} = X_7 \tag{68}$$

Axial and radial momentum Eqns. (59) and (57) now can be arranged to give:

$$\frac{dX_7}{dR} = -\frac{X_7}{X_1} - \frac{X_7X_5}{X_4} - \frac{A\,RE X_2X_7}{X_4} + \frac{\alpha RE Z^{\alpha-1}\,X_6^2}{X_4}$$

$$+ \frac{RE}{Z^\alpha X_4}\frac{dP_{(Z)}}{dZ} - \frac{2\alpha(\alpha-1)}{Z^2}X_6 + \frac{A_1}{Z^\alpha}\left[\frac{X_2X_5}{X_4} + X_3 + \frac{X_2^2}{X_1}\right] \qquad (69)$$

$$\frac{dX_8}{dR} = -\frac{AX_4}{RE}G_2 - \frac{A}{RE}\left[2X_5 + \frac{X_4}{X_1} + A\,X_2\,RE\right]X_3$$

$$- \frac{X_4}{RE}\left[A_2 - \frac{Z^\alpha RE X_6}{X_4}A_1 - \frac{A}{X_1^2}\right]X_2 + \frac{B^2}{X_1X_4^{2n}} \qquad (70)$$

The static pressure P(Z) of Eqn. (47) may be expressed in the form:

$$P(Z) = C(Z^2 - H^2) \qquad (71)$$

where C is a constant. This is based on the work of Kwok [25] and Donaldson and Sullivan [3] in which a similar function P(Z) was found. Kwok reveals that C is a constant depending on the geometric configuration of the vortex chamber. In this study, a constant C will be used whereby the given boundary conditions are satisfied.

The derivative of P(Z) with respect to Z then becomes:

$$\frac{dP(Z)}{dZ} = 2CZ \qquad (72)$$

Eqns. (62) to (72) can be solved by numerical methods with matched results at the interface between the annular and the core region as initial conditions.

CHAPTER 3

COMPARISON OF ANALYTICAL RESULTS WITH EXPERIMENTAL DATA

3.1 General

In order to establish the magnitude and behaviour of the apparent viscosity, valid experimental data must be chosen to set a guideline for matching the proposed analytical solution. A literature search revealed that few detailed measurements have been made for a confined vortex flow within a short cylindrical chamber of low aspect ratio.

Some relevant experimental investigations have been reported by Kendall [32], Savino and Keshock [28], Donaldson and Snedeker [33], Donaldson and Williamson [34], Kwok [25], Wormley [21] and Luh [29].

The experimental investigations of Kendall, Savino and Keshock, Donaldson and Snedeker involved the study of vortex motions within cylindrical chambers of various aspect ratios where the initial swirl was induced by rotation of the chamber or by peripherally aligned guide vanes. The most significant experimental finding in all these investigations was the presence of reverse flow for high initial swirls and the presence of a high degree of tur-

bulence. Donaldson and Williamson [34] later conducted detailed measurements of vortex flow in an annular cylindrical chamber of aspect ratio 6 and found that the velocity distributions corresponded closely to those found by Kendall. Kwok [25] reported experimental data on a vortex chamber with diameter to chamber height ratio of 50, with radius ratios r_e/r_o at 0.1 and 0.2. He observed the existence of reverse flow and variation of apparent kinematic viscosity within the vortex chamber.

Wormley [21] conducted experimental investigations of confined vortex flow in the annular region of short cylindrical chambers of aspect ratio of 7. The pressure profiles for various exit radii matched his analytical results fairly closely. Wormley also made a comparison of his analytical velocity profiles with data published by Savino and Keshock [20]. The comparison, limited to one specific case, showed that his analytical results for tangential and radial velocity distributions matched those of Savino and Keshock's experimental data reasonably well.

Luh [29] reported experimental measurements on a 25.4 cm vortex chamber with independently controlled tangential and radial flow inlets. Detailed measurements of the velocity profile at the exit plane of the extended orifice also revealed the existence of a strong reverse axial flow near the chamber axis.

3.2 Savino's Experimental Set-Up and Data Reduction

The experimental study by Savino and Keshock in the annular region was conducted with two main objectives: 1) to make accurate measurements of the radial and tangential velocities of a confined vortex in one particular geometry and, 2) to determine which factors are responsible for the resulting profiles.

The experimental set-up consisted of a cylindrical chamber of aspect ratio .9 as shown in Fig. 5. A series of 48 tangentially aligned guide vanes imparted a high swirl to the air as it passed into the container from the inlet plenum chamber. Air was discharged through a 5.08 cm diameter exhaust tube centered in one end wall. The other end wall was constructed with static wall taps and probe ports to measure static pressures and to sense magnitudes and directions of velocity vectors at 7 radial stations where r is equal to 2.54, 3.81, 5.08, 6.35, 7.62, 8.89 and 11.43 cm.

The experiment was conducted at a velocity ratio of 10, defined as the ratio of tangential to radial velocity at the outer periphery. At r = 14.25 cm, the mass flow rate was 0.095 kg/s at an absolute pressure of 106.7 cm of mercury. A 3-tube pitot probe was used because it is very sensitive to yaw and permits accurate velocity vector determination. The measurement of the mass flow rate through the test section was conducted with a calibrated orifice

plate accurate to within 0.5 per cent. The radial static pressures were measured relative to each other with a bank of water manometers whose accuracy was within 1.27 mm.

The experimental results are shown in Figs. 7 and 8 for tangential and radial velocity distributions. These results are used for comparison with the analytical results in the outer annular region.

3.3 Luh's Experimental Set-Up and Apparatus

The major objective of the experimental study by Luh [29] is to measure accurately the velocity profiles at the exit plane of the vortex exhaust core region. In his study, Luh utilized a vortex chamber which was designed by employing a concept similar to that of the vortex amplifier used in fluidic technology (Fig. 6). The main flow through the radial supply flow inlets and tangential flow inlets are equivalent to that of the power flow and control flow in fluid amplifier terminology respectively.

The 25.4 cm diameter vortex chamber used has a total of eight identical tangential nozzles, each .556 cm in diameter. Flow is discharged into the atmosphere through a central exhaust port. The exhaust port is designed to facilitate installation of various sizes and shapes of outlet. The experimental data illustrated in this

report is for a 8.89 cm long and 5.08 cm diameter cylindrical exhaust outlet. Experimental results are shown for the supply flow rate of .566 cu.m/min. and the control flow rate of .283 cu.m/min.

The end wall on the side of the outlet port was fabricated with a total of 22 wall static pressure taps at various radial positions. All the pressure taps were 0.016 cm in diameter. A five-hole 3-dimensional probe (manufactured by United Sensor and Control Corp., Model No. DA 125) was used and is capable of measuring yaw and pitch angles, static and total pressures simultaneously with good accuracy.

The experimental results are shown in Figs. 15 to 18. These results are used to compare quantitatively with the analytical results in the inner core region of the vortex flow field.

3.4 Results and Discussion

3.4.1 Comparison with Savino's Experimental Data of the Annular Region

The sets of equations (33) to (38) and (62) to (72) were solved numerically using the Runge-Kutta integration method. In studying the flow field of the annular region, the analytical results were used to compare with published experimental data of Savino [28] in order to clarify the fact that the apparent viscosity

does, in fact, vary throughout the vortex chamber and at the same time, to determine the magnitude of the apparent viscosity.

To carry out the critical comparison, the following procedures were used:

1. The apparent viscosity was assumed to be a function of tangential velocity at the mid-plane in the annular region; $\mu_a = K_1 v_\theta^n + K_2$, where K_1, K_2 and n are constants.

2. By a trial and error method, the constants K_1, K_2 and n were selected so that the analytical results would give a good match to the Savino and Keshock experimental data. The magnitude of the apparent viscosity μ_a was then computed.

3. The analytical results were superimposed on Savino and Keshock's experimental results, as shown in Figs. 7 and 8. In this case, they are the tangential and radial velocity distributions at 4 stations along the chamber radius. The constants K_1, K_2 and n were then defined.

Once the constants K_1, K_2 and n are defined, the velocity components, the static pressure and other conditions can be computed. The boundary values at the edge of the annular region were later used as the initial conditions for the second part of the FORTRAN

programme to analyse the flow field of the inner core region.

The matching of the analytical tangential and radial velocity distributions to Savino's experimental data as shown in Figs. 7 and 8 indicated that there are some discrepancies especially at the radial stations close to the exit orifice. This discrepancy can be explained by the fact that the flow in the vicinity of the central exit orifice is seriously affected by exit axial velocity distribution, and the theoretical model does not take into consideration the axial velocity component.

Fig. 7 shows that the tangential velocity distributions match very well with the experimental data, especially at the stations where R is equal to 2 and 2.5. The tangential flow shows almost perfect matching between the boundary layer thickness of theoretical analysis and experimental data. However, comparison of the radial velocity distributions shown in Fig. 8 do not give quite as good a matching, especially inside the boundary layer region. It is suspected that this may be due to instrumentation error when measuring the flow, and to the fact that the radial velocity was small compared to tangential velocity in the vicinity of the exit orifice. Furthermore, the radial velocity is more likely to be affected by the exit axial velocity distribution because of the relationship governing the continuity equation. Figs. 8c and 8d show a better match for radial velocity distribution. This helps to

substantiate the previous argument that these two stations are far from the exit orifice and therefore are less affected by axial flow.

Fig. 9 shows the analytical flow properties within the annular region of the vortex chamber using Eqn. (24) for apparent viscosity. The non-dimensional static pressure distribution is shown in Fig. 9a; this shows that the pressure decreases slowly from the chamber periphery to about half-way along the chamber, then decreases rapidly as the flow approaches the exit orifice. This is a very interesting result, indicating that the flow is moving towards a much more favourable pressure gradient region near the exit orifice. This is, in fact, confirmed by the results shown in Figs. 9b and 9c for the boundary layer thickness distribution and the behaviour of the apparent viscosity. Physically, it means that the vortex flow is drawn towards the centre and accelerated in accordance with the law of conservation of angular momentum; this acceleration makes the turbulence fluctuations less important and provides a favourable pressure gradient region near the exit orifice.

The dimensionless boundary layer thickness is shown in Fig. 9b and its behaviour displays some interesting features. The analytical boundary layer distribution is shown to increase as the flow moves inward; it reaches a maximum and then decreases slowly towards the centre of the vortex chamber. This may be explained by the fact that when the fluid is moving towards the central exhaust, a more favour-

able pressure gradient develops due to the rapid increase in the magnitude of both the tangential and radial velocity components. Schlichting [27] reported a similar type of solution for flow in a converging channel where he indicated a decrease in boundary layer thickness.

Fig. 9c represents the behaviour of the apparent viscosity in the annular region of a vortex chamber for our investigation. The apparent viscosity decreases from 7000μ at the periphery to 4500μ at the exit plane. This substantiates Kwok's [25] prediction that "... the apparent viscosity appears to vary with somewhat higher values nearing the periphery of the chamber and gradually decreasing towards the central orifice." He predicted that the magnitude of the apparent viscosity for a short vortex chamber would be in the vicinity of 6000μ, where μ is the normal fluid viscosity. From the physical standpoint, it may be explained that the flow initially entering the vortex chamber resembles flow along concave walls. The destabilizing effects of centrifugal forces create stationary Taylor-Görtler vortices along the wall of the chamber and therefore generate high turbulence; accordingly, the apparent viscosity at the periphery is also high. As flow approaches the central axis, vortex motions become more symmetrical and there is a large reduction in the effect of eddy viscosity in the central region [8, 35]. Coupled with the effect of a favourable pressure gradient, the apparent viscosity at the orifice exit plane is therefore lower. In

this annular region, the empirical equation of apparent viscosity, $\mu_a = .01/v_\delta^{1/3} + .00075$, is found to provide excellent predictions for flow parameters in short vortex chambers.

3.4.2 Analytical Results of the Inner Core Region

Based on Savino's experimental data at the interface between the annular and the core regions, vortex flow in the inner core region was predicted analytically using equations derived in 2.7.4 and shown in Fig. 10 to Fig. 14. The velocity distributions reveal that these results are similar to the solutions obtained by Donaldson and Sullivan [3] for the two-cell vortex flow of type III which is considered to be of special interest since most strong vortex flows tested in the laboratory as well as many meteorological phenomena such as hurricanes and tornadoes all exhibit such two-cell vortex flow characteristics. It should be emphasized that the theoretical analysis of this study is completely different from that of Donaldson and Sullivan [3] where laminar flow was assumed. In this study, a variable apparent viscosity is assumed and the radial and tangential velocity profiles are functions of both R and Z directions.

Analytical results were obtained for eleven stations for dif-

ferent axial positions of the vortex chamber. Three stations were chosen in the top boundary layer region corresponding to the top wall region A* (see Fig. 4). Five stations were selected in the mid-plane region B* and again three stations were chosen in the exit orifice region C*. Since analytical results for the stations in each region have very similar trends of characteristics, only one typical set of results for each region is presented.

Fig. 10 presents the results of the axial velocity components at different planes A, B and C of the chamber as shown. These figures show some interesting facts about the axial flow for this type of two-cell vortex flow configuration. First, they all indicate positive (outward) flow at or near the interface between the core and the annular regions and then strong negative (reverse) flow near the center. Physically, it means that according to the principle of conservation of angular momentum, the tangential velocity component increases as the flow spirals its way towards the center. The radial velocity also increases as the radial velocity components move inwards because of the decrease in the radial cross section area. The increase in tangential and radial velocity components will therefore result in a decrease in static pressure which eventually will reach a level below that of the ambient. At that moment, the ambient air will be sucked into the core to form a strong reverse flow.

The axial flow near the top wall of the chamber as indicated by curve A, has a strong reverse flow entering at the center of the vortex chamber and mostly turns into radial flow in a manner similar to that of radial flow of a jet when impinging on a flat plate. The numerical solutions for the velocity components near the top wall are very difficult as can be appreciated when the wall shear is taken into consideration together with complex flow equations. Considerable computer time was consumed and in particular, the initial slope of the axial velocity function F(R) is extremely critical. Curves B and C illustrate the radial distributions of the axial velocity at the mid-plane and exit orifice regions respectively. The magnitude of positive axial flow at plane C is obviously higher than that of A and B; it represents the conversion of all the radial velocity components into the axial velocity in that plane plus all the axial velocities from the planes above. It should be noted that special precautions have been taken in the computation to check out that the continuity equation at different planes is satisfied.

The radial distribution of tangential velocities for planes near the top wall (A), the mid-plane (B) and the orifice exit (C) are shown in Fig. 11. As explained above, the tangential velocity shows trends of increasing rapidly in the inner core region according to the principle of conservation of angular momentum. It must however satisfy the boundary conditions at the axis of the chamber where tangential velocity should be equal to zero. Fig. 11 shows that the

tangential flow near the top wall increases rapidly to a maximum at radial location of about R=0.1, then decreases, also rapidly, to zero at the axis of the chamber. The boundary condition is therefore satisfied. The tangential velocity distributions at the mid-plane B reach a much higher magnitude than that of A because they are less affected by the wall shear.

From the physical standpoint, the flow in the "eye" of the vortex defined as the region inside the maximum tangential velocity, exhibiting an essentially solid-body-like flow pattern may be explained by the fact that the axial reverse flow which is being sucked into the vortex core region has no angular momentum initially. As the flow enters into the center region and the region very near the top wall, it receives more and more angular momentum from the vortex flow. The total tangential momentum in the "eye" is imparted to it by fluid viscosity and some other complex momentum exhange phenomena observed in turbulent flow. In many experimental investigations of confined vortex flow of liquid, in particular, the work of Kwok and Farag [36], the air core in the "eye" region has the physical configuration identical to that represented by the theoretical results shown in Fig. 11.

The results of the radial velocity distributions are shown in Fig. 12. The positive sign used for radial flow indicates the fluid flow direction towards the center. At the region of the top wall,

curve A, the radial velocity near the center has a rather high value. This is quite reasonable since the strong incoming axial flow has to change its direction when obstructed by the closed top wall of the chamber.

According to the analysis substantiated by experimental data, all the outflow from the annular region passes through the top wall and exit orifice regions. Therefore, the magnitude of a radial velocity for plane B at the interface is zero. Fig. 12 shows that most of the radial flow component is negative (i.e. away from the center) so that the entrained flow in the "eye" can make its way out of the chamber as shown in Fig. 13. For the top wall and exit orifice regions represented by curves A and C, there are positive radial velocity components indicating the net flow leaving the annular region.

The vortex flow configuration as shown in Fig. 13 was first theoretically described by Donaldson and Sullivan [3] as a "two-cell" vortex. The negative axial velocity at the center coupled with strong positive axial velocity near the interface induce strong secondary vortex in the core region. It may be imagined that the secondary vortices are grouped in the form of a "doughnut" with its geometric axis corresponding to that of the vortex chamber. This flow pattern is superimposed with the tangential velocity components shown in Fig. 11. It can be seen from Fig. 13 that the reverse flow entering the center region eventually works its way out and mixes with the out-

flow from the annular region. The reverse axial flow component around the axis of the chamber has maximum kinetic energy as it enters the inner core region. When it impinges on the top plate and converts the axial velocity component to a radial component, the resultant velocity virtually "pushes" the incoming flow from the annular region. The positive radial velocity from flow leaving the annular region and the negative radial velocity from the entrained flow must eventually reach a point where they become zero. Fig. 12 and Fig. 13 substantiate this argument.

This highly complex flow configuration represents strong momentum exchanges and the magnitude of the apparent viscosity is theoretically predicted as presented in Fig. 14. It is very interesting to note that its behaviour again confirms predictions made by Kwok [25] and Schlichting [27]. Kwok predicted that the apparent viscosity would decrease as the flow moves inward and would increase rapidly as it approaches the chamber axis. As explained before, the flow initially entering the vortex chamber in the annular region resembles flow along concave walls. Due to the existence of the Taylor-Görtler vortices along the wall of the chamber, high turbulence was generated; therefore, the apparent viscosity at the periphery is very high. As flow approaches the central axis, the vortex motion becomes more symmetrical and there is a large reduction in the effect of eddy viscosity. Coupled with the effect of a favourable pressure gradient, the apparent viscosity in the inner

region therefore becomes still lower.

It is noted however, that the curve representing the apparent viscosity of the top wall region reaches a minimum value corresponding to the maximum radius of the vortex eye region. The apparent viscosity increases rather dramatically as the flow approaches the axis of the vortex chamber. The other two curves represent the apparent viscosity for the center and exit orifice regions. The minimum value of the apparent viscosity occurs at the point corresponding to the maximum tangential velocity. The magnitude of the apparent viscosity in the flow region inside the eye of the vortex is so high that it forces the vortex motion into a solid-body rotation.

3.4.3 Comparison with Luh's Experimental Measurements

The vortex flow in the outer annular and inner core regions of Luh's vortex chamber was predicted analytically using equations derived in 2.7.4. Results at the mid-plane and exit orifice regions were obtained for the inner core region. These analytical results are used to compare with the only available experimental results by Luh which were measured at the outlet of a 8.89 cm cylindrical pipe downstream of the exhaust port. However, by carefully working on both sets of theoretical and experimental data it was possible to reconstruct the actual flow pattern in the vortex core region. This exercise serves to provide a better understanding of the complex

flow pattern.

Based on the procedure developed for matching Savino's experimental data with the theoretical analysis, the technique was applied in comparison with Luh's data using his wall static pressure measurements in the annular flow region. The matching of theoretical pressure distribution with his experimental results is shown in Fig. 15a. Once the wall pressure curve is theoretically identified, the boundary layer thickness and apparent viscosity distributions can be predicted using Eqns. (33) to (38). Although Luh's experimental vortex chamber is not exactly identical to that of Savino's, they both achieved very similar vortex flow configurations described earlier as of the two-cell type. Both the boundary layer thickness and apparent viscosity exhibited similar characteristics.

The empirical expression for the apparent viscosity based on Luh's data is $\mu_a = K_1 v_\delta^n + K_2$, where $n = -1/3$, $K_1 = .01$ and $K_2 = -.002$. With this expression, the fluid properties at the interface between the annular and inner core region can be established. These data are then used as the initial conditions for theoretical prediction of flow pattern in the core flow region. As mentioned earlier, in matching the annular and core flow regions, all fluid flow properties (i.e. pressure and velocity components) must be continuous and the shear force as well must be exactly equal as both sides of the interface.

Both theoretical and experimental data of the axial, tangential and radial velocity distributions are shown in Figs. 16, 17 and 18 respectively. Based on these results, the actual vortex flow pattern is graphically presented in Fig. 19 to illustrate the actual complex flow pattern. The theoretically predicted axial velocity distributions at planes B and C as shown in Fig. 16 show basically a two-cell vortex flow characteristic quite similar to the cases predicted by Savino. As flow enters the vortex chamber at cross-section C, the reverse axial velocity near the central axis is quite strong. As the reverse flow reaches plane B, some of the reverse axial velocity component has to change to radial component as illustrated in Fig. 19. As a result, there is a marked decrease in the magnitude of the reverse axial velocity from plane C to B. It is also quite obvious to expect that the positive axial velocity (outflow) component at plane C should be higher than that of B because all the net outflow of the chamber including all the entrained flow in the core passes through plane C, while only part of the net flow goes through plane B.

It is also of interest to note that there is a "hump" in the positive axial velocity distribution in plane C. Physically, it can be seen that the entrained velocity at the core must find its way out of the chamber and also all the flow from the annular region of the vortex chamber must leave through the same plane C. These flows are moving in at an opposite radial direction as illustrated in Fig. 19;

consequently, the positive axial velocity distribution resembles that of a "camel's back". The theoretical prediction of axial velocity distribution which agrees so well with simple physical reasoning of this highly complex flow pattern is most encouraging. Unfortunately, there is no available experimental data at planes B and C and the only set of data presented by Luh is at D which is 8.89 cm downstream of the chamber exit plane C.

From Fig. 19, it is not difficult to envisage that the positive axial velocity component is highest at plane D. The two-celled vortex, as described earlier, resembles that of the wise coils in the shape of a "doughnut". The secondary vortices are of the "forced" nature and the positive axial velocity component at plane D, will undoubtedly exhibit solid body rotation characteristics as shown by Luh's experimental data in Fig. 16.

Fig. 17 shows the analytical results for tangential velocity at the mid-plane and the exit region of the inner core region. It also shows the experimental tangential velocity of Ref. [29] at the exhaust port of the extended cylinder. The analytical tangential velocity in the inner core region has similar trends as that of Savino's and both cases exhibit the same two-celled vortex characteristics. Tangential velocity components have a higher magnitude in plane C than in B. From previous discussion for flow in the annular region, it can be seen that most flows are leaving that region through

the upper and lower boundary layers. Therefore, total tangential momentum carried by flow in plane C would definitely be higher than that of the mid-plane at B because of the additional tangential momentum carried by flow through the lower boundary.

The magnitude of tangential velocity at the exit port of the extended cylinder measured at plane D is very much lower than that of the theoretically predicted value at the vortex chamber exit (plane C). The measurement of tangential velocity component indicates the trend that the flow initially decreases very rapidly until it reaches the region where the axial reverse flow starts. The reverse or entrained flow which is being sucked into the core of the vortex has no initial tangential momentum and as a result, all its tangential momentum is imparted to it by the exhaust flow. Therefore, it is reasonable to expect that the vortex motion in this region resembles that of a solid-body rotation as also shown from the experimental data. Due to the high turbulence level associated with flow leaving the chamber and the transfer of tangential momentum from the exhaust flow into the entrained flow, it is reasonable to expect that a significant drop in the magnitude of tangential velocity component can be expected at plane D. However, further experimental investigations would be required and theoretical analysis in the cylindrical extension section of the vortex exhaust port region should be carried out to better understand the phenomenon.

Fig. 18 shows the experimental radial velocity components at the exhaust port of a 8.89 cm cylinder superimposed on the analytical results calculated at the mid-plane and at the exit orifice of the vortex chamber. The magnitude of radial velocity components in the inner core region in planes B and C are very small and behave in a manner very similar to that described for Savino's case. The measured data shown in Fig. 18 indicate the radial velocity component fluctuates from negative (away from the center) to positive (towards the center) and then to negative again. Although the actual magnitude of the radial velocity component is rather small, they are transformed into streamline flow patterns together with the axial velocity component as illustrated in Fig. 19. By combining the existing experimental data and the results of the analytical, a vivid description of the real flow configuration of the two-cell vortex flow pattern is presented.

Fig. 20 shows the apparent viscosity distributions at planes B and C for experimental data of Ref. [29]. The curves indicate a gradual decrease in apparent viscosity as flow is approaching the center. The rate of decrease tapers off when reverse flow region starts. However, as the vortex flow approaches the center, there is a dramatic increase in the apparent viscosity since the tangential velocity component would inevitably become zero at the center of the vortex.

Theoretical results on the distribution of apparent viscosity as shown in Figs. 14 and 20 represent a first ever attempt to predict the magnitude of the apparent viscosity in the inner core region of a complex vortex flow pattern. The gradual decrease in apparent viscosity as flow leaves the annular region does seem to make sense from the physical standpoint. As flow swirls in towards the center, tangential velocity increases and achieves a much smoother and more symmetrical flow pattern. Moreover, the increase in velocities creates a low pressure core region, and the favourable pressure gradient further dampens the turbulence. It may also be noticed that there is a significant change in the decrease rate as well as the magnitude of the apparent viscosity when the reverse flow starts. This may be explained by the fact that the entrained flow in the core of the vortex has very low turbulence to start with, and its vortex motion is actually "forced" by the exhaust vortex flow from the annular region. Therefore, it is quite reasonable to expect that the actual magnitude of the apparent viscosity will be rather low.

In real vortex flow, the tangential velocity component in the region near or at the center, must vanish. This is in contrast with an idealized inviscid free vortex solution where the tangential velocity at the center of the vortex reaches infinity. It is therefore not surprising to see that the theoretically predicted magnitude of the apparent viscosity shoots up dramatically. Some complex form of momentum exchange mechanism must have taken place to slow down the flow velocity at the center.

CHAPTER 4

MULTI-CELL VORTEX FLOW

4.1 General

In analysing confined vortex flow in the inner core region, the axial velocity profile has been assumed to be $W = Z^{\alpha}F(R)$ where α is a positive integer. In the previous analysis, α has been assumed to be unity and namely a two-cell vortex flow configuration is obtained. Donaldson and Sullivan [3] also achieved the prediction of multi-cell vortex flow configuration in their theoretical analysis. However, there is no follow-up of the investigation because they believed that these vortex phenomena may, in all possibility, not be true in the finite scale of laboratory apparatus.

The analysis developed for this investigation which has been successfully used as a tool to explain the two-cell type vortex flow can also be used to analytically predict the flow fields of multi-cell vortex phenomena. When the pressure differential at the exit of the vortex is very high (i.e. both the supply pressure to the vortex chamber and the back pressure are high), it is reasonable to expect that the variation of the axial velocity component along the axial coordinate Z will also be correspondingly high. In other words, the

exponent α can easily be greater than unity which is the value assumed for two-cell vortex flow solution. In this Chapter, a theoretical investigation of computer programming of vortex core flow for α equals two and three is described. The theoretical results are plotted and analysed.

4.2 Analytical Four-Cell Vortex Flow

When $W = Z^2F(R)$, analytical results of the axial, tangential and radial velocity distributions are calculated, based on Savino's experimental data at the interface between the annular and the core region, and are shown in Figs. 21, 22 and 23 respectively. Based on these results, a schematic diagram of the flow pattern is constructed and shown in Fig. 24.

As stated previously, when the back pressure is very high, and a very strong swirl is associated with the vortex flow, then a situation may develop where the axial velocity is very much a function of the axial coordinate Z. In the case of $W = Z^2F(R)$, it can be seen from Fig. 21 that a very strong positive outflow component is realized around the axis of the vortex flow. Initially, the large pressure gradient between the ambient and the vortex core flow region starts a very strong reverse flow. Flow entering the vortex core from the ambient must find its way out of the chamber. As indicated in Fig. 24, the net vortex flow leaving the annular region coupled with the

entrained reverse flow creates a four-cell vortex flow configuration. The flow may be visualized as containing two concentric doughnut shaped vortex rings, with one inside the other. The outer doughnut consists of a series of "forced vortices" where rotation is energized by the exit flow from the annular region and the entrained flow through the core. Depending on the strength of the outer ring vortices, they induce the rotation of the inner vortex ring whose rotation is in the opposite direction to the outer vortices as illustrated in Fig. 24. Superimposed on these vortex rings is the tangential velocity distribution shown in Fig. 22.

The very high tangential velocity component near the axis indicates a severe drop in static pressure. The low static pressure coupled with high ambient back pressure results in strong entrain or reverse flow. In other words, the stronger the vortex flow leaving the annular region, the stronger will be the entrained flow. This has a direct effect on the strength of the forced vortices of the outer vortex ring in the core region. The vortices in the inner vortex ring are in turn induced by the vortices of the outer ring in a manner similar to that of a gear train with each consecutive gear rotating in opposite directions. The direction of rotation can also be realized from the radial velocity distribution curves shown in Fig. 23.

In order to better understand the radial velocity distribution curve, it may be instructive to consider the projected linear velocity

of a point moving around a circular path as in simple harmonic motion. The magnitude of the velocity of the point when it is projected onto the plane perpendicular to the path must necessarily resemble that of a sine wave. Curves in Fig. 23 clearly indicate such a trend and substantiate the interpretation of the flow model shown in Fig. 24.

Theoretically predicted apparent viscosity (Fig. 25) indicates the general decreasing trend similar to that of the previous two-cell model. However, the magnitude of apparent viscosity in the outer vortex ring is higher than that of the inner ring whose flow consists entirely of the entrained (reverse) flow which has a much lower turbulence level. The flow in the outer vortex ring consists partly of the entrained flow and partly of the turbulent exhaust flow from the annular region. The apparent viscosity at that point is therefore higher. As the computer program calculates the point near or at the center of the vortex, the tangential velocity must approach zero at the center according to the boundary condition. Since the apparent viscosity is considered to be an inverse type function of the tangential velocity component, its magnitude has to assume a dramatic increase when the tangential velocity component approaches zero.

4.3. Analytical Six-Cell Vortex Flow

Fig. 26 presents analytical results of the velocity distributions for the vortex flow based again on Savino's data when α is equal to 3 in the expression for axial velocity distribution. The complicated flow pattern is constructed based on the velocity distribution curves and is shown in Fig. 27. The graphical six vortex rings superimposed on the main swirl flow while the previous case, where $\alpha = 2$, has only four rings. The doughnut shaped rings have generally the same characteristics and rotate in alternating directions similar to the cases described earlier, except in this configuration where six rings are involved.

The axial velocity distribution shows a very strong reverse flow occuring at the axis of the chamber. This phenomenon may occur when there is a large pressure differential between the ambient and the center of the vortex core. The six-cell flow configuration is clearly indicated by the axial and radial velocity components. The strength of the vortices in different doughnut rings is mainly dependent on the entrained flow in the center of the vortex. In this particular case, the smallest vortex ring in the center has the maximum velocity.

Superimposed on these vortex rings, is the strong tangential velocity component. In this case, it is clearly identifiable that the

tangential velocity reaches its maximum at R = 0.2. The entrained flow in the central core inside the point of maximum tangential velocity assumes the "forced" vortex flow configuration. Theoretical prediction of the apparent viscosity in Fig. 28 shows the similar decreasing trend as that for the two- and four-cell models. However, the decreasing trend reverses itself when the tangential velocity reaches its maximum.

It is doubtful whether this type of six-cell vortex flow configuration will be realized in actual practice. In most cases, the magnitude of velocity components will be so high that they easily reach beyond the sonic speed. When this happens, effects of compressible flow and shock wave phenomenon will take place. However, purely from the academic point of view, it is interesting to note the capability of this analytical model to predict such a complex vortex flow configuration.

CONCLUSIONS

The swirling, incompressible flow in a short cylindrical chamber has been investigated analytically and the results compared with Savino's and Luh's experimental data. Based on these comparisons, it is possible to understand the behaviour and magnitude of the apparent viscosity for confined vortex flow in both the annular and the inner core regions.

The theoretical phase of the investigation was concerned with the development of a non-dimensional set of differential equations for the vortex flow within a short cylindrical chamber. The whole vortex flow field was divided into two regions, namely an annular and an inner region. Wormley's analytical technique was further extended to include the apparent viscosity factor for the annular region. The technique of separation of variables was applied to formulate the equations of motion in the inner core region. Differential equations were solved numerically using the Runge-Kutta method. All the fluid properties including the apparent viscosity were matched at the boundary between the annular region and the core flow region of the vortex chamber.

The analytical results show the actual trend of the apparent viscosity variation across the whole vortex chamber. In comparison with the existing experimental data, the magnitudes of the apparent viscosity were obtained and further substantiate the earlier prediction

by Kwok [25].

Flow characteristics and velocity profiles for the whole chamber were analytically obtained for two-cell as well as for multi-cell vortex flows.

REFERENCES

1. Gartshore, I.S., "Recent Work in Swirling Incompressible Flow", National Research Council of Canada, Aeronautical Report LR-343, 1962.

2. Gartshore, I.S., "Some Swirling Flow Phenomena and Applications", National Research Council of Canada, DME/NAE Quarterly Bull., No. 1962 (2), July 1962.

3. Donaldson, C. du P. and Sullivan, R.D., "Examination of the Solutions of the Navier-Stokes Equations for a Class of Three-Dimensional Vortices", Aero Research Associates of Princeton AFOSR, TN 60-1277, October 1960.

4. Küchemann, D., "Report on the International Union for Theoretical and Applied Mechanics", (I.U.T.A.M.), Symposium on Concentrated Vortex Motions in Fluids, J. of Fluid Mech., Vol. 21, Part 1, pp. 1-20, 1965.

5. Lewellen, W.S., "A Review of Confined Vortex Flows", NASA CR-1772, July 1971.

6. Görtler, H., "Theoretical Investigations of the Laminar Boundary Layer. Problem II: Decay of Swirl in an Axially Symmetrical Jet, Far from the Orifice", Final Report, AFOSR, TN 54-164, March 1954.

7. Talbot, L., "Laminar Swirling Pipe Flow", J. Appl. Mech., Vol. 21, No. 1, 1954.

8. Newman, B.G., "Flow in a Viscous Trailing Vortex", Aero. Quart., Vol. 10, May 1959.

9. Lewellen, W.S., "Linearized Vortex Flows", AIAA Journal, Vol. 3, No. 1, pp. 91-98, January 1965.

10. Burgers, J.M., "A Mathematical Model Illustrating the Theory of Turbulence", Adv. in Appl. Mech., Vol. I, pp. 171-199, Academic Press, 1948.

11. Rott, N., "On the Viscous Core of a Line Vortex", ZAMP, Vol. IXb, pp. 543, 1958.

12. Donaldson, C. du P. and Sullivan, R.D., "Behaviour of Solutions of the Navier-Stokes Equation for a Complete Class of Three-Dimensional Viscous Vortices", Proc. 1960 Heat Transfer and Fluid Mech. Inst., Standford University Press, pp. 16-30.

13. Farris, G.J. et al, "A Theoretical and Experimental Study of Confined Vortex Flow", Trans. of the ASME, J. of Appl. Mech., Vol. 36, Series E, No. 4, December 1969.

14. Mack, L.M., "Laminar Boundary Layer on a Disk of Finite Radius in a Rotating Flow, Part I", Jet Propulsion Laboratory Report TR-32-224, 1962.

15. King, W.S., "Momentum Integral Solutions for the Laminar Boundary Layer on a Finite Disk in a Rotating Flow", Aerospace Corp., Report ATN-63 (9227)-3, 1963.

16. Weber, H.E., "Boundary Layer Inside a Conical Surface Due to Swirl", J. of Appl. Mech., Vol. 23, Trans. ASME, Vol. 78, Series E, 1956.

17. Rott, N., "Turbulent Boundary Layer Development on the End Walls of a Vortex Chamber", Aerospace Corp., Report ATN-62 (9202)-1, 1962.

18. Ostrach, S. and Loper, D.E., "An Analysis of Confined Vortex Flows", AIAA Paper No. 66-88, 1966.

19. Long, R.R., "Vortex Motion in a Viscous Fluid", J. Meterology Vol. 15, No. 1, pp. 108-112, February 1958.

20. Long, R.R., "A Vortex in an Infinite Viscous Fluid", J. Fluid Mech., Vol. 11, pp. 611-624, 1961.

21. Wormley, D.N., "An Analytical Model for the Incompressible Flow in Short Vortex Chambers", J. of Basic Engineering, Trans. of the ASME, June 1969.

22. Einstein, H.A. and Li, H., "The Steady Vortex Flow in a Real Fluid", La Houille Blanche, Vol. 10, No. 4, pp. 483, 1955.

23. Squire, H.B., "The Growth of a Vortex in Turbulent Flow", ARC 16, pp. 666, (F.M. 2053), March 1954.

24. Ross, D.H., "An Experimental Study of Turbulence Levels in Jet-Driven Vortex Chambers", Aerospace Corp., Report No. ATN-64 (9227)-5.

25. Kwok, C.K., "Vortex Flow in a Thin Cylindrical Chamber and Its Applications in Fluid Amplifier Technology", Ph.D. Thesis, McGill University, Montreal, 1966.

26. Thinh, N.D., "An Analytical Investigation of Confined Vortex Flow Phenomena", M.Eng. Dissertation, Concordia University (SGW

Campus), Montreal, Canada, March 1971.

27. Schlichting, H., "Boundary Layer Theory", McGraw-Hill Book Co., New York, 6th ed., 1968.

28. Savino, J.M. and Keshock, E.G., "Experimental Profiles of Velocity Components and Radial Pressure Distribution in a Vortex Contained in a Short Cylindrical Chamber", NASA TN D-3072, October 1965.

29. Luh, B.S., "Experimental Study of the Exit Velocity Distribution in a Short Vortex Chamber", M.Eng. Dissertation, Concordia University (SGW Campus), Montreal, Canada, Sept. 1973.

30. Brodkey, Robert S., "The Phenomena of Fluid Motions", Addison-Wesley Publishing Company, New York, 1967.

31. Kwok, C.K., Thinh, N.D. and Lin, S., "An Investigation of Confined Vortex Flow Phenomena", Trans. of ASME, J. of Basic Engineering, Vol. 94, Series D, No. 3, September 1972.

32. Kendall, J.M. Jr., "Experimental Study of a Compressible Viscous Vortex", Tech. Report No. 32-290, Jet Propulsion Laboratory, California Institute of Technology, June 1962.

33. Donaldson, C. du P. and Snedeker, R.S., "Experimental Investigation of the Structure of Vortices in Simple Cylindrical Vortex Chambers", ARAP Report No. 47.

34. Donaldson, C. du P. and Williamson, G.C., "An Experimental Study of Turbulence in a Driven Vortex", Aero. Res. Assoc., Princeton, ARAP Tech. Memo No. 64-2, July 1964.

35. Taylor, G.I., "Fluid Friction Between Rotating Cylinders", Proc. Royal Soc. A157, pp. 546, 1936.

36. Kwok, C.K. and Farag, E.A., "Investigation of Swirling Flows of Liquids Through Rotating Vortex Chambers", ASME Publications, Paper No. 73-WA/Flcs-8, 1973.

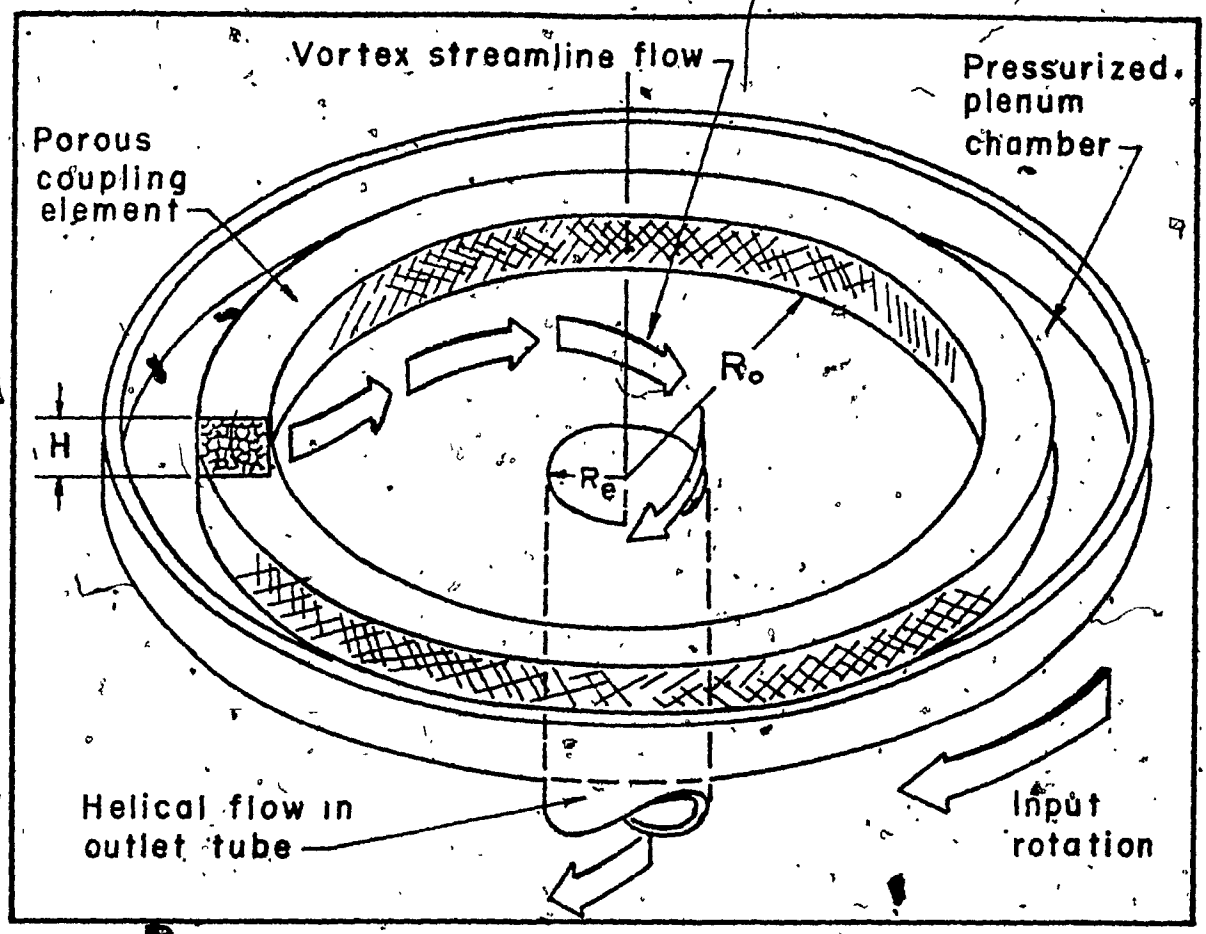

FIG. 1 VORTEX RATE SENSOR

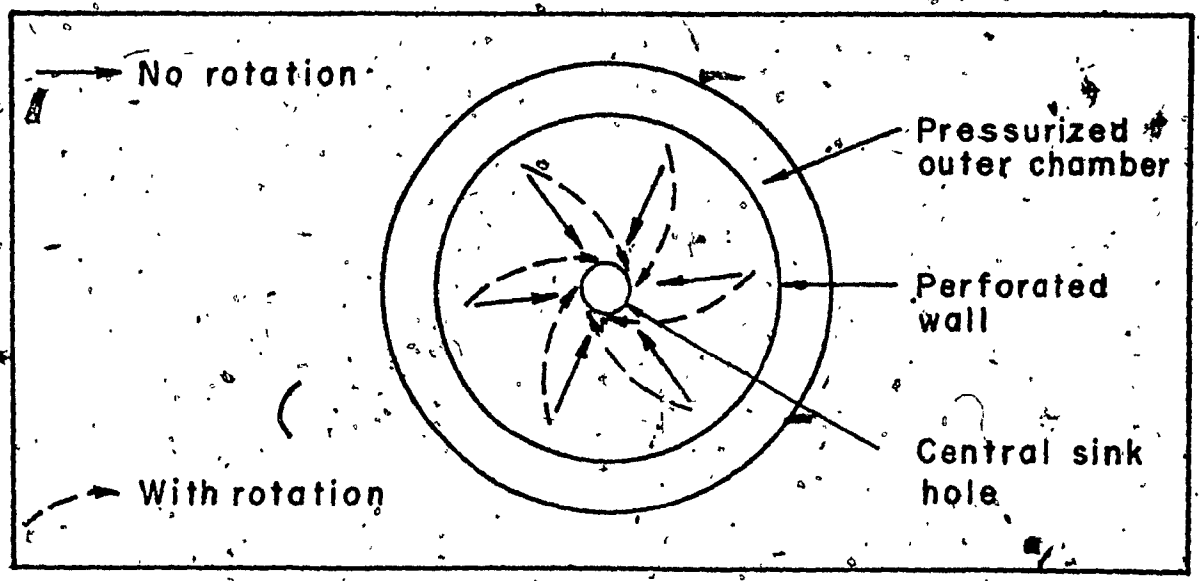

FIG. 2 OPERATION PRINCIPLE OF VORTEX RATE SENSOR

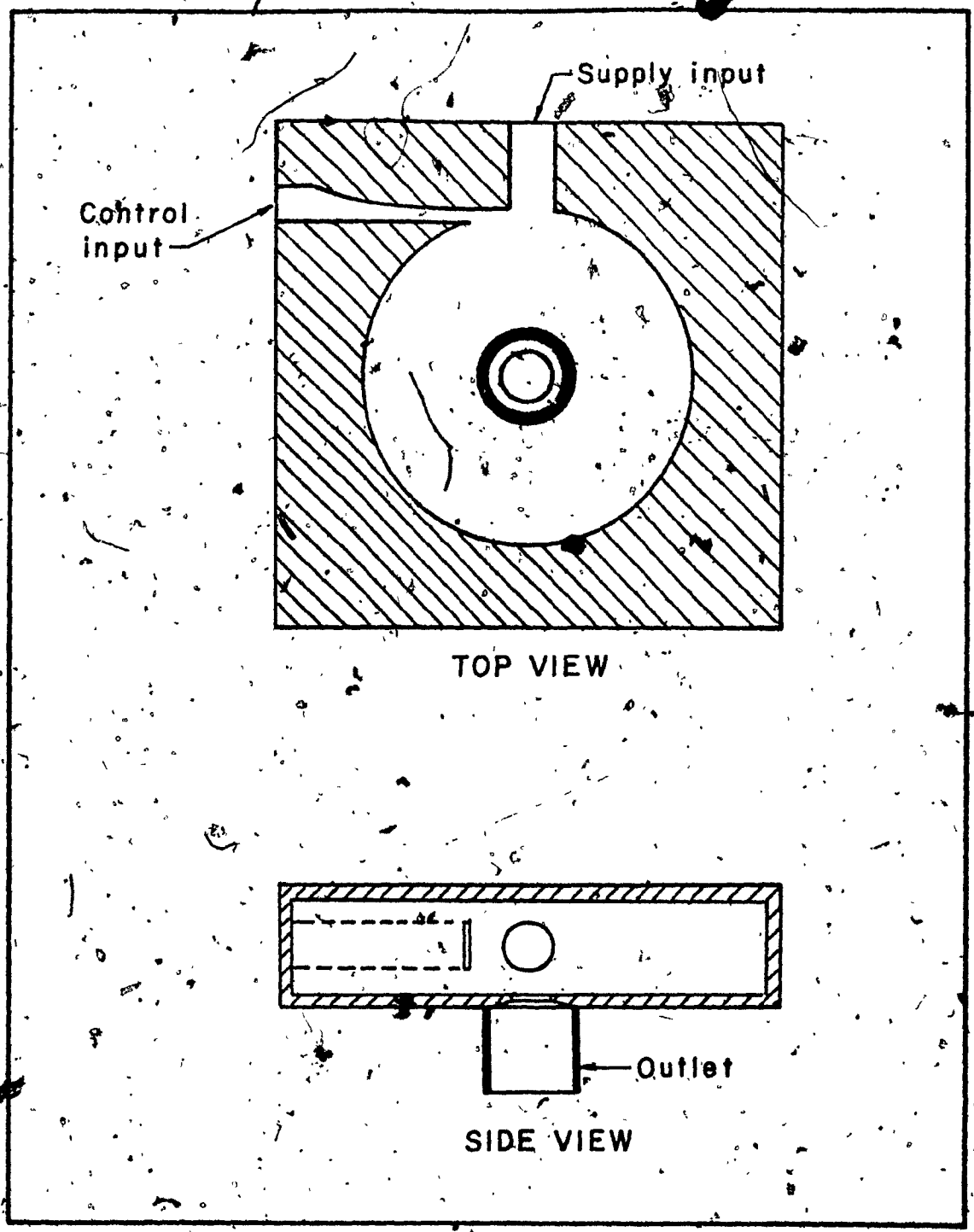

FIG. 3 SIMPLE TWO JET VORTEX AMPLIFIER

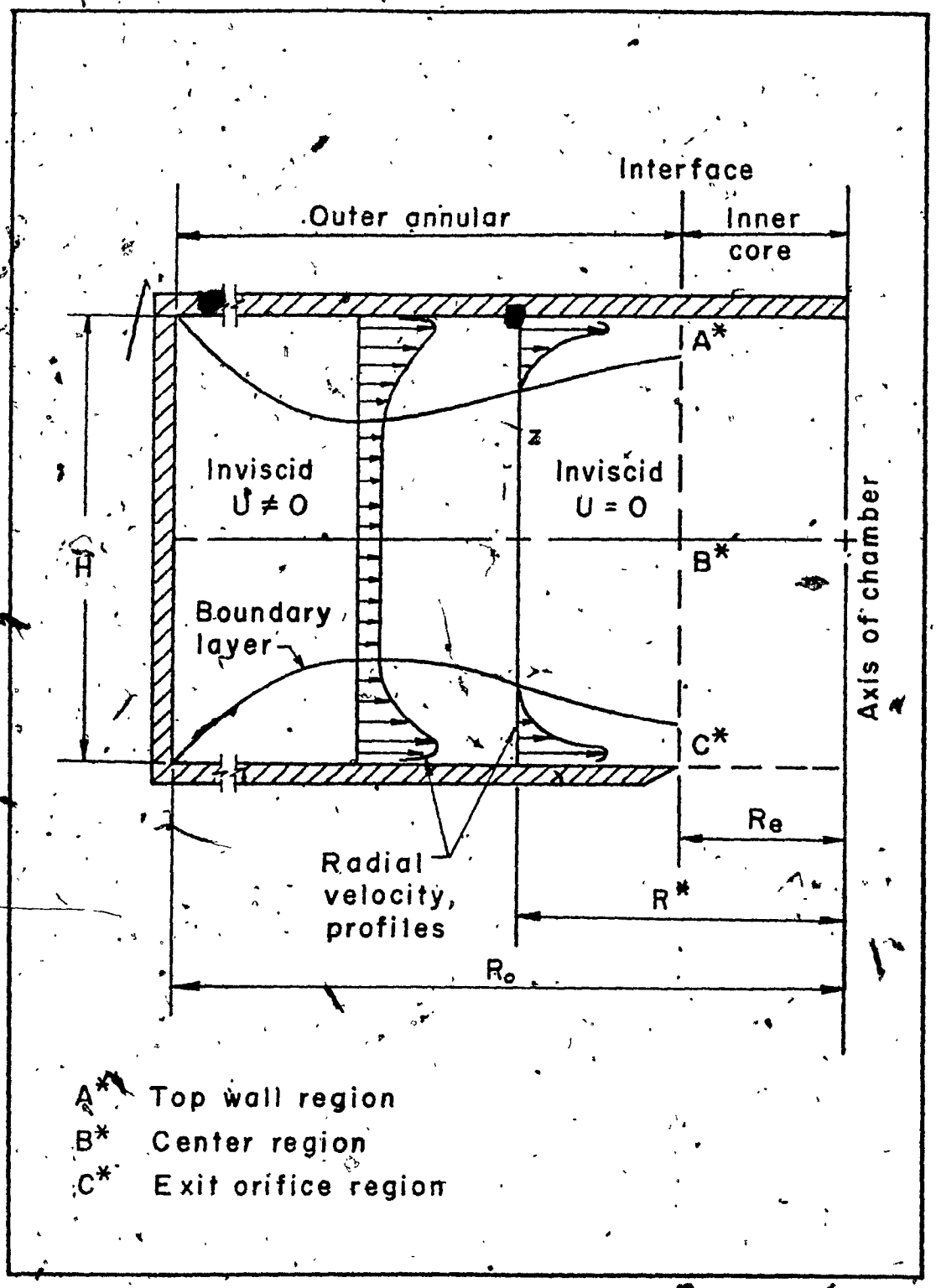

FIG. 4 ANALYTICAL MODEL OF THE VORTEX CHAMBER

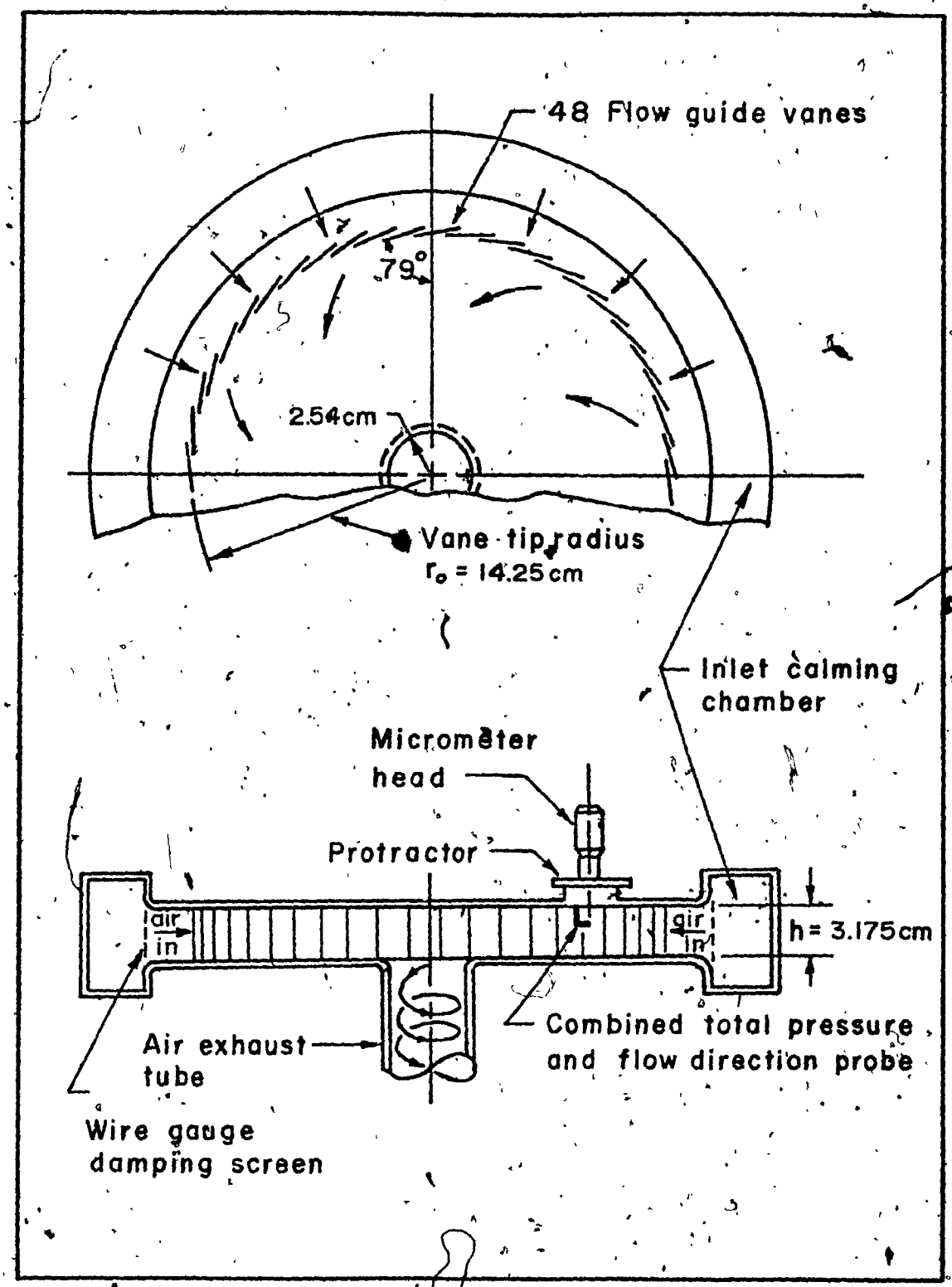

FIG. 5 EXPERIMENTAL VORTEX CHAMBER OF REF. 28

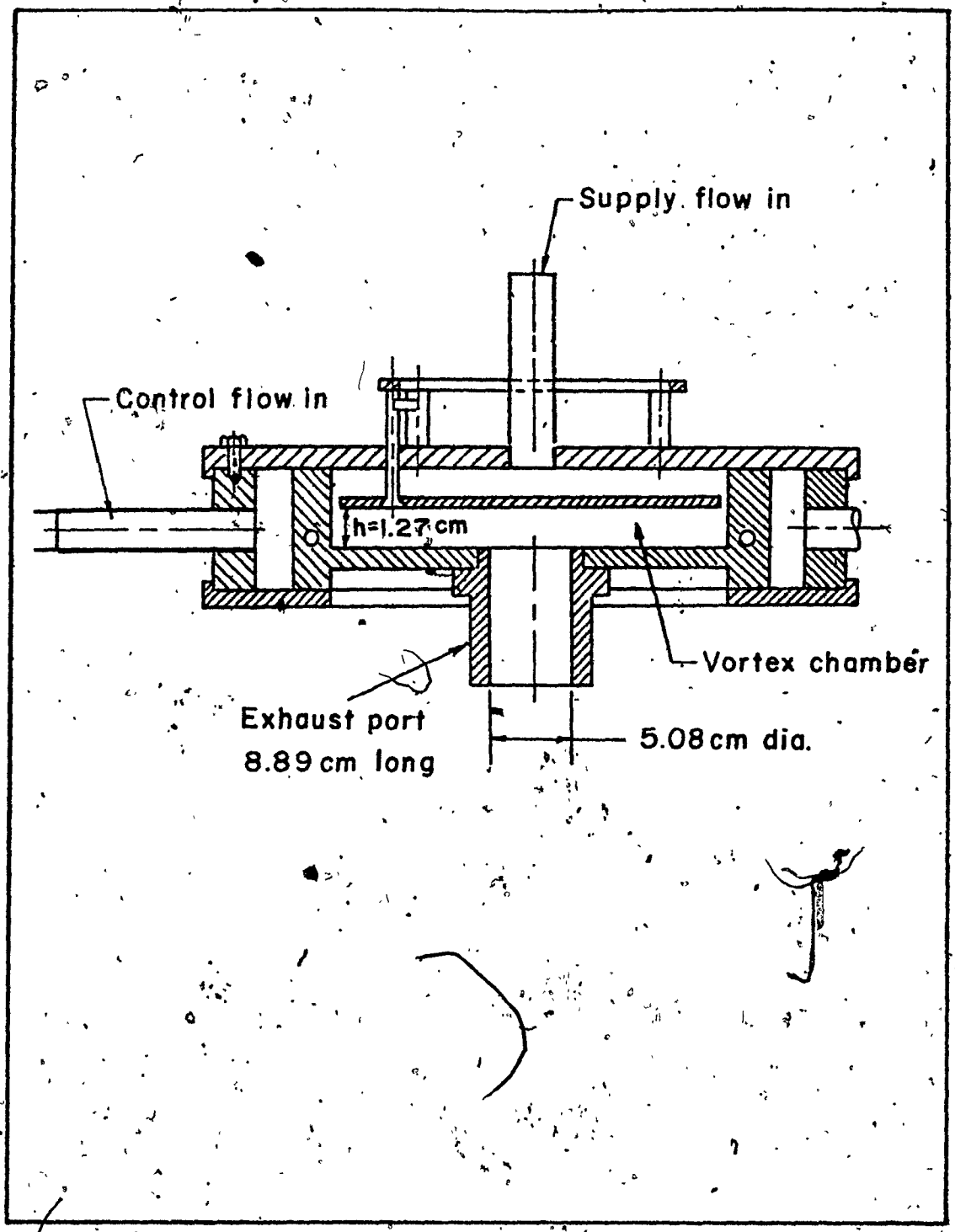

FIG. 6 EXPERIMENTAL VORTEX CHAMBER OF REF. 29

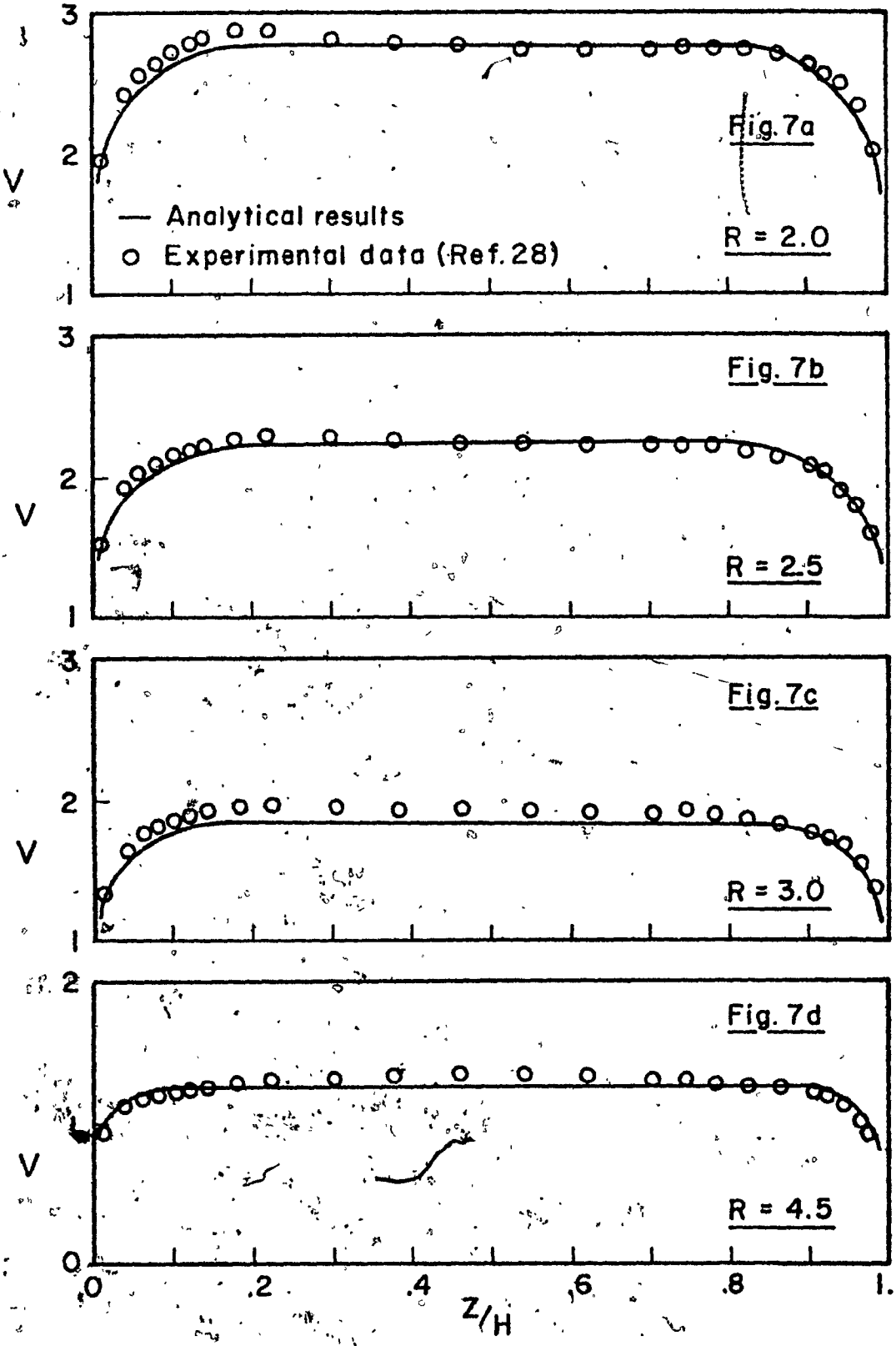

FIG. 7 COMPARISON OF EXPERIMENTAL AND ANALYTICAL TANGENTIAL VELOCITY DISTRIBUTIONS

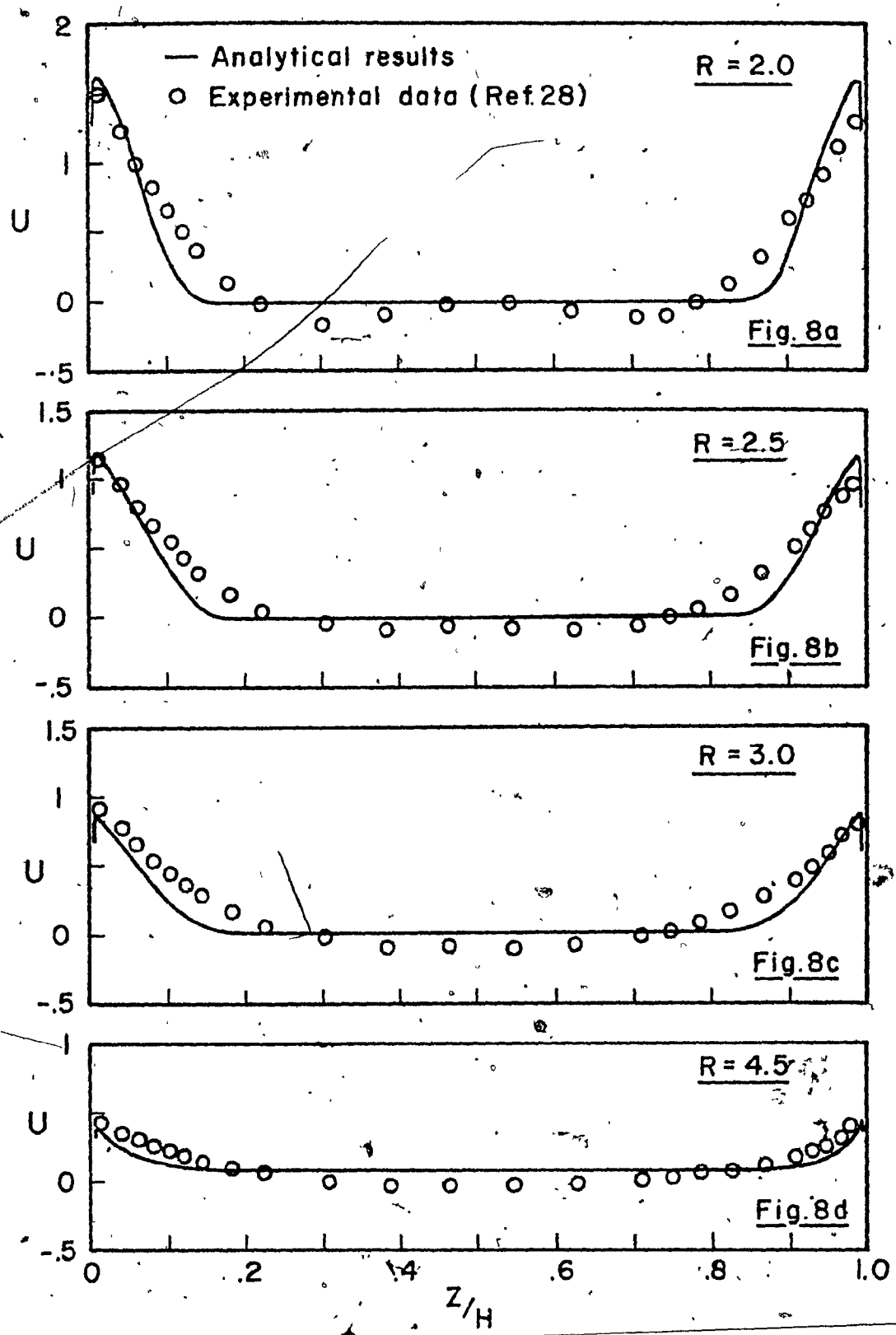

FIG. 8 COMPARISON OF EXPERIMENTAL AND ANALYTICAL RADIAL VELOCITY DISTRIBUTIONS

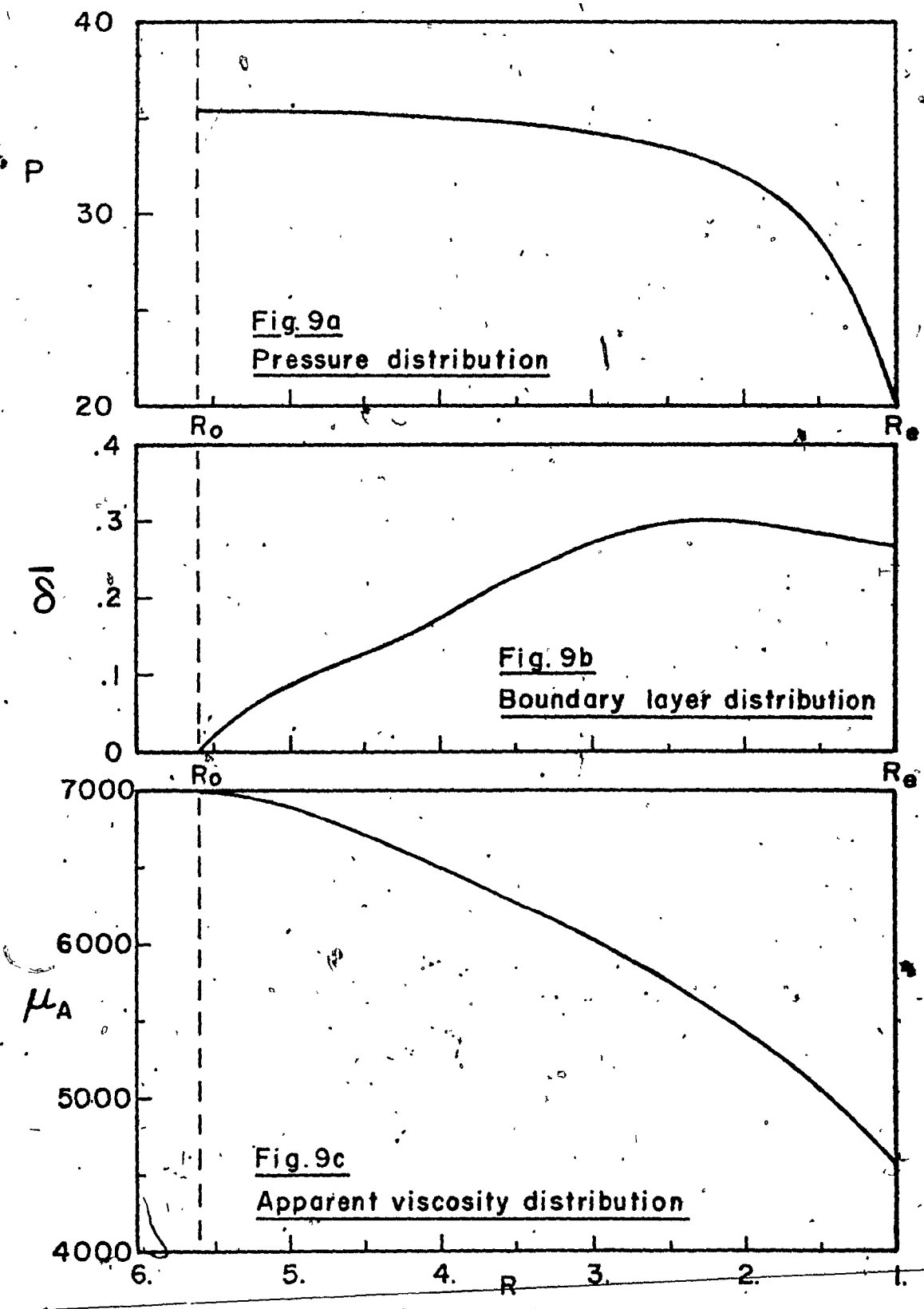

FIG. 9 ANALYTICAL FLOW PARAMETERS IN THE ANNULAR REGION OF REF. 28

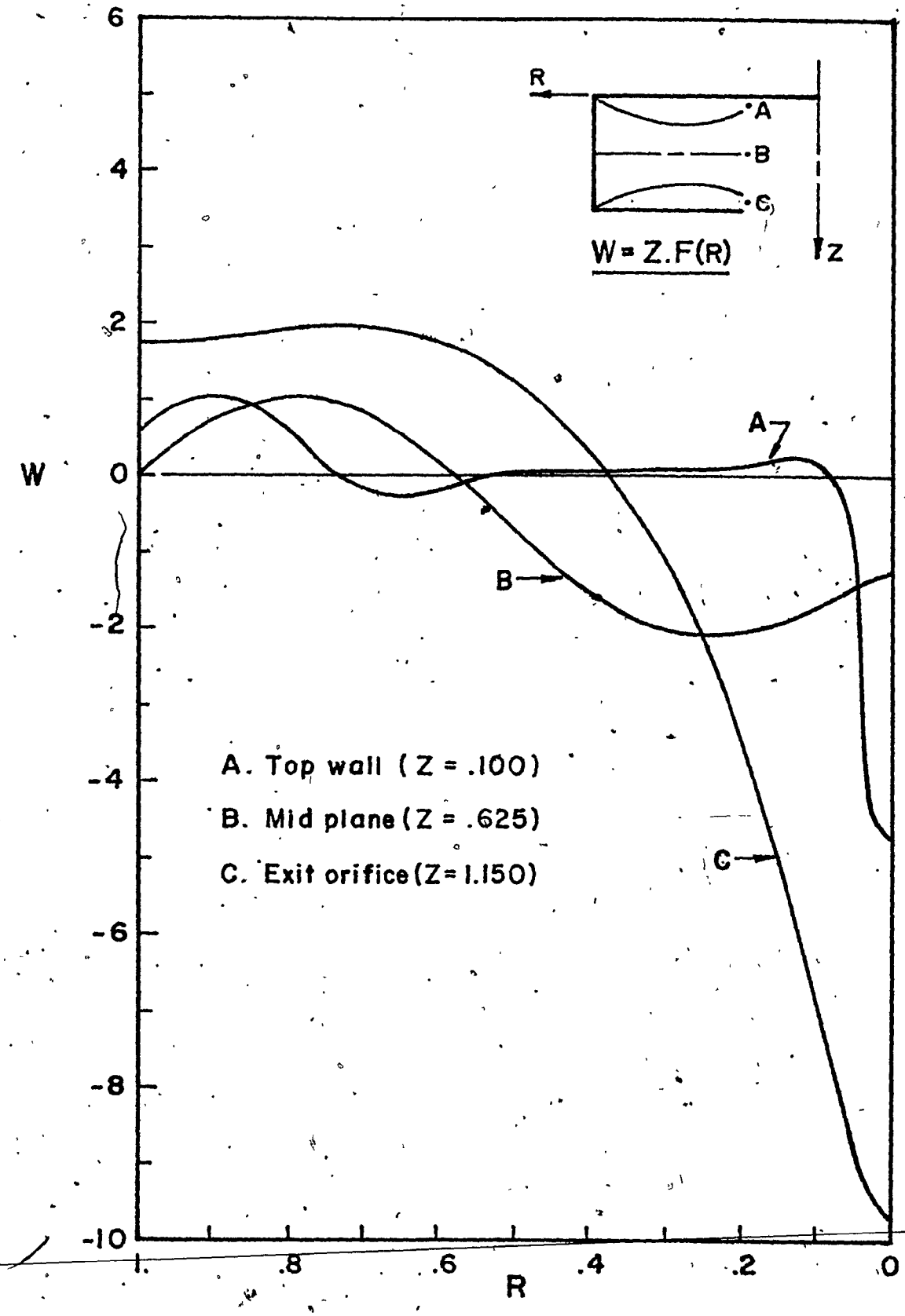

FIG. 10 AXIAL VELOCITY DISTRIBUTIONS IN THE CORE REGION — 2-CELL VORTEX

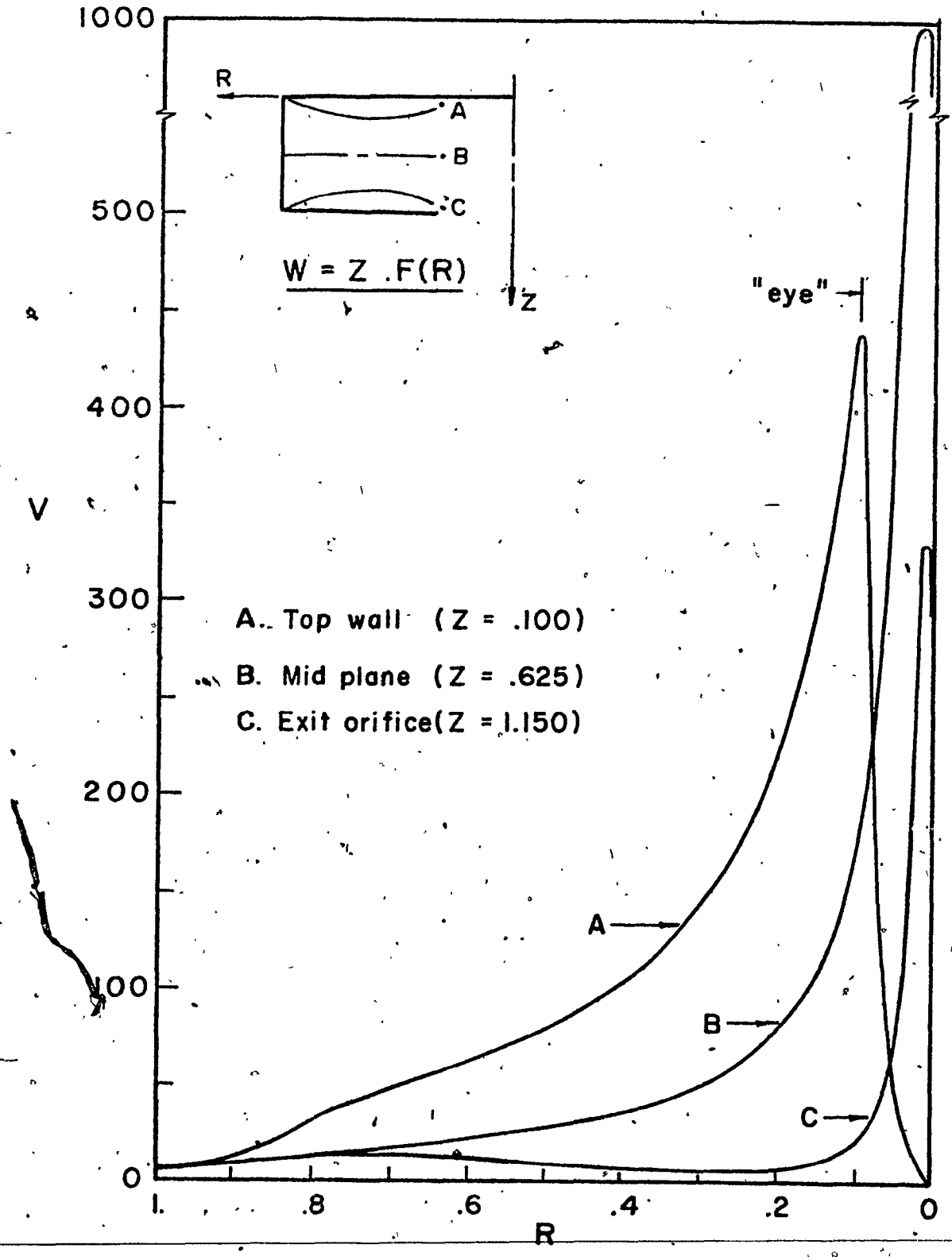

FIG. 11 TANGENTIAL VELOCITY DISTRIBUTIONS IN THE CORE REGION - 2-CELL VORTEX

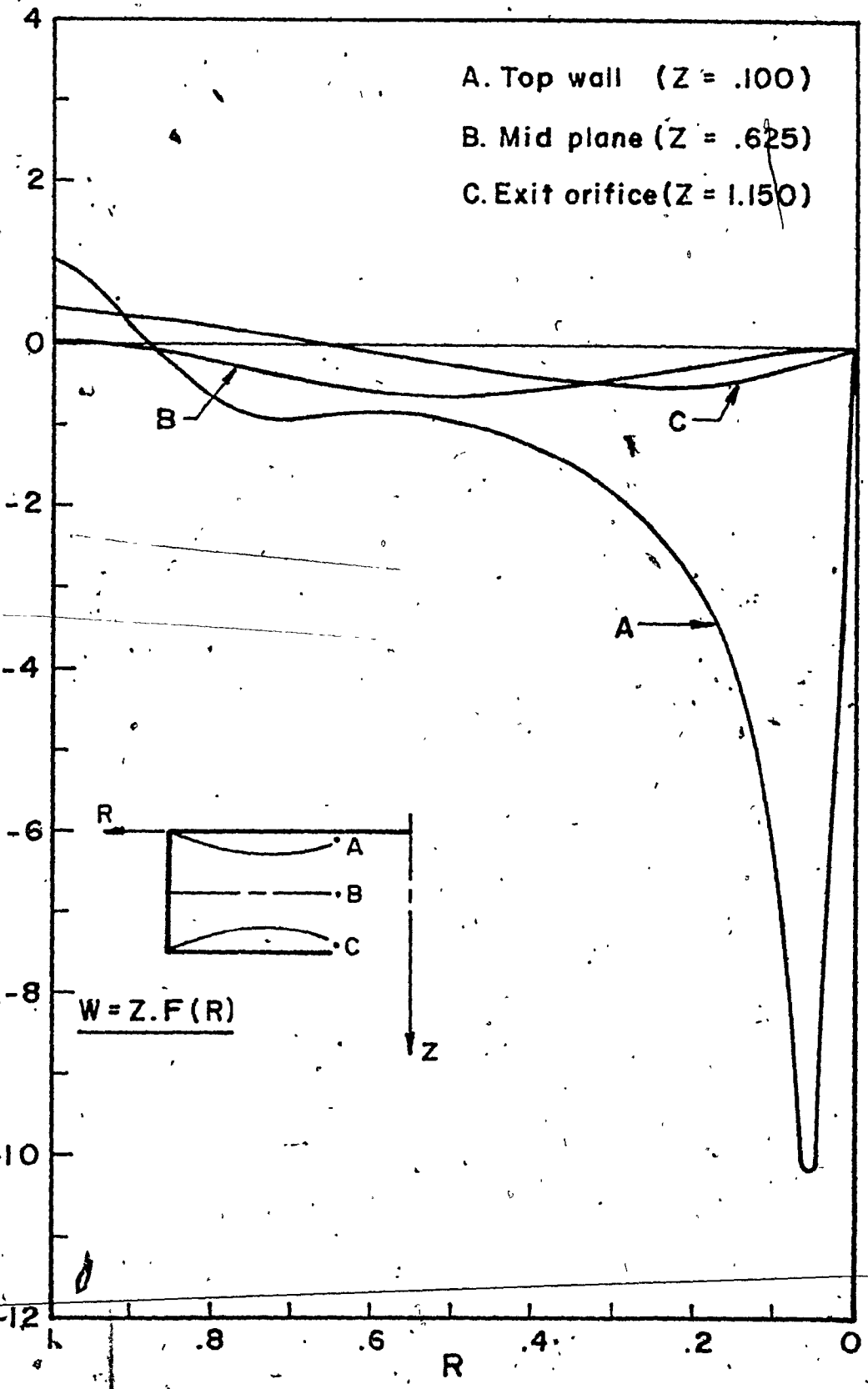

FIG. 2 RADIAL VELOCITY DISTRIBUTIONS IN THE CORE REGION — 2-CELL VORTEX

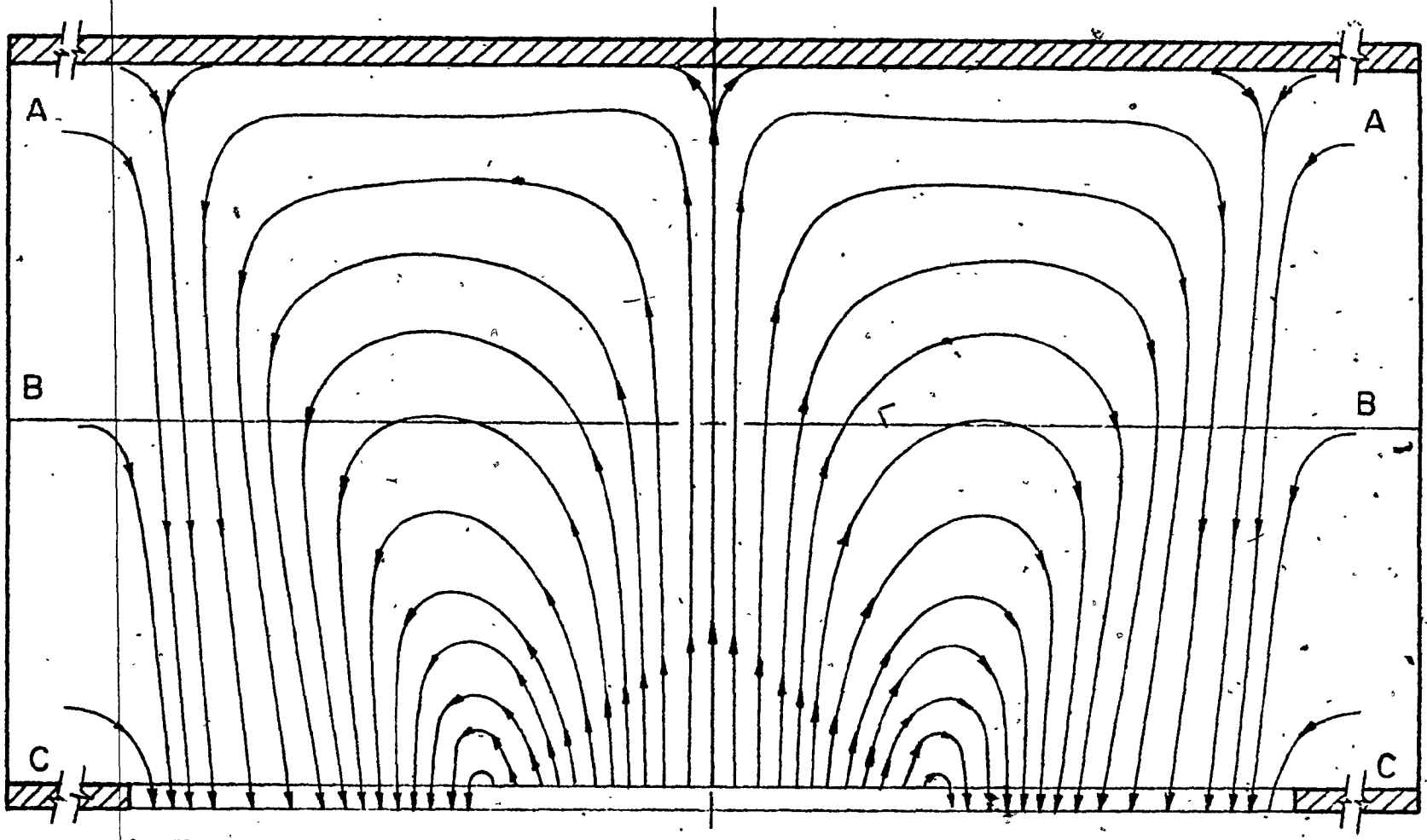

A. Top wall B. Mid plane C. Exit orifice $W = Z.F(R)$

FIG.13 STREAMLINES OF TWO-CELL CONFINED VORTEX FLOW

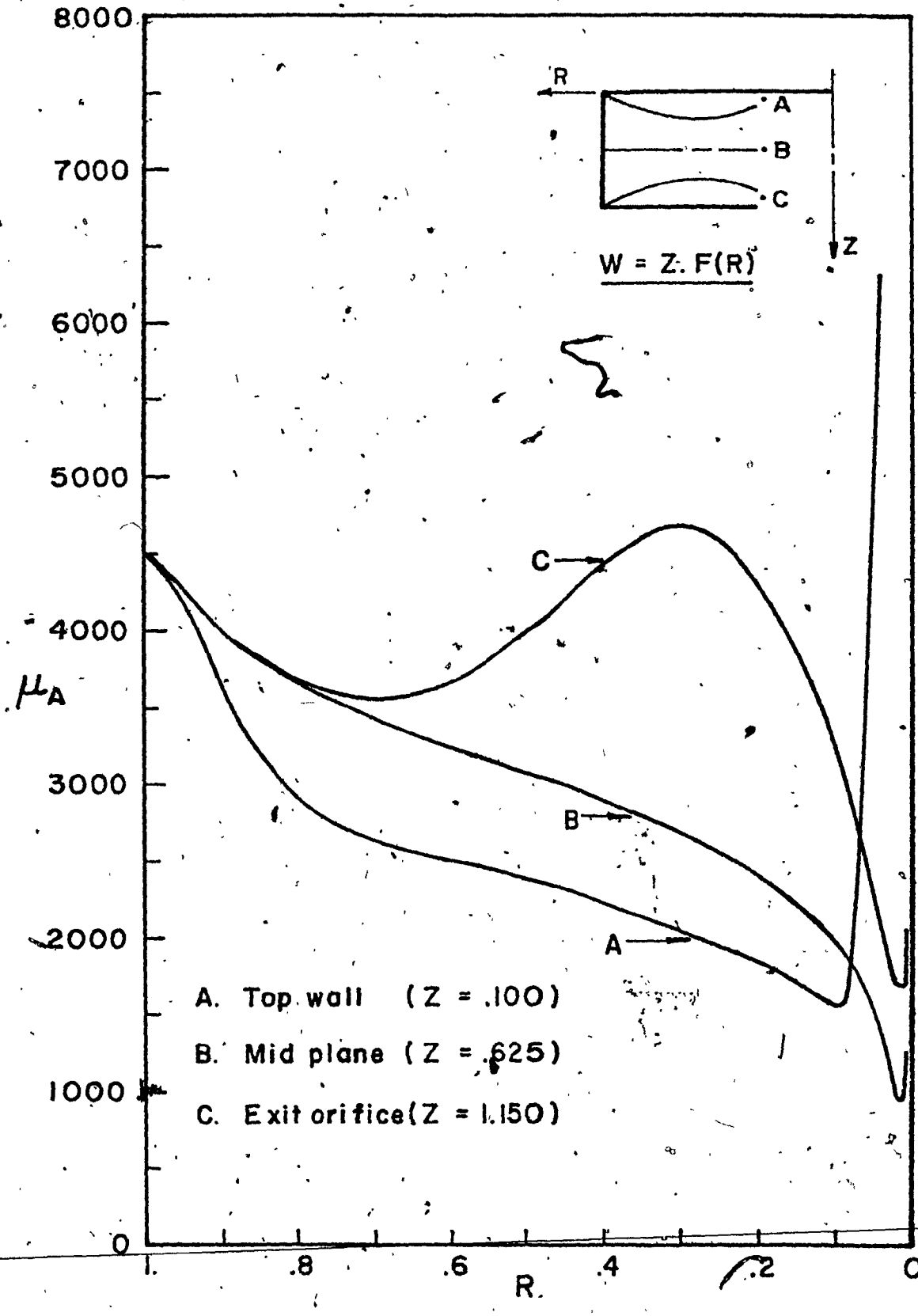

FIG. 14 APPARENT VISCOSITY DISTRIBUTIONS IN THE CORE REGION - TWO-CELL VORTEX

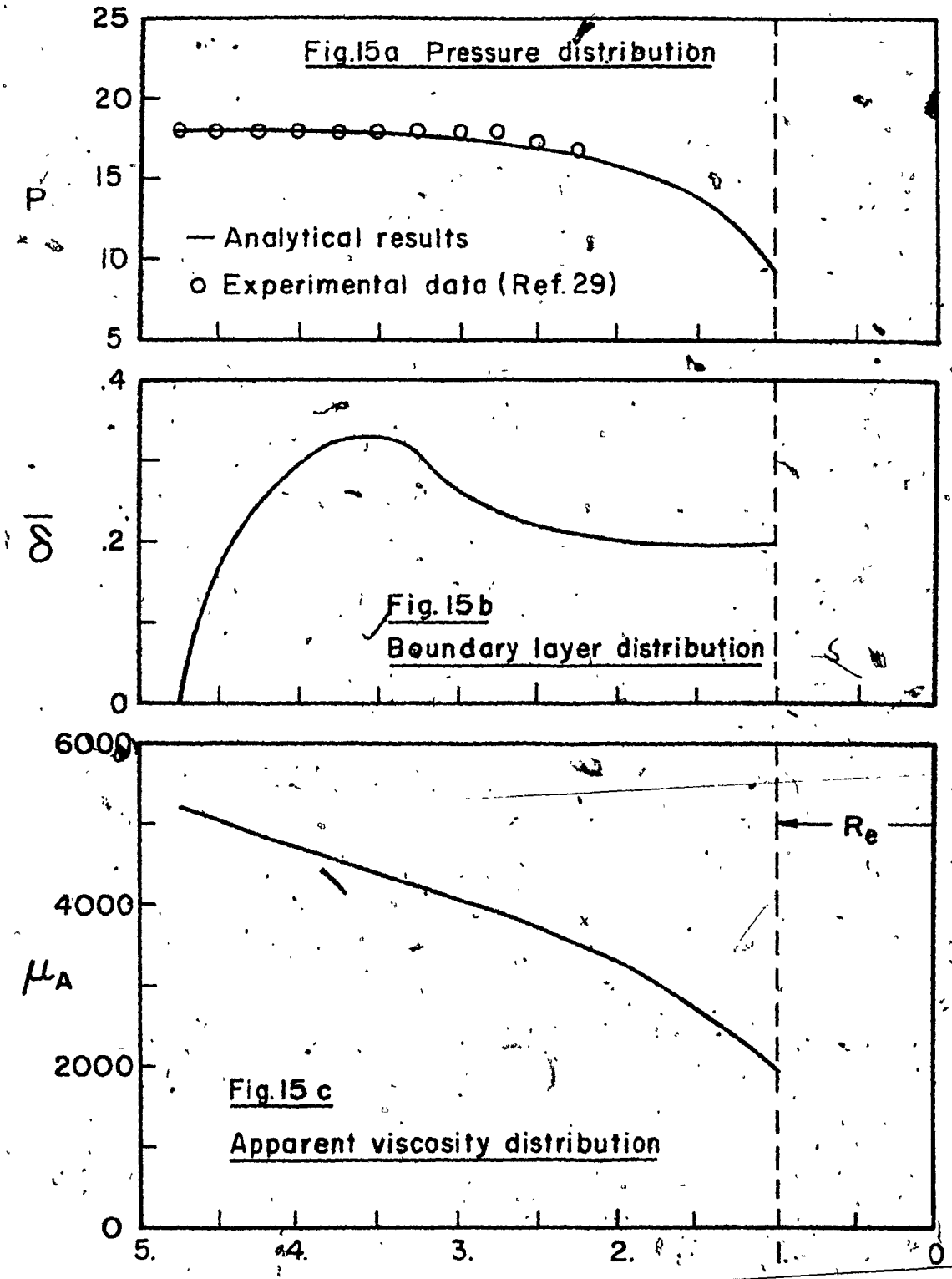

FIG. 15. ANALYTICAL FLOW PARAMETERS IN THE ANNULAR REGION OF REF. 29

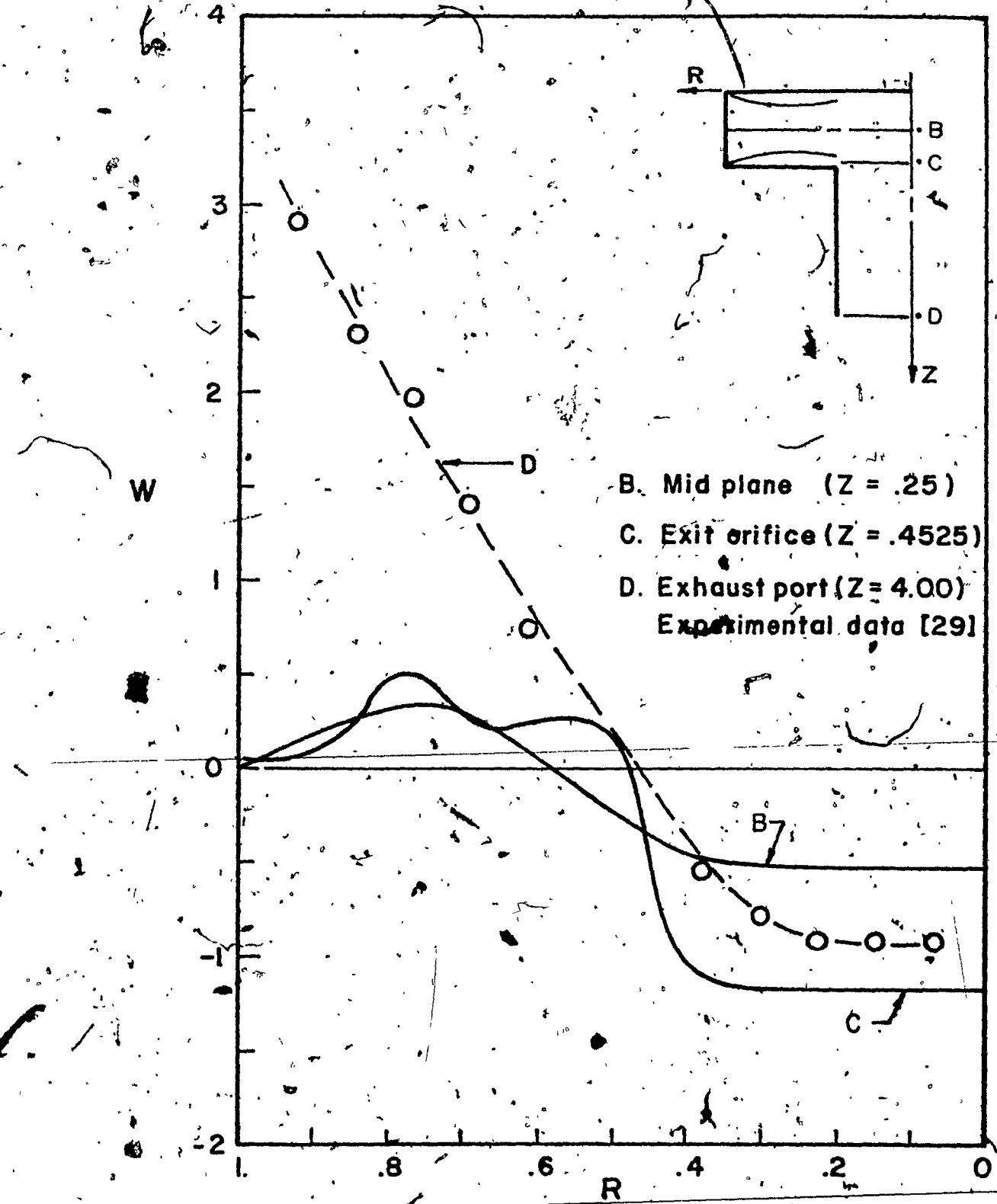

FIG. 16 AXIAL VELOCITY DISTRIBUTIONS IN THE CORE CYLINDER

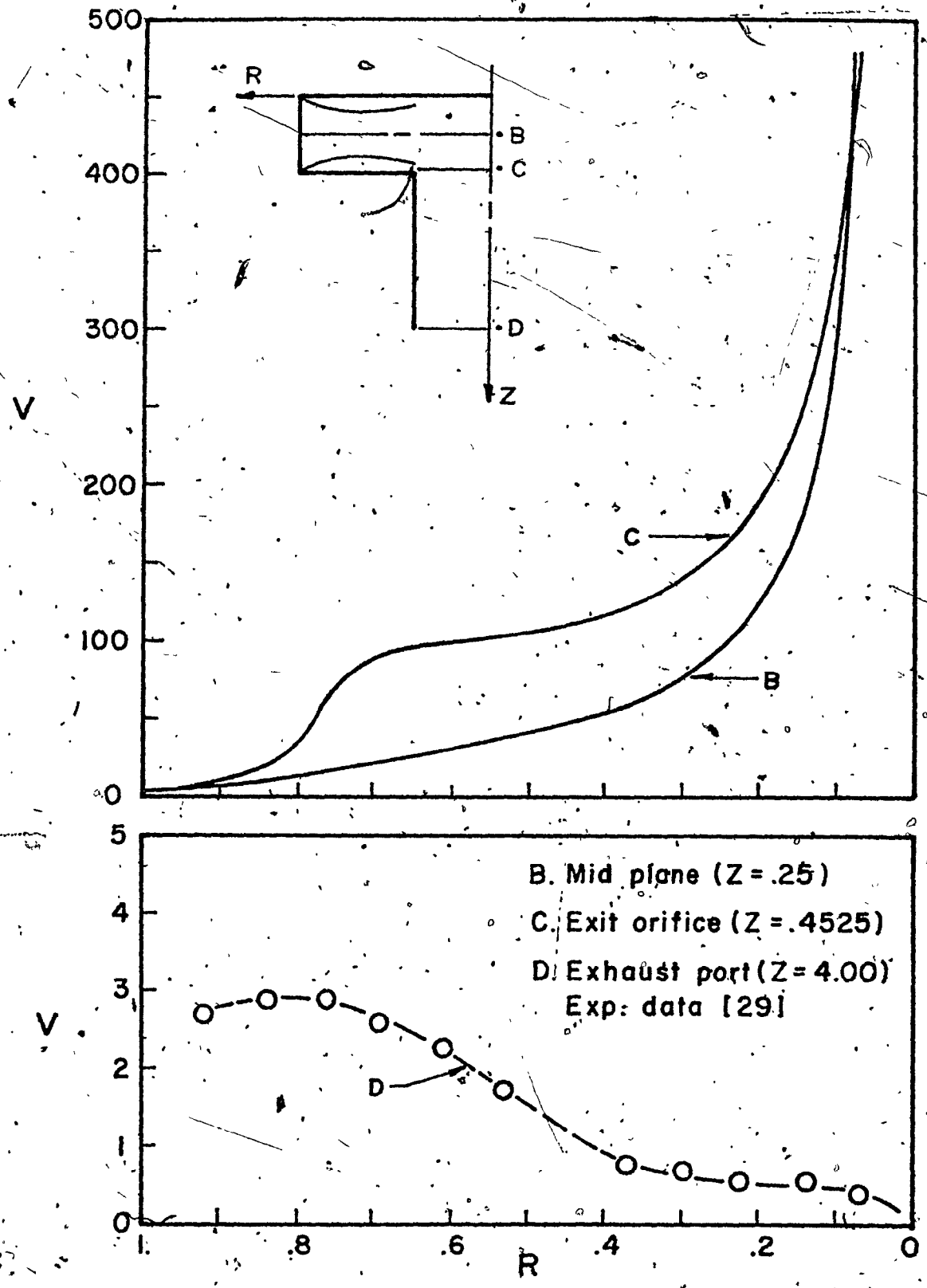

FIG. 17 TANGENTIAL VELOCITY DISTRIBUTIONS IN THE CORE CYLINDER

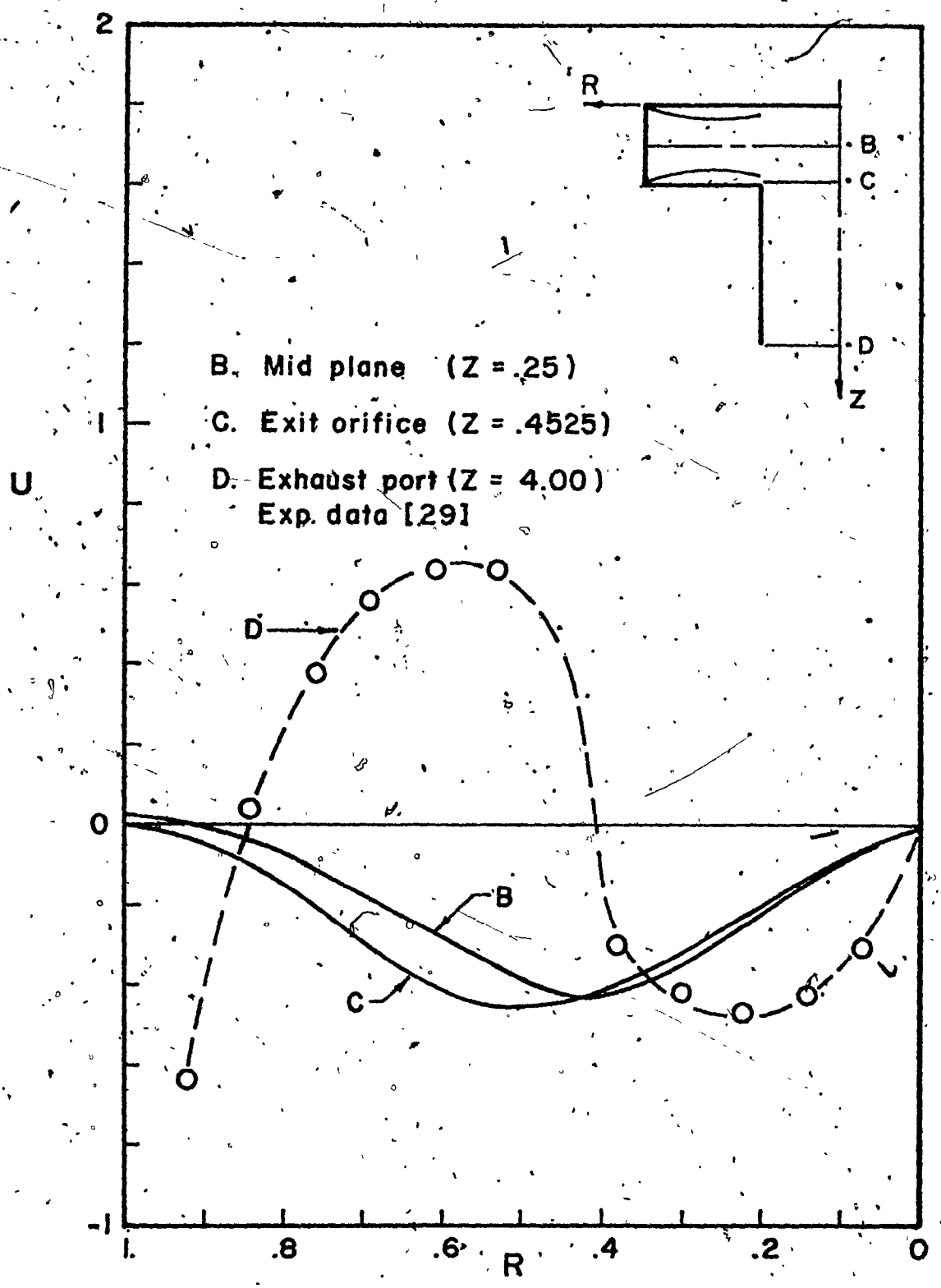

FIG. 18 RADIAL VELOCITY DISTRIBUTIONS IN THE CORE CYLINDER

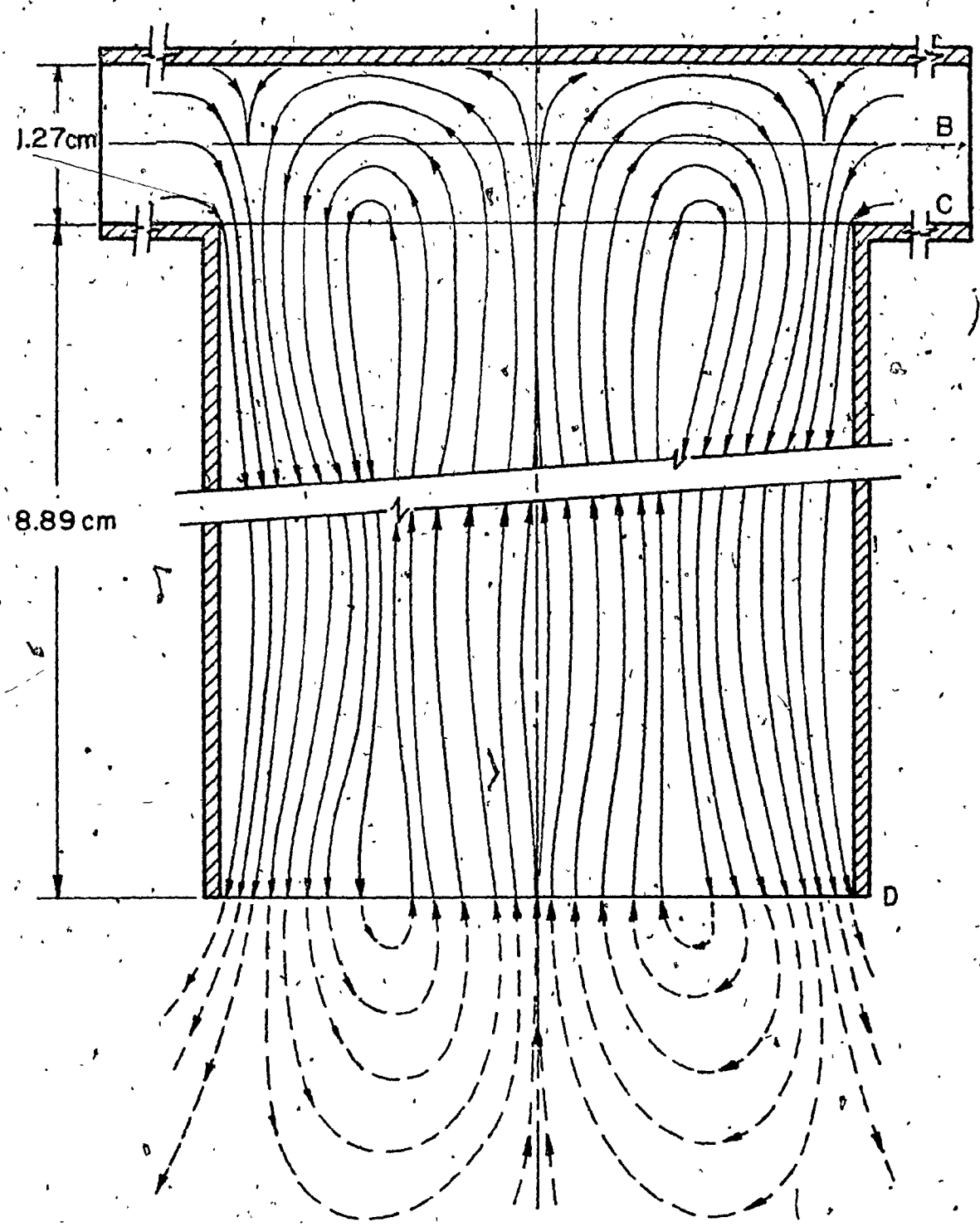

FIG.19 TWO-CELL VORTEX FLOW PATTERN IN THE CORE CYLINDER

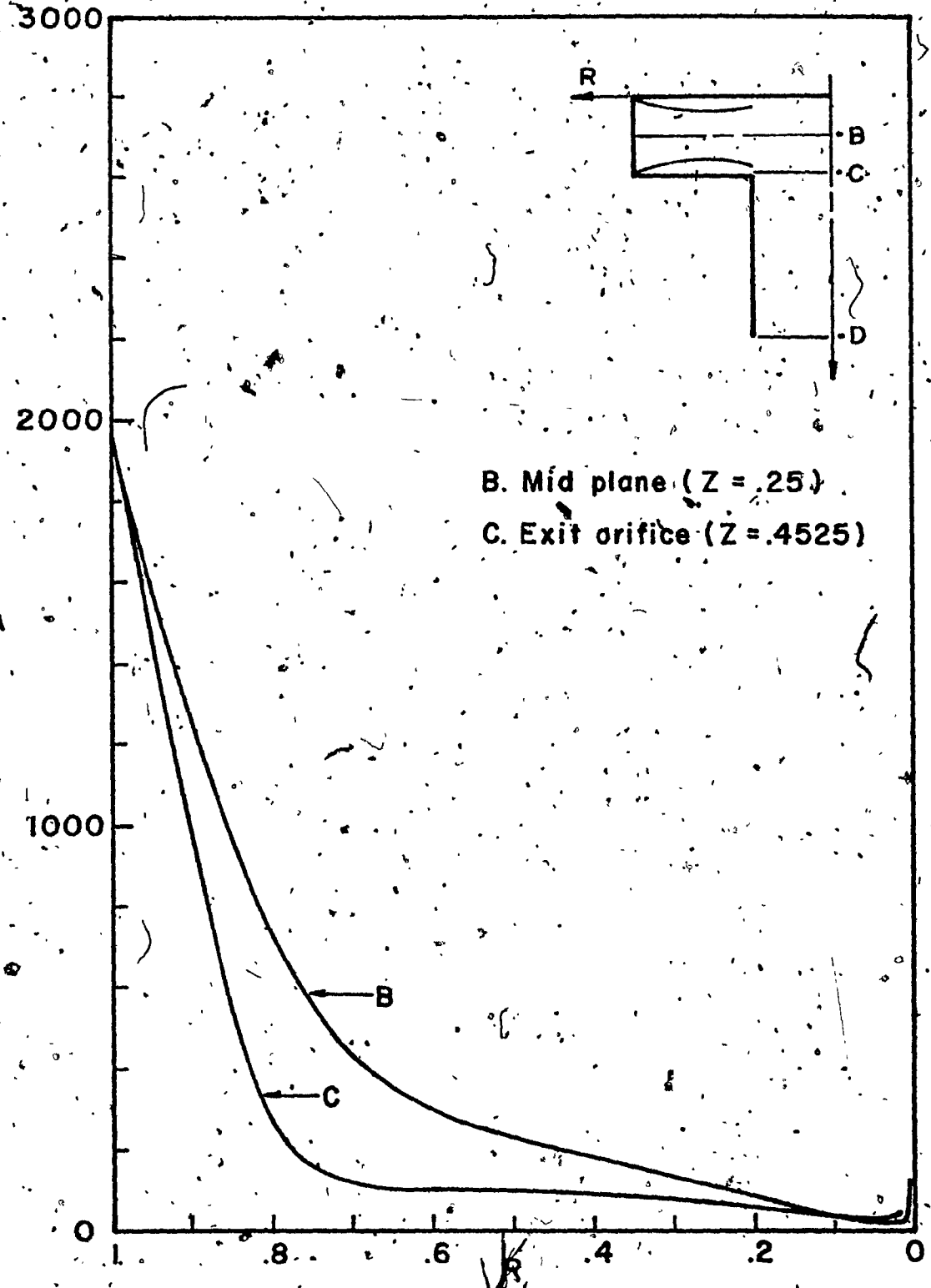

FIG. 20 THEORETICAL APPARENT VISCOSITY DISTRIBUTIONS IN THE CORE REGION

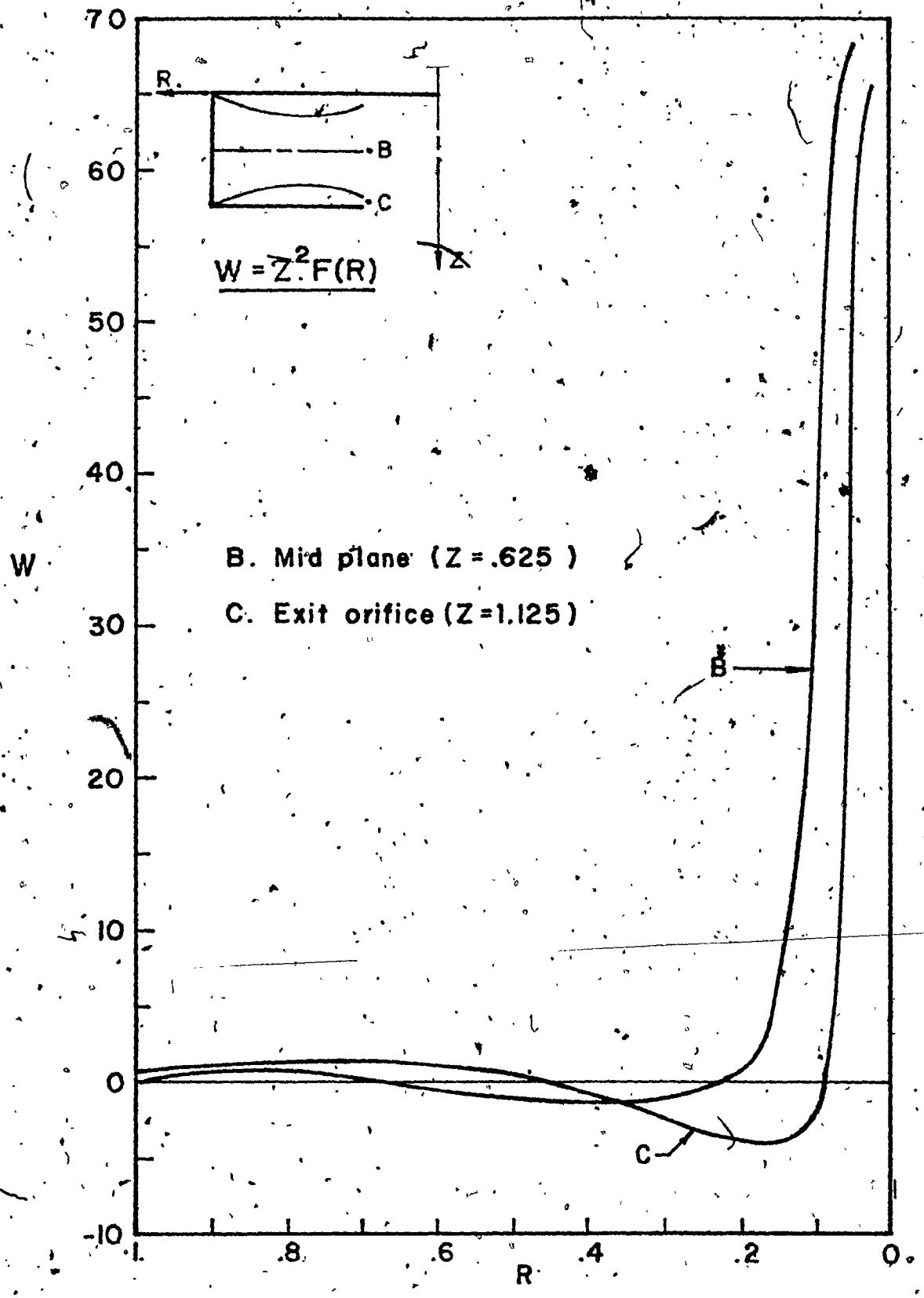

FIG. 21 AXIAL VELOCITY DISTRIBUTIONS IN THE CORE REGION - 4-CELL VORTEX

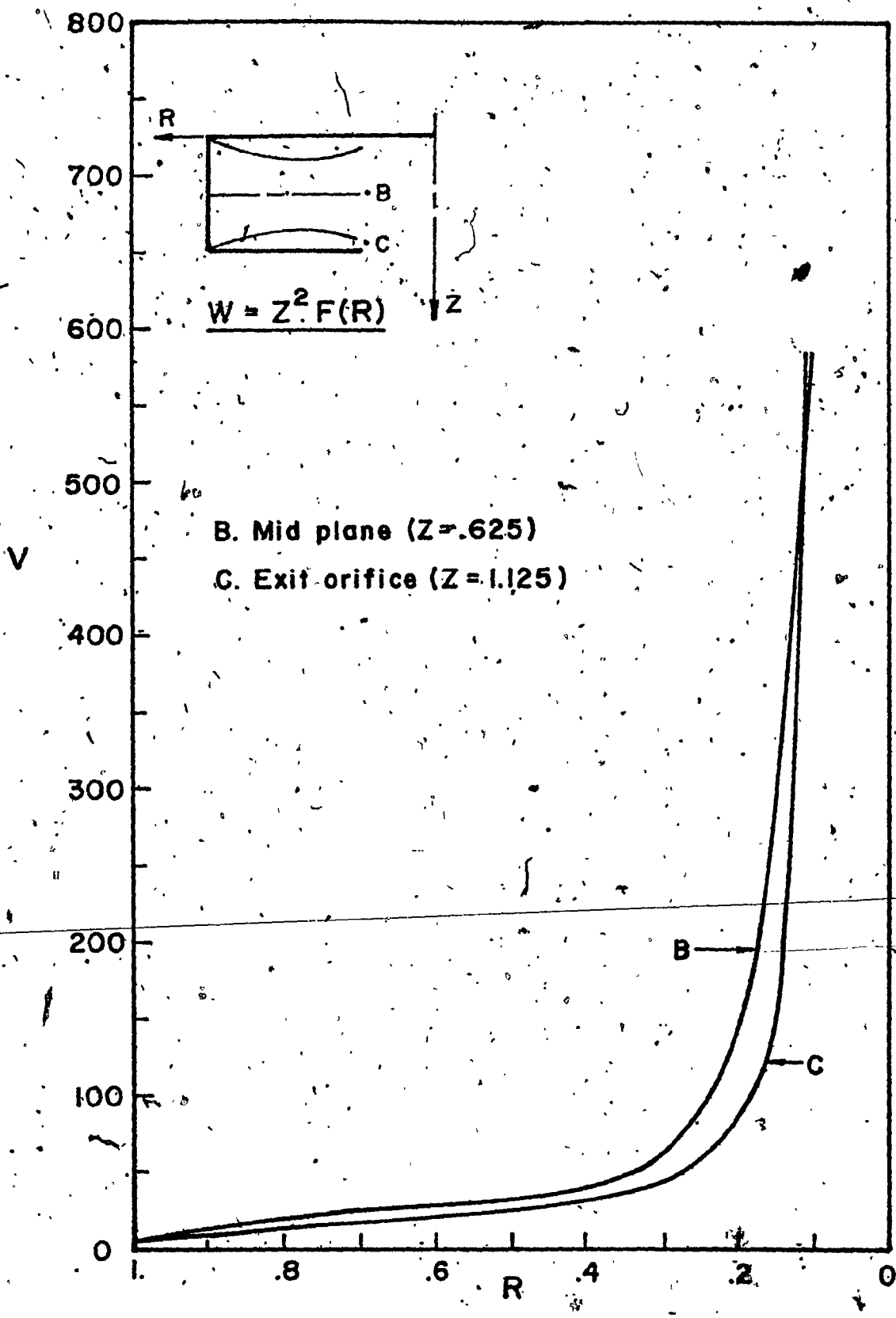

FIG. 22 TANGENTIAL VELOCITY DISTRIBUTIONS IN THE CORE REGION – 4-CELL VORTEX

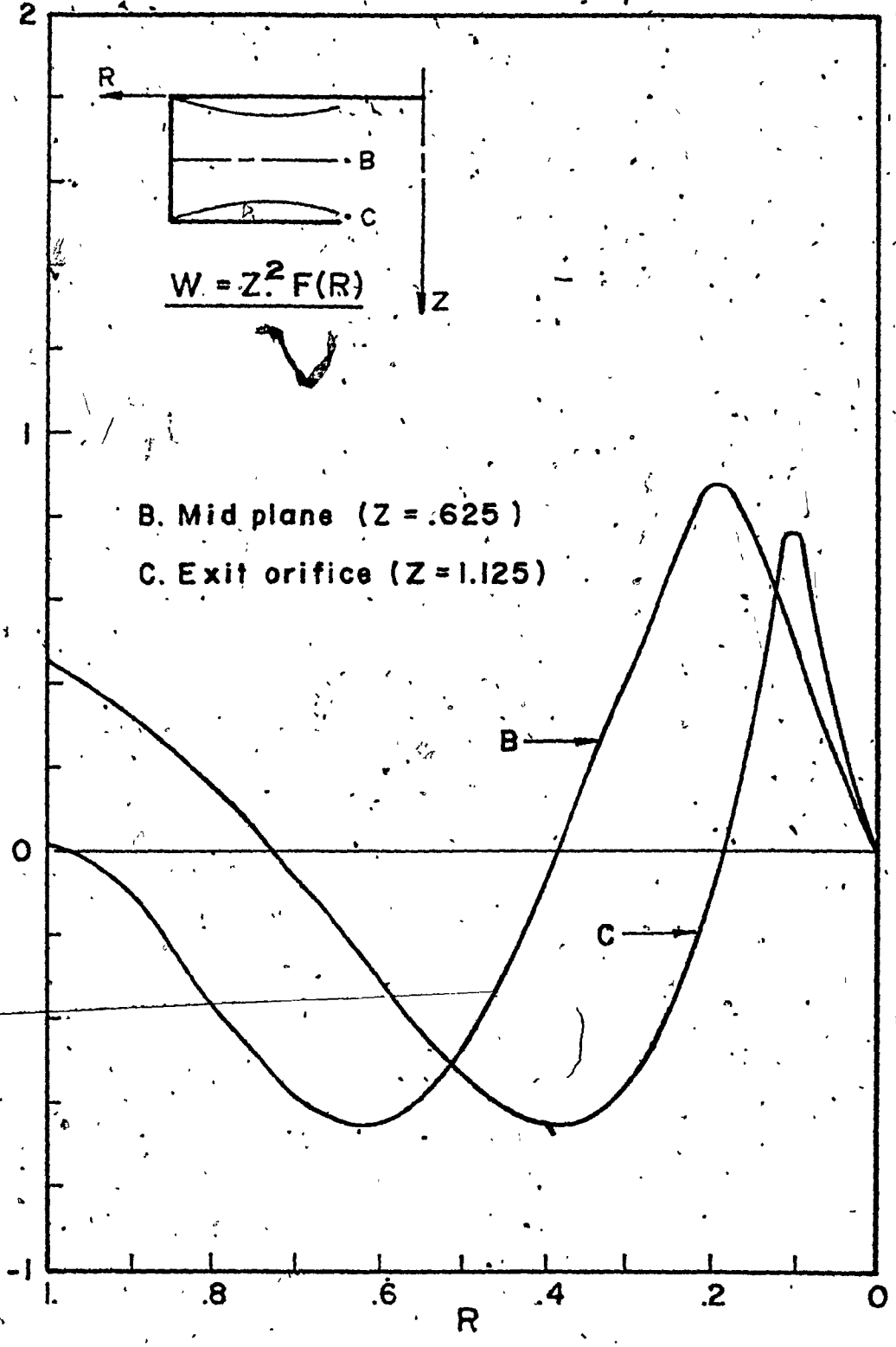

FIG.23 RADIAL VELOCITY DISTRIBUTIONS IN THE CORE REGION — 4-CELL VORTEX

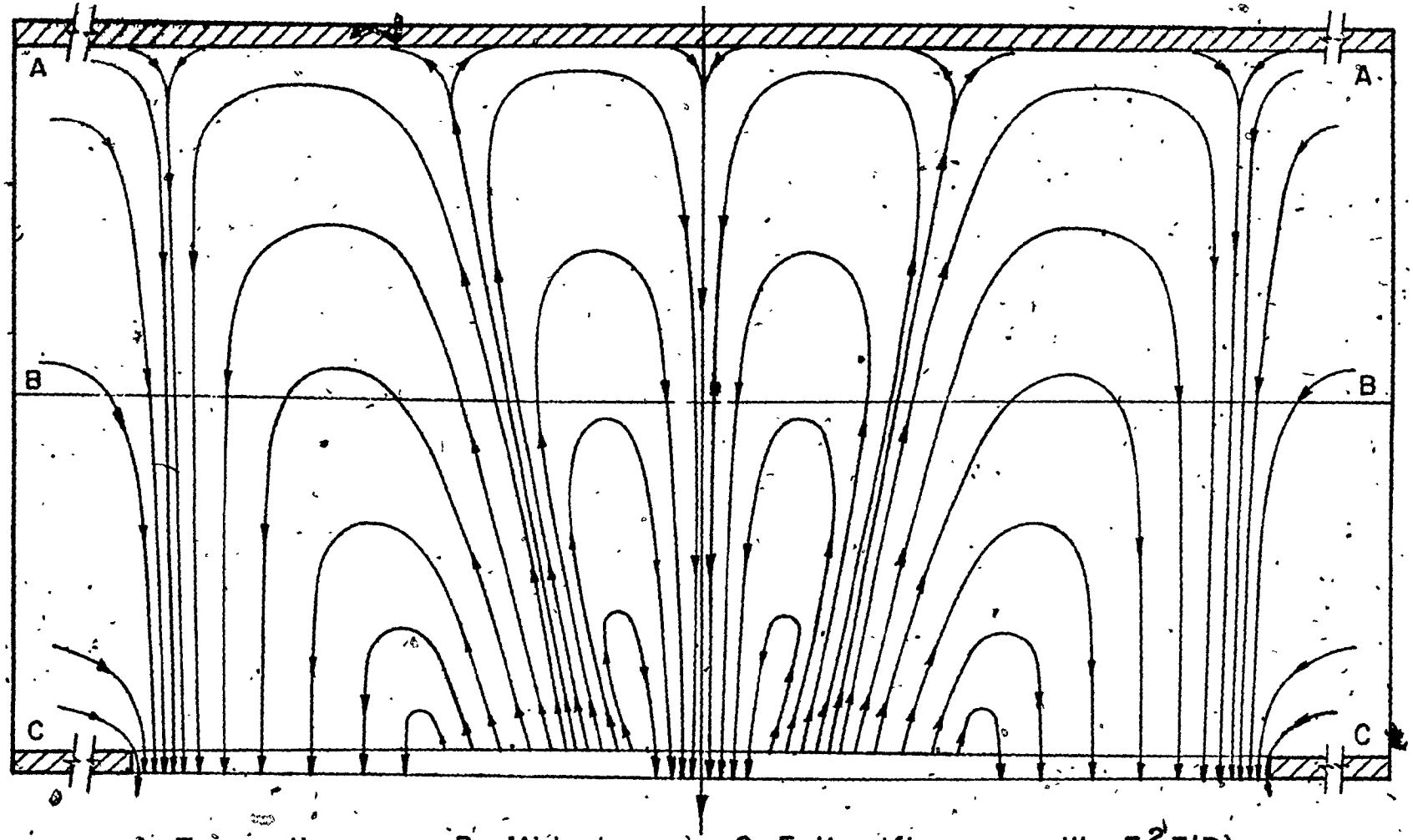

A. Top wall B. Mid plane C. Exit orifice $W = Z^2 F(R)$

FIG.24 STREAMLINES OF FOUR-CELL CONFINED VORTEX FLOW

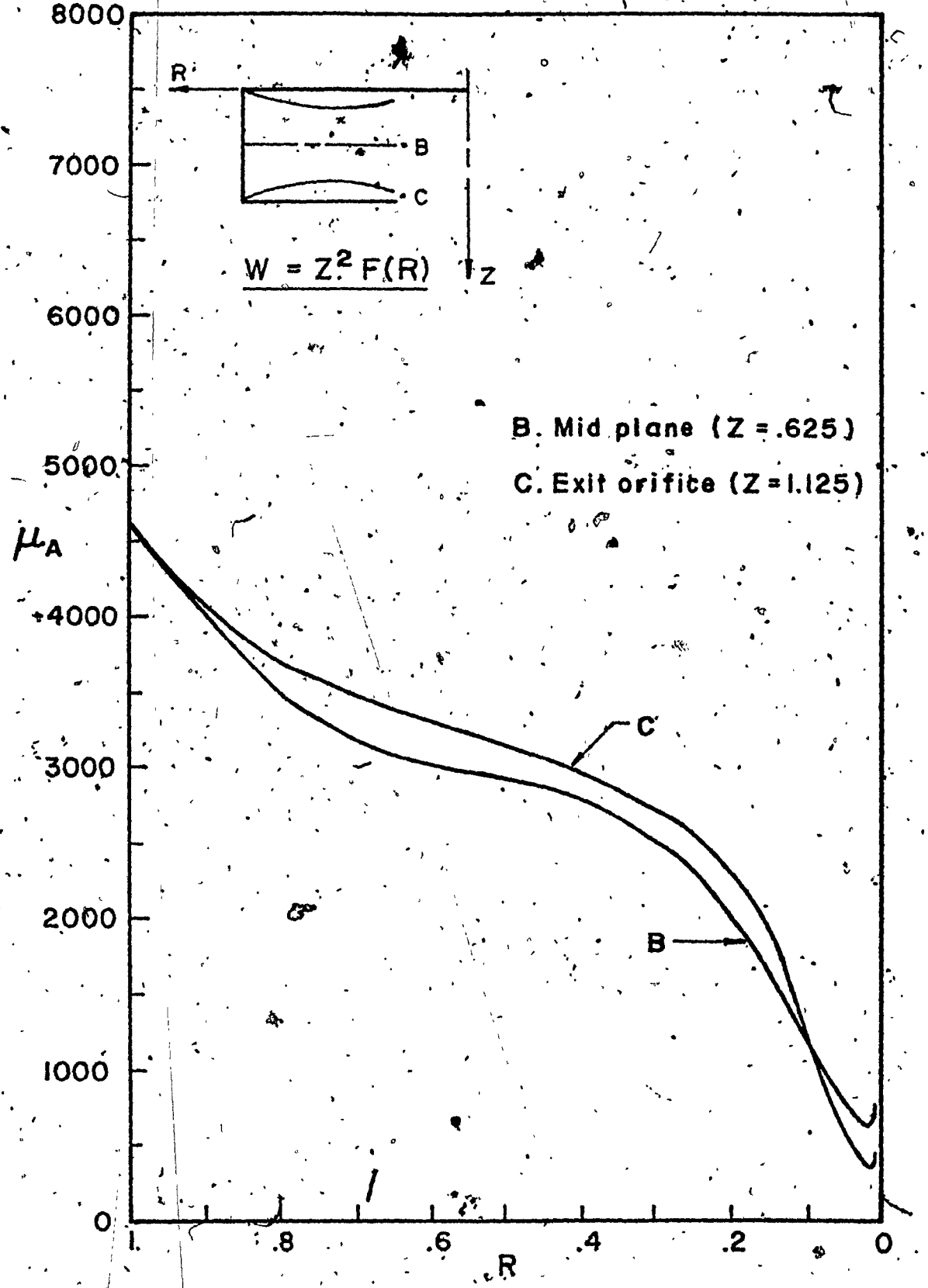

FIG. 25 THEORETICAL APPARENT VISCOSITY DISTRIBUTIONS IN THE CORE REGION -4-CELL VORTEX

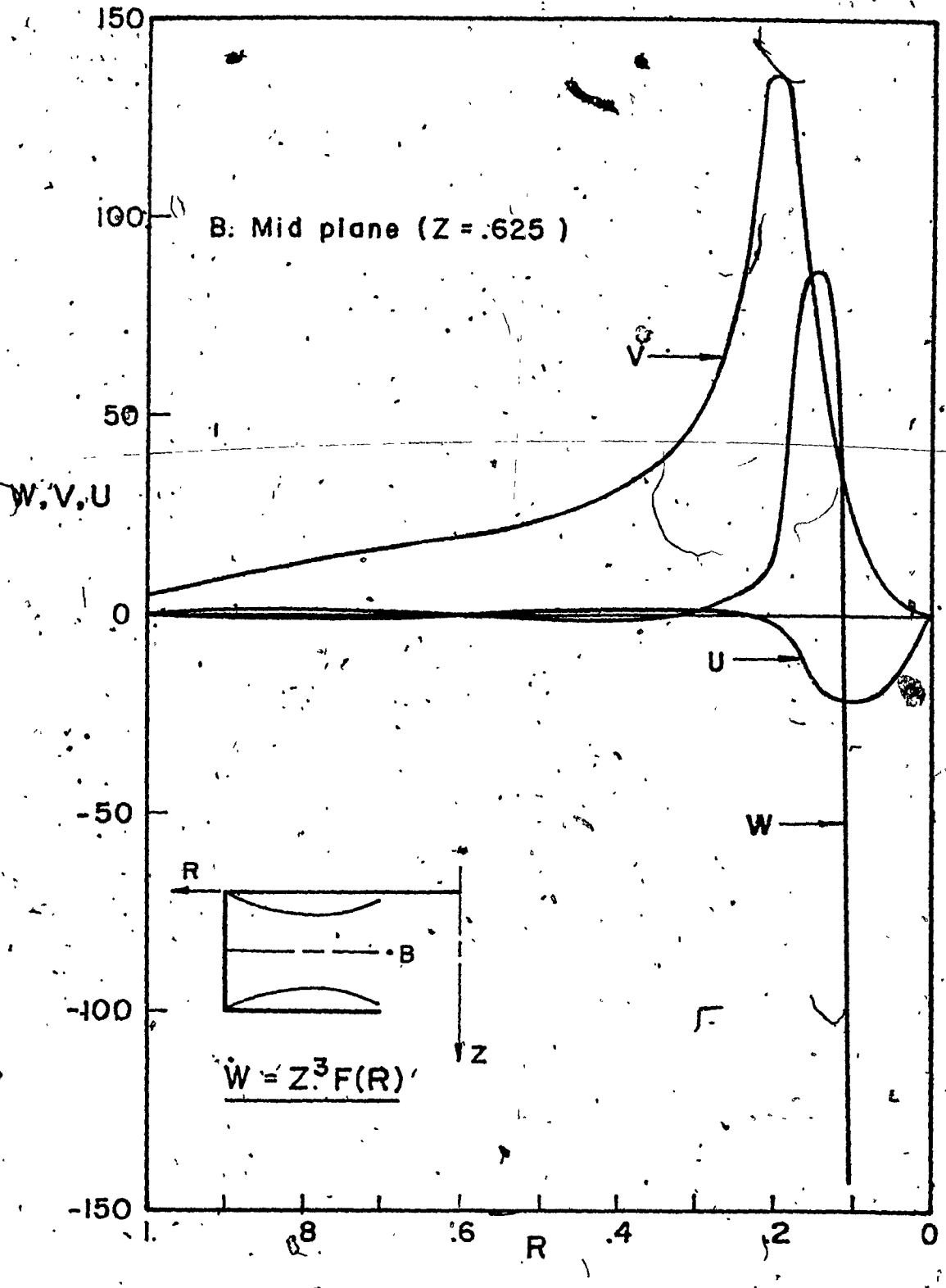

FIG. 26 AXIAL, TANGENTIAL AND RADIAL VELOCITY DISTRIBUTIONS IN THE CORE REGION — 6-CELL VORTEX

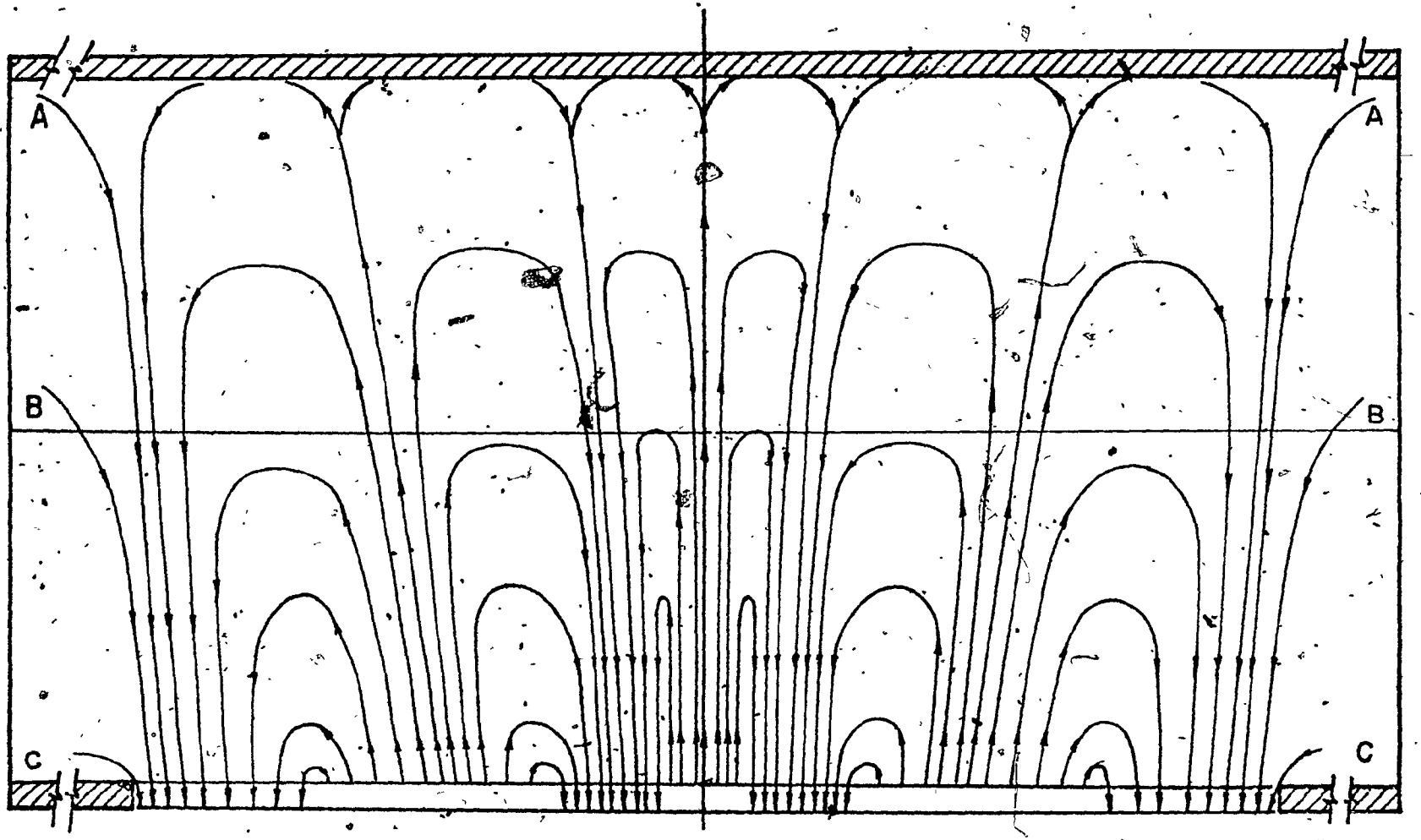

A. Top wall B. Mid plane C. Exit orifice $W = Z^3 F(R)$

FIG.27 STREAMLINES OF SIX-CELL CONFINED VORTEX FLOW

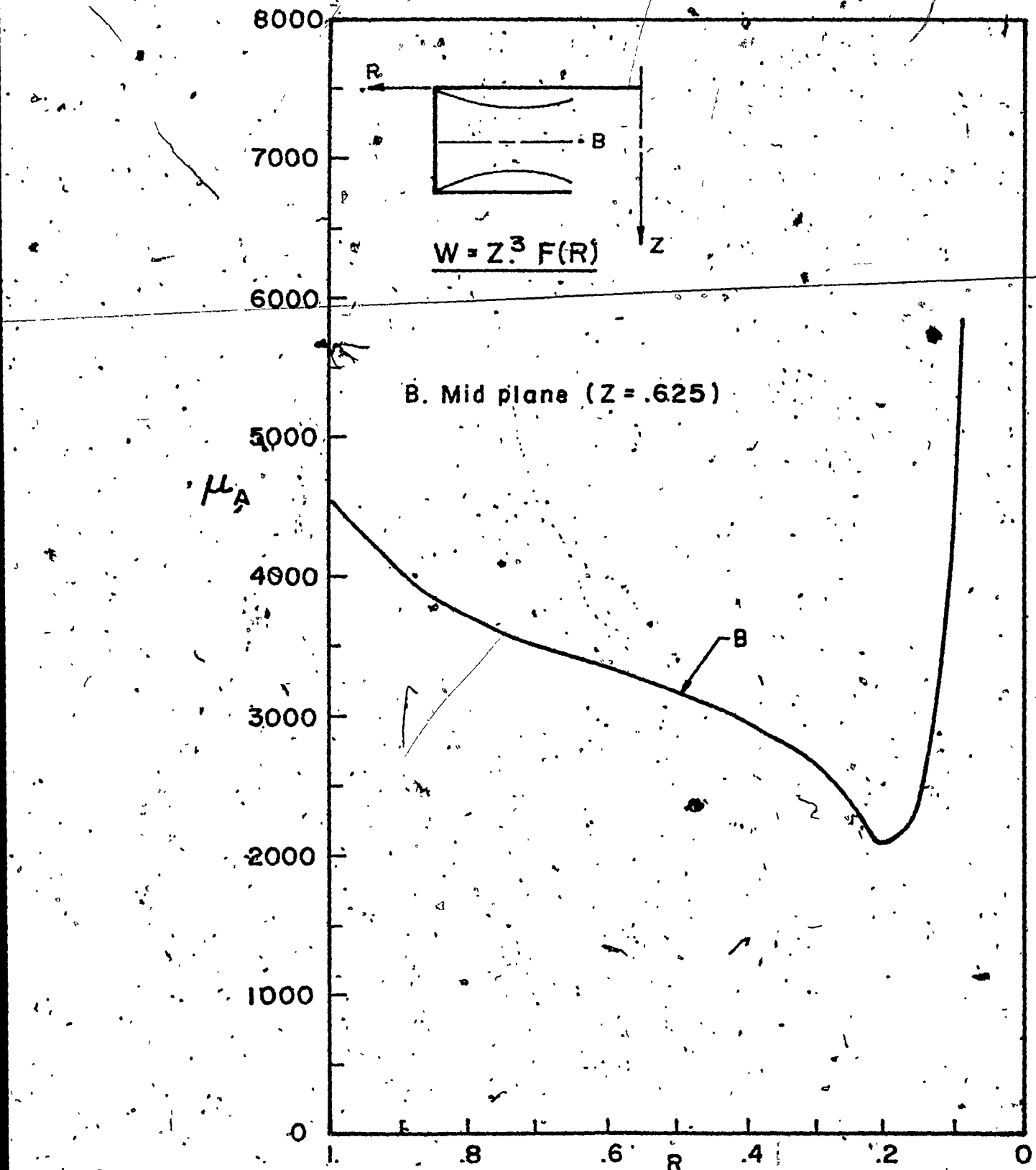

FIG. 28 THEORETICAL APPARENT VISCOSITY DISTRIBUTIONS IN THE CORE REGION — 6-CELL VORTEX

APPENDIX A

PROCEDURE FOR OBTAINING EQUATIONS (4) ON PAGE 13

Upon comparing Eqns. (3) and (1) on page 12, we can see that the components of the stress tensor due to the turbulent velocity components of the flow are:

$$\begin{bmatrix} \sigma_x & \tau_{xy} & \tau_{xz} \\ \tau_{xy} & \sigma_y & \tau_{yz} \\ \tau_{xz} & \tau_{yz} & \sigma_z \end{bmatrix} = - \begin{bmatrix} \overline{\rho u'^2} & \overline{\rho u'v'} & \overline{\rho u'w'} \\ \overline{\rho u'v'} & \overline{\rho v'^2} & \overline{\rho v'w'} \\ \overline{\rho u'w'} & \overline{\rho v'w'} & \overline{\rho w'^2} \end{bmatrix} \qquad \text{(A-1)}$$

It is noted that the components of the mean velocity of turbulent flow satisfy the same laminar flow equations, except that the laminar stresses must be increased by the addition of "apparent", or Reynolds stresses, in the turbulent flow. These stresses are due to turbulent fluctuation and are given by the time-mean values of the quadratic terms in the turbulent components. They are added to the ordinary viscous terms in laminar flow and have a similar influence on the course of the flow. These additional viscous terms are often considered to be caused by eddy viscosity.

The total stresses therefore can be expressed as the sums of the viscous stresses and the apparent stresses:

$$\sigma_x = -p + 2\mu \frac{\partial u}{\partial x} - \rho \overline{u'^2}$$

$$\sigma_y = -p + 2\mu \frac{\partial v}{\partial y} - \rho \overline{v'^2} \qquad \text{(A-2)}$$

$$\sigma_z = -p + 2\mu \frac{\partial w}{\partial z} - \rho \overline{w'^2}$$

$$\tau_{xy} = \mu\left(\frac{\partial v}{\partial x} + \frac{\partial u}{\partial y}\right) - \rho \overline{u'v'}$$

$$\tau_{yz} = \mu\left(\frac{\partial w}{\partial y} + \frac{\partial v}{\partial z}\right) - \rho \overline{v'w'} \qquad \text{(A-3)}$$

$$\tau_{zx} = \mu\left(\frac{\partial u}{\partial z} + \frac{\partial w}{\partial x}\right) - \rho \overline{u'w'}$$

In most turbulent flow, especially in vortex flow cases, the apparent stresses far outweigh the viscous components. For approximation, the latter may be omitted. Eqns. (A-2) and (A-3) become:

$$\sigma_x = -\rho \overline{u'^2}$$

$$\sigma_y = -\rho \overline{v'^2} \qquad \text{(A-4)}$$

$$\sigma_z = -\rho \overline{w'^2}$$

$$\tau_{xy} = -\rho u'v'$$

$$\tau_{yz} = -\rho \overline{v'w'} \qquad \text{(A-5)}$$

$$\tau_{zx} = -\rho \overline{u'w'}$$

Eqns. (A-4) and (A-5) represent the normal stresses and sheaning stresses respectively. Since,

$$\tau_{xy} = -\rho \overline{u'v'} = \rho\varepsilon \frac{\overline{du}}{dy} \qquad \text{(A-6)}$$

where ε is eddy viscosity as discussed by Schlichting [27]. Eqns. (A-4) and (A-5) can be changed into the form of equation (A-6) then substituted into equation (3) to obtain equation (4) on page 13.

APPENDIX B

FUNCTIONS $\phi(Z)$, $\psi(Z)$ AND THEIR DERIVATIVES

Functions $\phi(Z)$ and $\psi(Z)$ are determined by matching the boundary conditions along the Z direction at the interface between the annular and inner core flow regions.

Let δ_e be the non-dimensional boundary layer thickness at the interface where R = 1:

$$\delta_e \cong \frac{\delta(1)}{r_e}$$

Following constants are introduced:

$$C_1 = \frac{v_\delta(1) \cdot \mu_A(1)}{v_o}$$

$$C_2 = \frac{u_\delta(1)}{v_o}$$

$$C_3 = \frac{u_s(1)}{v_o}$$

a) $0 < Z \leq \delta_e$

$$\psi(Z) = C_1 \left[Z/\delta_e\right]^{\frac{1}{7}}$$

$$\frac{d\psi(Z)}{dZ} = \frac{C_1}{7\delta_e} \left[Z/\delta_e\right]^{-\frac{6}{7}}$$

$$\frac{d^2\psi(Z)}{dZ^2} = -\frac{6C_1}{49\delta_e^2} \left[Z/\delta_e\right]^{-\frac{13}{7}}$$

$$\phi(Z) = \frac{C_2}{\beta} \left[\frac{Z}{\delta_e}\right]^{\frac{1}{7}} + \frac{1.69\ C_3}{\beta} \left[\left(\frac{Z}{\delta_e}\right)^{\frac{1}{7}} + \left(\frac{Z}{\delta_e}\right)^{\frac{15}{7}} - 2\left(\frac{Z}{\delta_e}\right)^{\frac{8}{7}}\right]$$

$$\frac{d\phi(Z)}{dZ} = \frac{C_2}{7\beta\delta_e} \left[\frac{Z}{\delta_e}\right]^{-\frac{6}{7}} + \frac{1.69\ C_3}{7\beta\delta_e} \left[\left(\frac{Z}{\delta_e}\right)^{-\frac{6}{7}} + 15\left(\frac{Z}{\delta_e}\right)^{\frac{8}{7}} - 16\left(\frac{Z}{\delta_e}\right)^{\frac{1}{7}}\right]$$

$$\frac{d^2\phi(Z)}{dZ^2} = -\frac{6}{49} \frac{C_2}{\beta\delta_e^2} \left[\frac{Z}{\delta_e}\right]^{-\frac{13}{7}} + \frac{1.69}{49} \frac{C_3}{\beta\delta_e^2} \left[-6\left(\frac{Z}{\delta_e}\right)^{\frac{13}{7}}\right.$$

$$\left. + 120\left(\frac{Z}{\delta_e}\right)^{-\frac{1}{7}} - 16\left(\frac{Z}{\delta_e}\right)^{-\frac{6}{7}}\right]$$

b) $\delta_e \leq Z \leq (H - \delta_e)$

$$\psi(Z) = C_1$$

$$\frac{d\psi(Z)}{dZ} = \frac{d^2\psi(Z)}{dZ^2} = 0$$

$$\phi(Z) = C_2$$

$$\frac{d\phi(Z)}{dZ} = \frac{d^2\phi(Z)}{dZ^2} = 0$$

c) $(H - \delta_e) \leq Z \leq H$

$$\psi(Z) = C_1 \left[\frac{H - Z}{\delta_e}\right]^{\frac{1}{7}}$$

$$\frac{d\psi(Z)}{dZ} = -\frac{C_1}{7\delta_e}\left[\frac{H - Z}{\delta_e}\right]^{-\frac{6}{7}}$$

$$\frac{d^2\psi(Z)}{dZ^2} = -\frac{6C_1}{49\delta_e^2}\left[\frac{H - Z}{\delta_e}\right]^{-\frac{13}{7}}$$

$$\phi(Z) = \frac{C_2}{\beta}\left[\frac{H-Z}{\delta_e}\right]^{-\frac{1}{7}} + \frac{1.69\ C_3}{\beta}\left[\left(\frac{H-Z}{\delta_e}\right)^{\frac{1}{7}} + \left(\frac{H-Z}{\delta_e}\right)^{\frac{15}{7}} - 2\left(\frac{H-Z}{\delta_e}\right)^{\frac{8}{7}}\right]$$

$$\frac{d\phi(Z)}{dZ} = -\frac{C_2}{7\beta\delta_e}\left[\frac{H-Z}{\delta_e}\right]^{-\frac{6}{7}} - \frac{1.69}{7\beta}\frac{C_3}{\delta_e}\left[\left(\frac{H-Z}{\delta_e}\right)^{-\frac{6}{7}} + 15\left(\frac{H-Z}{\delta_e}\right)^{-\frac{8}{7}} - 16\left(\frac{H-Z}{\delta_e}\right)^{\frac{1}{7}}\right]$$

$$\frac{d^2\phi(Z)}{dZ^2} = -\frac{6}{49\beta}\frac{C_2}{\delta_e^2}\left[\frac{H-Z}{\delta_e}\right]^{-\frac{13}{7}} + \frac{1.69}{49\beta}\frac{C_3}{\delta_e^2}\left[-6\left(\frac{H-Z}{\delta_e}\right)^{-\frac{13}{7}} + 120\left(\frac{H-Z}{\delta_e}\right)^{\frac{1}{7}} - 16\left(\frac{H-Z}{\delta_e}\right)^{-\frac{6}{7}}\right]$$

APPENDIX C

COMPUTER PROGRAM

C.1 FLOW CHART

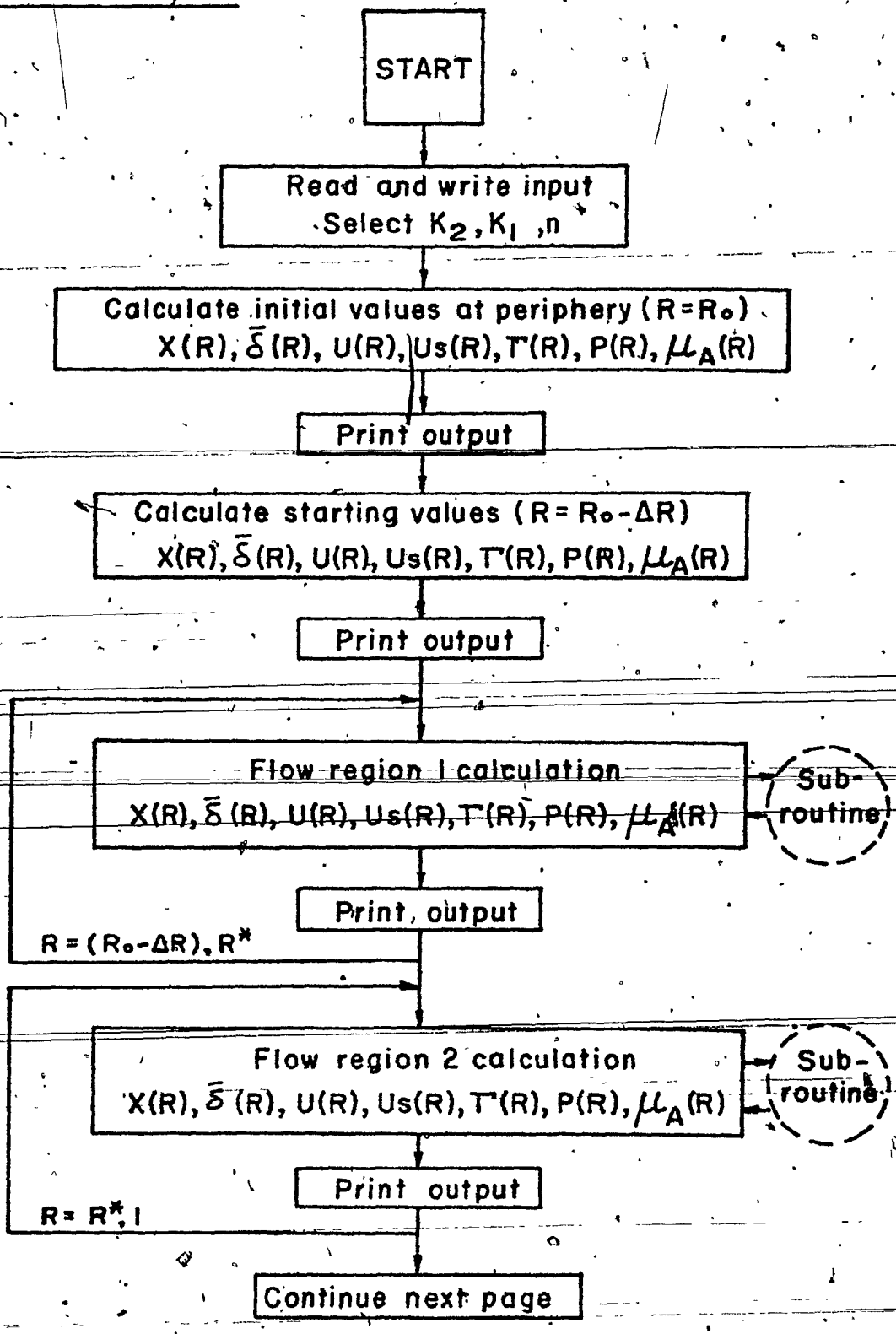

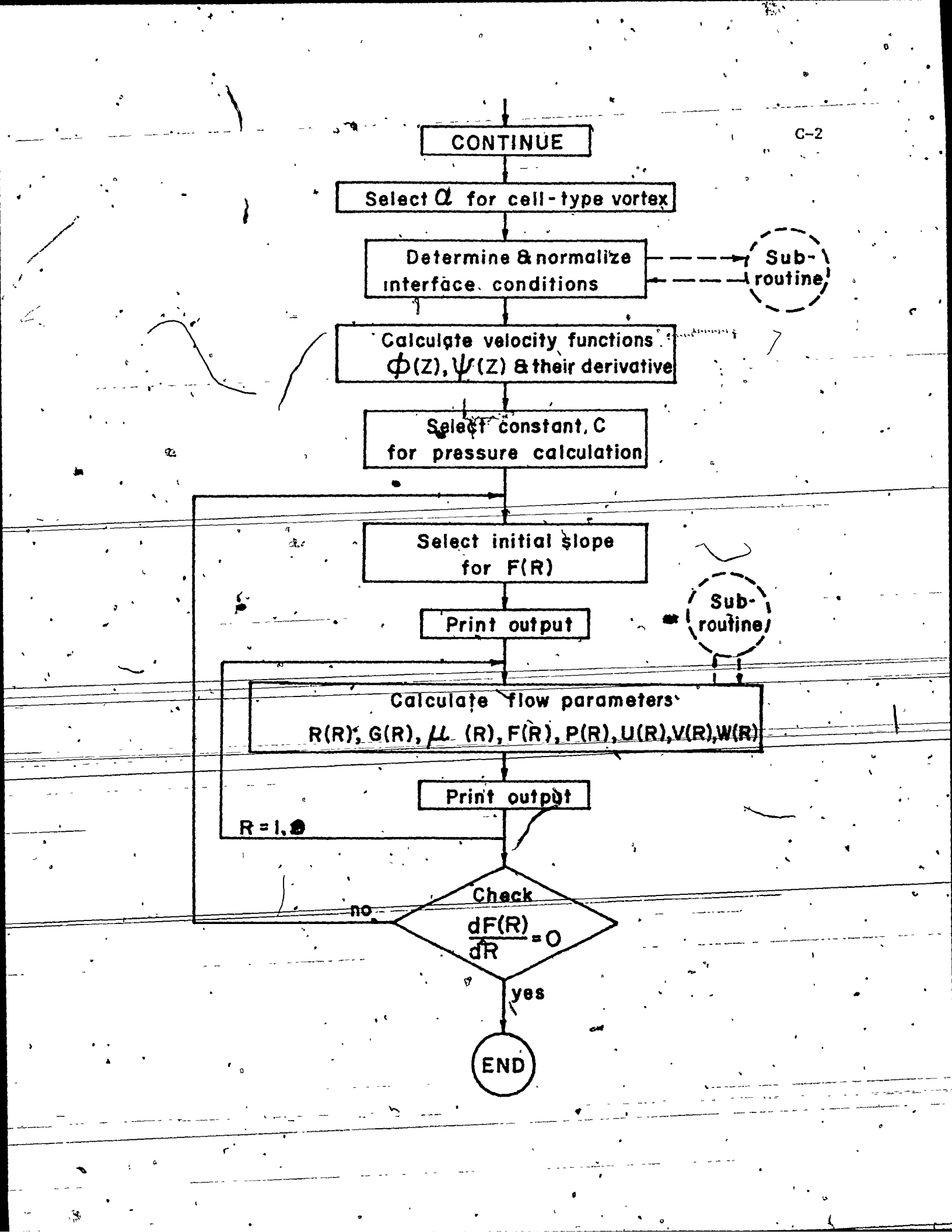
CONTINUE
Select α for cell-type vortex
Determine & normalize interface conditions
Sub-routine
Calculate velocity functions $\phi(Z)$, $\psi(Z)$ & their derivative
Select constant, C for pressure calculation
Select initial slope for F(R)
Print output
Sub-routine
Calculate flow parameters R(R), G(R), μ (R), F(R), P(R), U(R), V(R), W(R)
Print output
R = 1, 2
Check $\frac{dF(R)}{dR} = 0$
no
yes
END

C.2. LISTING

```
      PROGRAM TUSON(INPUT,OUTPUT,TAPE60=INPUT,TAPE61=OUTPUT)
C
      D I M E N S I O N
     X  YP(8,100), BY(8)   , RMUA(5),  ST(7), JA(5),
     X  Y(6,100), AY(8)   , RMU(100),  ZA(7), RS(5),
     X   CY(8),  PRES(5),  VELR(5)   , Q(8),   PZ(100)
     X   , GAMA(7),  R(100), VELT(5),CON(7)
C
      C O M M O N
     X /BLK1/ AL1,AL2,AL3,AL4,AL5,XA,XN,VO,UO,XH,XL4M,
     X          H, RHO, BN, RO
     X /BLK2/ REY,A,A1,A2,B,B1,B2,AL,Z,EN,DPZ,G2,DPRZ
     X /BLK3/  XK(4,8)
     X /BLK4/  AA(5)   , BB(5)   , CC(5)   , DD(5)
C
    1 READ(60,501) LASTRUN
      IF(LASTRUN.EQ.1RS) 2,3
    2 STOP
    3 READ(60,502)
C
C     READ AND WRITE INPUT
C
      READ(60,504) RO,RE,H,UO,VO,PO,W
      READ(60,504) RHO,XMU,XN,BN,BETA
      READ (60,504) ST
      READ(60,514) ZA
      READ(60,504) XHI,DRI,TOD,AL,DZI,DTOL,TTOD
      READ(60,504) GAMA
      READ(60,504) CON
      READ(60,504) PERC,PE4,PEA1,PEA2
      READ(60,581) PEB,PEB1,PEB2
  504 FORMAT(3F25.5)
      PRINT 503
      PRINT 501
      PRINT 502
      WRITE(61,505) RO,RE,H,UO,VO,PO,W
      WRITE(61,512) RHO,XMU,XN,BN,BETA
      WRITE(61,505) ST
      WRITE(61,514) ZA
      WRITE(61,505) XHI,DRI,TOD,AL,DZI,DTOL,TTOD
      WRITE(61,505) GAMA
      WRITE(61,505) CON
      WRITE(61,505) PERC,PE4,PEA1,PEA2
      WRITE(61,581) PEB,PEB1,PEB2
      DR = DRI
```

```
C
C     CONSTANTS AND CONVERSIONS
C
      PI=3.14159
      AL1= .77773
      AL2= .35004
      AL3= .31337
      AL4= .43914
      AL5= .87500
      XH = XH1
      XLAM= V0/U0
      TOL= 1.-RE/R0
      FLO = W*S0./RH0
C
C     INITIAL CONDITIONS
C
      HE = H/RE
      DZ = -DZ1
C
      KK=1
   13 XA=ZA(KK)
      PRINT 509, XA,BN
      PRINT 510
      Y(1,1)= 0.
      Y(2,1)= 0.
      Y(3,1)= 1.0
      Y(4,1)= 0.
      Y(5,1)= 1.0
      Y(6,1)= P0*32.196*144./(RH0*U0**2)
      DELP= 1.
      UPN= 1.0
      USN= 0.
      XMUA= XA*(Y(5,1)*V0/(1.-Y(1,1)))**XN +BN
      RMU(1) = XMUA/XMU
      R(1) = R0
      PRINT 506,R(1), (Y(M,1),M=1,6),UPN,USN,DELP,RMU(1)
C
      F=.0225
      Y(1,2)= XH
      CF= F/ (RH0*H/12.*U0/(2.*XMU))**.25
      Y(2,2)=( 13.1*2.*R0/H*CF*SQRT(XH)/XLAM**.25)**.8
      Y(4,2)= .686*XLAM*SQRT(XH)
      Y(3,2) = (1.-.125*Y(2,2) - .378*Y(2,2)*Y(4,2))/
     1  (1.+.25*Y(2,2))
      Y(5,2)= 1.0
      SIM = -Y(3,2)/XH*(Y(3,2)-Y(3,1))-XLAM**2/(1.-XH)**3
     1  *Y(5,1)**2
      Y(6,2)= XH*SIM +Y(6,1)
      DELP= Y(6,2)/Y(6,1)
      UPN= Y(3,2)*(1.-Y(1,2))
      USN= Y(4,2)*(1.-Y(1,2))
      XMUA= XA*(Y(5,2)*V0/(1.-Y(1,2)))**XN +BN
      RMU(2) = XMUA/XMU
      R(2) = R0 * (1. -XH)
      PRINT 506,R(2),(Y(M,2),M=1,6),UPN,USN,DELP,RMU(2)
```

```
C
C     REGION OF 2 VEL. COMPONENTS FLOW.
C
      J=2
      II = 1
    4 CALL SOL (Y(1,J),Y(2,J),Y(3,J),Y(4,J),Y(5,J),Y(6,J),II)
      DO 5 M=1,6
    5 AY(M) = Y(M,J)+0.5*XH*XK(1,M)
      II = 2
      CALL SOL (AY(1), AY(2), AY(3), AY(4), AY(5), AY(6), II)
      DO 10 M=1,5
   10 BY(M) = Y(M,J) +0.5*XH * XK(2,M)
      II = 3
      CALL SOL (BY(1), BY(2), BY(3), BY(4), BY(5), BY(6), II)
      DO 15 M=1,6
   15 CY(M) = Y(M,J) + XH * XK(3,M)
      II = 4
      CALL SOL (CY(1), CY(2), CY(3), CY(4), CY(5), CY(6), II)
C
      JJ=J+1
      DO 20 M=1,6
   20 Y(M,JJ) = Y(M,J)+XH/6.*(XK(1,M)+ 2.*XK(2,M)
     1  +2.*XK(3,M) +XK(4,M))
      R(JJ) = RO*(1.-Y(1,JJ))
      DELP= Y(6,JJ)/Y(6,1)
      UPN= Y(3,JJ)*(1.-Y(1,JJ))
      USN= Y(4,JJ)*(1.-Y(1,JJ))
      XMUA= XA*(Y(5,JJ)*VO/(1.-Y(1,JJ)))**XN+BN
      RMU(JJ) = XMUA/XMU
      IF(Y(3,JJ)) 52,52,50
   50 IF(Y(1,JJ).EQ.TOL) GO TO 24
      IF(Y(1,JJ).GT.TOL) 22, 24
   22 XH = TOL - Y(1,J)
      II = 1
      GO TO 4
   24 PRINT 506,R(JJ),(Y(M,JJ),M=1,6),UPN,USN,DELP,RMU(JJ)
      IF(Y(1,JJ).EQ.TOL) GO TO 47
      J= JJ
      II= 1
      GO TO 4
   52 CONTINUE
      Y(3,J) = 0.
      II= 1
   34 CALL SOK(Y(1,J),Y(2,J),Y(3,J),Y(4,J),Y(5,J),Y(6,J),II)
      DO 35 M=1,6
   35 AY(M) = Y(M,J)+0.5* XH * XK(1,M)
      II = 2
      CALL SOK(AY(1),AY(2),AY(3),AY(4),AY(5),AY(6),II)
      DO 40 M=1,6
   40 BY(M) = Y(M,J)+0.5* XH * XK(2,M)
      II = 3
      CALL SOK(BY(1),BY(2),BY(3),BY(4),BY(5),BY(6),II)
      DO 42 M=1,6
   42 CY(M) = Y(M,J)+ XH* XK(3,M)
      II = 4
```

```
      CALL SOK(CY(1),CY(2),CY(3),CY(4),CY(5),CY(6),II)
C
      JJ= J+1
      DO 45 M=1,6
   45 Y(M,JJ) = Y(M,J)+ XH/6.*(XK(1,M)+ 2.*XK(2,M)+2.*
     1    XK(3,M) + XK(4,M))
      R(JJ) = RO*(1.-Y(1,JJ))
      DELP= Y(6,JJ)/Y(6,1)
      UPN= Y(3,JJ)*(1.-Y(1,JJ))
      USN= Y(4,JJ)*(1.-Y(1,JJ))
      XMUA= XA*(Y(5,JJ)*VO/(1.-Y(1,JJ)))**XN+BN
      RMU(JJ) = XMUA/XMU
      IF(Y(1,JJ).EQ.TOL) GO TO 46
      IF(Y(1,JJ).GT.TOL) 44, 46
   44 XH = TOL - Y(1,J)
      II = 1
      GO TO 34
   46 PRINT 506,R(JJ),(Y(M,JJ),M=1,6),UPN,USN,DELP,RMU(JJ)
      IF(Y(1,JJ).EQ.TOL) GO TO 47
      J= JJ
      II= 1
      GO TO 34
   47 CONTINUE
C
C     DETERMINING AND NORMALIZING INTERFACE CONDITIONS
C
      PAMB = 14.7 * 32.196 *.144./(RHO*VO**2)
      POI = PO *32.196 *144./(RHO * VO **2)- PAMB
      REY = RHO/32.196 * VO * RE/(12.*XMU)
      JA(5) = JJ
      JA(4) = JJ-1
      JA(3) = JJ-2
      JA(2) = JJ-3
      JA(1) = JJ-4
      RS(5) = 1.
      RS(4) = RS(5) + XH/RE
      RS(3) = RS(4) + XH1/RE
      RS(2) = RS(3) + XH1/RE
      RS(1) = RS(2) + XH1/RE
C
      DO 75 I= 1,5
      K = JA(I)
      PRES(I) = Y(6,K) * UO**2/VO**2 - PAMB
   75 RMUA(I) = RMU(K)
      CALL VAN (5,RS,RMUA)
      DMU = 3.*AA(4)*RS(5)**2 +2.*BB(4)*RS(5)+CC(4)
      CALL VAN (5,RS,PRES)
      DPR = 3.*AA(4)*RS(5)**2 +2.*BB(4)*RS(5)+CC(4)
C
      E1 = 1./7.
      E2 = 8./7.
      E3 = 15./7.
      E4 = -6./7.
      E5 = -13./7.
      E6 = -20./7.
```

```
      NJ = JJ
C
C     DEFINING VELOCITY FUNCTIONS AND DERIVATIVES
C
      XZ = HE
      XZ = XZ+DZ
   80 RI = RS(5)
      THEZ = Y(2,NJ)*H/2./RE
      HTEZ = HE-THEZ
      IF(XZ.GT.HTEZ) 62,64
   62 XZ = HE-XZ
      GO TO 70
   64 IF(XZ.GT.THEZ) 66,70
   66 XZ = HE-XZ
      GO TO 70
   70 DO 82 I = 1,5
      K = JA(I)
      VDEL = VO*RO*Y(5,K)/R(K)
      UDEL = -UO*Y(3,K)
      USE = -UO*Y(4,K)
      THETA = Y(2,K)*H/2./RE
      ETA = XZ/THETA
      IF(ETA.GT.1.) GO TO 81
      FETA = ETA**E1
      GO TO 83
   81 ETA = 1.
      FETA = 1.
   83 GETA = 1.69*FETA*(1.-ETA)**2
      U = UDEL*FETA+USE*GETA
      V = VDEL*FETA
      VELT(I) = V/VO
   82 VELR(I) = U/VO
      CALL VAN(5,RS,VELR)
      DVELR = 3.*AA(4)*RS(5)**2+2.*BB(4)*RS(5)+CC(4)
      CALL VAN(5,RS,VELT)
      DVELT = 3.*AA(4)*RS(5)**2+2.*BB(4)*RS(5)+CC(4)
      EN = -RMUA(5)*DVELT/(DMU*VELT(5))
      THE = Y(2,NJ) * H/2./RE
      HTE = H/RE - THE
      THE2 = THE **2
      THE3 = THE **3
      UDEL = -UO * Y(3,NJ)
      USE = -UO * Y(4,NJ)
      VDEL = VO * RO * Y(5,NJ)/RE
      C1 = VDEL * RMU(NJ)**EN/VO
      C2 = -UDEL/VO
      C3 = -USE/VO
   60 Z = HE
      Z = Z + DZ
      ZE = Z/THE
      IF ( Z.LT.THE) 85,90
   85 AAQ = C2 *ZE**E1 + 1.69*C3*(ZE**E1+ZE**E3 - 2.*ZE**E2)

      AA1 = .14286* C2/THE* ZE**E4 + C3/THE*(.24143*ZE**E4
     1      + 3.62143 *ZE**E2-3.86286*ZE**E1)
```

```
      AA2 =-.12245 *C2/THE2*ZE**E5+C3/THE2*(-.20694*ZE**E5
     1       + 4.13878*ZE**E1-.55184* ZE**E4)
      B   = C1*ZE**E1
      B1  = .14286 *C1/THE*ZE**E4
      B2  = -.12245*C1/THE2*ZE**E5
      GO TO 105
   90 IF(Z.LE.HTE) 95,100
   95 AA0= C2
      AA1 = 0.
      AA2= 0.
      B   = C1
      B1  =0.
      B2 = 0.
      GO TO 105
  100 ZE  = (HE - Z)/THE
      AA0 = C2* ZE**E1+1.69*C3*(ZE**E1+ZE**E3-2.*ZE**E2)
      AA1 = -.14286 * C2/THE * ZE **E4-C3/THE*(.24143*ZE**E4
     1       + 3.62143 *ZE**E2 - 3.86286 * ZE**E1)
      AA2 =-.12245* C2/THE2*ZE**E5+C3/THE2*(-.20694*ZE**E5
     1       + 4.13878 *ZE**E1- .55184*ZE**E4)
      B   = C1 *ZE **E1
      B1  = -.14286 *C1/THE*ZE**E4
      B2  = -.12245*C1/THE2 *ZE **E5
  105 A   = AA0/BETA
      A1  = AA1/BETA
      A2  = AA2/BETA
C
C
      PRINT 525
      PRINT 560, Z,A,A1,A2,B,B1,B2,C1,AA0, AA1,AA2,DVELR
      L = 1
      PPZ = CON(L)*(Z**2-HE**2)
  110 YP(1,1) = 1.
      YP(2,1) = BETA
      YP(3,1) = DVELR
      YP(4,1) = RMUA(5)
      YP(5,1) = DMU
      IF(PERC.GT.0.) GO TO 107
      YP(6,1) = (DVELR+A*BETA)/(AL*Z**(AL-1.))
      GO TO 108
  107 YP(6,1) = PERC
      A = PEA
      A1 = PEA1
      A2 = PEA2
      B = PEB
      B1 = PEB1
      B2 = PEB2
  108 DPRZ = 0.
      PZ(1) = PRES(5)
      YP(8,1) = PRES(5)-PPZ
      KKK= 1
  115 GA = GAMA(KKK)
      YP(7,1) = GA
      DR=DR1
      TOD1 = TOD
```

```
      G2 = 2.*BETA +AL*GA*Z**(AL-1.)/A
      DPZ = 2.*CON(L)*Z
      PRINT 520, AL,BETA,EN,GA,CON(L)
      PRINT 560, THE,UDEL,USE,VDEL,DPZ,REY,DPR,G2,PAMB
C
      J = 1
      PRINT 535
C
      VR = A*YP(2,1)
      VT = B/YP(4,1)**EN
      VZ = Z**AL*YP(6,1)
C
      PRINT 560,(YP(M,JJ), M= 1,8), VR,VT,VZ,PZ(1)
C
C
      DPRZ = 0.
  120 CONTINUE
      DO 122 M= 1,8
  122 Q(M) = YP(M,J)
      II = 1
      CALL TAN (QN1,Q(2),Q(3),Q(4),Q(5),Q(6),Q(7),II)
      DO 200 M= 1,8
  200 AY(M) = YP(M,J)+0.5*DR*XK(1,M)
      II=2
      CALL TAN (AY(1),AY(2),AY(3),AY(4),AY(5),AY(6),AY(7),II)
      DO 220 M= 1,8
  220 BY(M) = YP(M,J) + 0.5*DR*XK(2,M)
      II = 3
      CALL TAN (BY(1),BY(2),BY(3),BY(4),BY(5),BY(6),BY(7),II)
      DO 240 M= 1,8
  240 CY(M) = YP(M,J) + DR*XK (3,M)
      II = 4
      CALL TAN (CY(1),CY(2),CY(3),CY(4),CY(5),CY(6),CY(7),II)
      JJ=J+1
      DO 260 M= 1,8
  260 YP(M,JJ) = YP(M,J) +DR/6.*(XK(1,M)+2.*XK(2,M)
     1   +2.*XK(3,M)+XK(4,M))
C
C     CALCULATION OF AXIAL VELOCITY
C
      YP(3,JJ) = AL*Z**(AL-1.)*YP(6,JJ)/A - YP(2,JJ)/YP(1,JJ)
      G2 = YP(2,JJ)/YP(1,JJ)**2 -YP(3,JJ)/YP(1,JJ)
     1   +AL*Z**(AL-1.)*YP(7,JJ)/A
      PZ(JJ) = YP(8,JJ)+PPZ
C
      VR = A*YP(2,JJ)
      VT = B/YP(4,JJ)**EN
      VZ = Z**AL*YP(6,JJ)
      PRINT 560,(YP(M,JJ), M=1,8), VR,VT,VZ,PZ(JJ)
      J = JJ
      IF(YP(1,JJ).GT.TOD1) GO TO 120
      DR = DTOL
      TOD1 = TTOD
      IF(YP(1,JJ).GT.TOD1) GO TO 120
C
```

```
C     CALCULATION OF MASS FLOW
C
      GPM = 0.
      DO 270 JX = 1,J
      VZT = HE**AL*YP(6,JX)*V0*60.
      DAT = 2.*PI*RE*YP(1,JX)*RE*(-DR)/144.
  270 GPM= GPM+VZT*DAT
      YP(1,J) = 0.
      YP(2,J) = 0.
      YP(3,J) = .11111
      YP(4,J) = .11111
      YP(5,J) = .11111
      YP(6,J) = .11111
      YP(7,J) = 0.
      YP(8,J) = 0.
      PZ(J) = .11111
      VR = 0.
      VT = 0.
      VZ = .11111
      PRINT 560,(YP(M,JJ), M=1,8), VR,VT,VZ,PZ(JJ)
      PRINT 580, GPM,FLO
C
  300 CONTINUE
      KKK = KKK+1
      IF(GAMA(KKK).EQ.0.) GO TO 280
      GO TO 115
  280 L = L+1
      IF(CON(L).EQ.0.) GO TO 1
      GO TO 110
  501 FORMAT(79H
     1                              ,R1)
  502 FORMAT(79H
     1                              )
  503 FORMAT(1H1)
  504 FORMAT(7F10.4)
  505 FORMAT(/7F10.4)
  506 FORMAT(2F6.3,4F10.4,F15.5,3F10.4,F15.5)
  508 FORMAT(//5X17H STATION (IN.) = F5.2,5X5H X = F5.2/)
  509 FORMAT(//5X5H AN= F10.7,5X6H BN = F10.7/)
  510 FORMAT(/*    R      X        DEL        U          US         GAM
     X  P          UPH        USN          P/PO       MUA/MU */)
  512 FORMAT(/2F10.7,5F10.4)
  514 FORMAT(7F10.7)
  516 FORMAT(/* Z        U          V          VEL          Z/H        U/U
     XO         V/VO  */)
  520 FORMAT(//5X26H,VORTEX FLOW WITH ALPHA = ,F5.2,
     15X8H BETA = ,F8.4,5X5HEN = ,F5.2,5X8H GAMA = ,F10.4,
     15X7H CON = ,F10.4/)
  525 FORMAT(//* Z       PHI          PHI1         PHI2         PSI
     1PSI1        PSI2                    */)
  535 FORMAT(//* R        G          DG         MUA         DMUA
     X F          DF          PR          VR          VT          V
     XZ          P *)
  550 FORMAT(I4,6F15.4)
  560 FORMAT(F6.3,7E12.5,4E11.4)
```

```
 580 FORMAT(//5X11HFLOW OUT = ,E12.5,5X11H FLOW IN = ,E12.5//)
     END
     SUBROUTINE SOL(X1, X2, X3, X4, X5, X6, I)
C
     C O M M O N
    X /BLK1/  A1 ,A2 ,A3 ,A4 ,A5 ,XA ,XN ,VO ,UO ,XH ,XLA ,
    X         H ,RHO ,BN ,RO
    X /BLK3/  XK(4,4)
C
C    DETERMINATION OF DIFFERENTIAL EQN COEFF.
C
     XNN=XN+1.
     A11= A5*X3+A4*X4-X3
     A21= A1*X3**2+2.*A2*X3*X4-A5*X3**2-A4*X3*X4+A3*X4**2
     A31= A1*X3+A2*X4-A5*X3-A4*X4
     A12= A5*X2+1.-X2
     A22 = 2.*A1*X2*X3+2.*A2*X2*X4-A5*X2*X3
     A32= (A1-A5)*X2
     A42= X3
     A13= A4*X2
     A23= 2.*A2*X2*X3-A4*X2*X3+2.*A5*X2*X4
     A33= (A2-A4)*X2
     A34= (A1*X2*X3+A2*X2*X4)/X5
     A54= X3
     A25= X2
     A45= 1.
     B1= (A5*X2*X3+A4*X2*X4+(1.-X2)*X3)/(1.-X1)
     TAR1=4.*XA*RO*X3/(7.*RHO*H**2*UO*X2)*(X5*VO/(1.-X1))**XN
     TAR2= 4.*BN*X3*RO/(7.*RHO*UO*H**2*X2)
     TAR= TAR1+TAR2
     SIM = A1*X2*XLA**2*X5**2/(1.-X1)**2
     B2 = 1./(1.-X1)*(SIM-A1*X2*X3**2-2.*A2*X2*X3*X4-
    1 A3*X2*X4**2+A5*X2*X3**2+A4*X2*X3*X4)+TAR
     TAT1= 4.*RO*XA*(1.-X1)/(7.*X5*XLA*H**2*RHO*X2*UO**2)
    1  *(X5*VO/(1.-X1))**XNN
     TAT2= 4.*RO*BN*VO/(7.*RHO*H**2*UO**2*X2*XLA)
     TAT= -TAT1-TAT2
     B3=-(A1*X2*X3-X2*A2*X4+A5*X2*X3+A4*X2*X4)/(1.-X1)+TAT
     B4= X5**2*XLA**2/(1.-X1)**3
     B5=0.
C
C    DIFFERENTIAL EQUATION SYSTEM
C
     C11=A11
     C12=A12
     C13=A13
     C21=-A21
     C22=-A22+A25*A42
     C23=-A23
     C31=A31
     C32=A32
     C33=A33
     D1=B1
     D2=B2-B4*A25
     D3=+B3-B5/A54*A34
```

```
      DET=C11*(C22*C33-C23*C32)+C12*(C31*C23-C21*C33)
     1   +C13*(C21*C32-C31*C22)
      DET2=D1*(C22*C33-C23*C32)+D2*(C32*C13-C12*C33)
     1 +D3*(C12*C23-C22*C13)
      DET3= D1*(C23*C31-C21*C33) +D2*(C11*C33-C13*C31)
     1   +D3*(C21*C13-C23*C11)
      DET4= D1*(C21*C32-C22*C31)+D2*(C12*C31-C32*C11)
     1   +D3*(C11*C22-C21*C12)
      XK(I,1) = 1.0
      XK(I,2) = DET2/DET
      XK(I,3) = DET3/DET
      XK(I,4) = DET4/DET
      XK(I,5) = B5/A54
      XK(I,6) = -B4-A42*XK(I,3)
      RETURN
      END
      SUBROUTINE SOK(X1, X2, X3, X4, X5, X6, I)
C
      C O M M O N
     X /BLK1/  A1 ,A2 ,A3 ,A4 ,A5 ,X4 ,XN ,VO ,UO ,XH ,XLA ,
     X         H ,RHO ,BN ,RO
     X /BLK3/  XK(4,8)
C
C
C     DETERMINATION OF DIFFERENTIAL EQN. COEFF.
C
      XNN=XN+1.
      A11= A4*X4
      A12= A4*X2
      A21=-A3*X4**2
      A22= -2.*A3*X2*X4
      A31= X4*(A2-A4)
      A32= X2*(A2-A4)
      A33= A2*X2*X4/X5
      B1= A4*X2*X4/(1.-X1)
      TAR= 0.
      SIM = (A1*X2*XLA**2*X5**2/(1.-X1)**2-A3*X2*X4**2)
     1    /(1.-X1)-TAR
      B2= SIM-X2*X5**2*XLA**2/(1.-X1)**3
      TAT1= 4.*RO*X4*(1.-X1)/(7.*X5*XLA*H**2*RHO*X2*UO**2)
     1  *(X5*VO/(1.-X1))**XNN
      TAT2= 4.*RO*BN*VO/(7.*RHO*H**2*UO**2*X2*XLA)
      TAT= -TAT1-TAT2
      B3=+(    A2*X2*X4-A4*X2*X4)/(1.-X1)+TAT
C
C     DIFFERENTIAL EQUATION SYSTEM
C
      DET= A33*(A11*A22-A12*A21)
      DET2=A33*(B1*A22-B2*A12)
      DET4=A33*(B2*A11-B1*A21)
      DET5= A11*(A22*B3-A32*B2)-A12*(A21*B3-A31*B2)
     1  +B1*(A21*A32-A22*A31)
      XK(I,1) = 1.0
      XK(I,2) = DET2/DET
      XK(I,3) = 0.0
      XK(I,4) = DET4/DET
```

```
      XK(I,5) = DET5/DET
      XK(I,6) = -XLA**2 *X5**2/(1.0-X1)**3
      RETURN
      END
      SUBROUTINE VAN (N,X,Y)
C
C     BEAM FIT LAST POINTS TO OBTAIN INITIAL CONDITIONS
C
      DIMENSION  X(5) ,Y(5)
      COMMON
     X /BLK4/  AA(5)  , BB(5)  , CC(5)  , DD(5)
C
      SL1= (Y(2)-Y(1))/(X(2)-X(1))
      SL2= (Y(3)-Y(2))/(X(3)-X(2))
      PS1= .5*(X(2)+X(1))
      PS2= .5*(X(3)+X(2))
      DSL= (SL2-SL1)/(PS2-PS1)
      SL0 = SL1+DSL*(X(1)-PS1)
      SL1= (Y(N-1)-Y(N))/(X(N-1)-X(N))
      SL2= (Y(N-2)-Y(N-1))/(X(N-2)-X(N-1))
      PS1= .5*(X(N-1)+X(N))
      PS2= .5*(X(N-2)+X(N-1))
      DSL = (SL2-SL1)/(PS2-PS1)
      SLN= SL1+DSL*(X(N)-PS1)
C
      DO 1 J= 2,N
      AA(J) = X(J)-X(J-1)
    1 DD(J) = (Y(J)-Y(J-1))/AA(J)
      K2= N-2
      CC(N) = 3.0*(SLN-DD(N))/AA(N)
      BB(N) = 0.5
      DO 9 J=1,K2
      K= N-J
      T= 2.0*(AA(K)+AA(K+1))-AA(K+1)*BB(K+1)
      BB(K) = AA(K)/T
    9 CC(K) = (6.0*(DD(K+1)-DD(K))-AA(K+1)*CC(K+1))/T
      BB(1)=(6.*(DD(2)-SL0)-CC(2)*AA(2))/(AA(2)*(2.-BB(2)))
      DO 16  J=2,N
   16 BB(J) = CC(J)-BB(J)*BB(J-1)
      DO 19 J=2,N
      TA = 6.0*AA(J)
      TM = BB(J-1)*X(J)
      TN = X(J-1)*BB(J)
      TX=X(J)*(X(J)-X(J-1)-X(J-1))
      TY= X(J-1)*(X(J)+X(J)-X(J-1))
C
      AA(J-1) = (BB(J)-BB(J-1))/TA
      CC(J-1) = DD(J)+(BB(J)*(-TX)+2.*X(J-1)*TN-BB(J-1)
     1   *TY-2.*X(J)*TM)/TA
      BB(J-1) = (TM-TN)*3.0/TA
   19 DD(J-1) = (TX*TN+TY*TM)/TA+Y(J-1)-X(J-1)*DD(J)
      RETURN
      END
      SUBROUTINE  TAN ( X1, X2, X3, X4, X5, X6, X7, I)
C
```

```
      C O M M O N
     X /BLK2/ REY,A,A1,A2,B,B1,B2,AL,Z,EN,DPZ,G2,DPRZ
     X /BLK3/  XK(4,3)
      XI = I
      XK(I,1) = 1.
      XK(I,2) = -X2/X1+AL*Z**(AL-1.)*X6/1
      XK(I,3) = 0.
      XK(I,4) = X5
      Q11 = +1*REY*(1./X1-EN*X5/X4)*X2/EN
      Q22 = (32/B-1./X1**2)*X4/EN
      Q33 = EN*X5/X4-2./(EN*X1)+ (1.-EN)/(EN*X1)
      Q44 =  -Z**AL *B1*REY*X6/B/EN
      XK(I,5) = Q11+Q22+Q33*X5+Q44.
      XK(I,6) = X7
      Q1 = -X7/X1-X7*X5/X4-REY*1*X2*X7/X4
      Q2 = AL*REY*Z**(AL-1.)*X6**2/X4+REY*DPZ/X4/Z**AL
      Q3 =-2.*AL*(AL-1.)*X6/Z**2+A1/Z**AL*(X2*X5/X4+X3+X2/X1)
      XK(I,7) = Q1+Q2+Q3
      Q1 = -4*X4*G2/REY
      Q2 = -A*X3/REY*(2.*X5+X4/X1+X2*REY*A)
      Q3 = -X4*X2/REY*(A2-Z**AL*REY*X6*A1/X4-A/X1**2)
      Q4 = B**2/X1/X4**(2.*EN)
      XK(I,8) = Q1+Q2+Q3+Q4-DPRZ
C
      RETURN
      END
* EOF *
```